

**EVAPOTRANSPIRATION, SURFACE CONDUCTANCE AND WATER-USE  
EFFICIENCY OF TWO YOUNG HYBRID-POPLAR PLANTATIONS IN CANADA'S  
ASPEN PARKLAND**

by

Hughie Jones

B.Sc., The University of Alberta, 2012

A THESIS SUBMITTED IN PARTIAL FULLFILLMENT  
OF THE REQUIREMENTS FOR THE DEGREE OF

MASTERS OF SCIENCE

in

THE FACULTY OF GRADUATE AND POSTDOCTORAL STUDIES  
(Soil Science)

THE UNIVERSITY OF BRITISH COLUMBIA  
(Vancouver)

August 2014

© Hughie Jones, 2014

## Abstract

Hybrid poplar (HP) plantations established on former agricultural land in the aspen parkland of Canada have the potential to provide fibre, bio-energy and ecosystem services. The low precipitation and large summertime vapor pressure deficits in the aspen parkland raise questions about HP plantation water use and its effects on regional water supplies. In 2010 and 2011, I began using the eddy-covariance (EC) technique to measure CO<sub>2</sub>, water vapor and sensible heat fluxes above two young HP plantations planted in 2009 (HP09) and 2011 (HP11) on clay loam Chernozemic soil located near Edmonton, AB and Winnipeg, MB, respectively. Measurements showed that both HP09 and HP11 shifted from carbon (C) sources to C sinks in the 3<sup>rd</sup> year of growth. EC measured evapotranspiration ( $E$ ) and climate data were used to calculate bulk surface conductance ( $G_s$ ) using the inverted Penman-Monteith (PM) equation and were compared to  $G_s$  estimates derived from a biophysical model that permits the partitioning of  $E$  into canopy transpiration ( $E_c$ ) and evaporation from the soil ( $E_s$ ).  $E_s$  was estimated using the equilibrium evaporation rate modified to account for soil moisture effects on  $E_s$  using a soil water content based multiplier ( $f$ ), and  $E_c$  was estimated using a canopy conductance ( $G_c$ ) sub-model and the PM equation. Modelled half-hourly values of  $G_s$  showed excellent diurnal and seasonal agreement with EC-calculated  $G_s$ . Measured and modelled  $E$  also had excellent agreement, and using the  $G_s$  model, I was able to show the relative contribution of  $E_c$  and  $E_s$  to  $E$  as the plantation grew. For example, in the 5<sup>th</sup> year of growth at HP09, measured and modelled  $E$  was 400 and 428 mm, respectively, of which 138 and 290 mm occurred as  $E_s$  and  $E_c$ , respectively. Values of water use efficiency calculated as gross primary productivity divided by  $E$ , increased every year of growth and were similar at both sites. Results show  $E_s$  dominates  $E$  during the first 2 years of HP growth and as  $E_c$  becomes increasingly dominant in the following

years,  $E$  can exceed  $P$ , suggesting HP planted on highly productive agricultural soils in Canada's aspen parkland can become water limited.

## **Preface**

The HP09 data (2010 and 2011) used in this thesis were used in a previous publication, for which I am a co-author. During 2010 and 2011, I was a field technician with the Climate Change Group at the Northern Forestry Centre (Natural Resources Canada) in Edmonton, AB. During this time I was responsible for collecting field data and maintaining all field instrumentation used in the publication below.

Jassal, R. S., Black, T. A., Arevalo, C., Jones, H., Bhatti, J. S., and Sidders, D. (2013). Carbon sequestration and water use of a young hybrid poplar plantation in north-central Alberta. *Biomass and Bioenergy*, 56: 323–333.

# Table of Contents

Abstract .....	ii
Preface .....	iv
Table of Contents .....	v
List of Tables .....	vii
List of Figures .....	viii
Acknowledgements .....	xiv
Dedication .....	xv
1 Introduction .....	1
1.1 Afforestation, biomass and bioenergy .....	1
1.2 Carbon sequestration and greenhouse gas fluxes .....	2
1.3 Water balance issues and evapotranspiration modelling .....	3
1.4 Objectives .....	5
2 Theory .....	7
2.1 Canopy conductance model .....	7
2.2 Soil evaporation model .....	9
2.3 Surface conductance model .....	9
3 Methods .....	12
3.1 Site descriptions .....	12
3.2 Climate measurements .....	13
3.3 Energy balance measurements and closure .....	14
3.4 EC instrumentation and flux calculations .....	15
3.5 Water balance .....	18
3.6 Canopy and boundary layer characteristics .....	18
4 Results .....	20
4.1 Weather .....	20
4.2 Surface properties and energy balance .....	22
4.2.1 Seasonal and diurnal energy balance components .....	22
4.2.2 Energy balance closure .....	27
4.3 Surface conductance .....	30
4.3.1 Seasonal and annual surface conductance .....	30
4.3.2 Controls on surface conductance .....	31

4.4	Canopy and surface conductance model .....	33
4.4.1	Canopy conductance model .....	33
4.4.2	Diurnal and seasonal performance of the surface conductance model .....	35
4.4.3	Diurnal and annual evapotranspiration partitioning.....	40
4.5	Annual water balance and water use efficiency .....	46
4.5.1	Water balance.....	46
4.5.2	Carbon balance.....	49
4.5.3	Water use efficiency.....	51
5	Discussion .....	53
5.1	Surface and canopy conductance model .....	53
5.2	Energy balance.....	55
5.3	Water balance.....	58
5.4	Carbon balance.....	60
5.5	Water use efficiency.....	61
6	Conclusions.....	63
	References.....	65
	Appendices.....	73

## List of Tables

Table 1. $G_c$ and $G_s$ model input parameters with their respective equations, values and sources. ....	11
Table 2: Annual NEP, GPP, $R_e$ , $E$ and WUE at both sites for each year of the study period. ....	51
Table 3: EC instrumentation ( $z$ ), canopy ( $h$ ), zero plane displacement ( $d$ ), and $z - d$ along with roughness length ( $z_m$ ) at HP09 and HP11, each year of the study. ....	76

## List of Figures

Figure 1: Climate variables at HP09 from the beginning of measurement in May 25, 2010 to Dec 31, 2013. Panel a) shows daytime 7-day average downwelling photosynthetically active radiation ( $Q_d$ ). In panel b) the bold and thin lines represent 7-day average air temperature ( $T_a$ ) and soil temperature ( $T_s$ ), respectively. Panel c) shows 7-day precipitation ( $P$ ) and panel d) shows 7-day average wind speed ( $u$ ). . 20

Figure 2: Climate variables at HP11 from the beginning of measurement in June 3, 2011 to Dec 31, 2013. Panel a) shows daytime 7-day average downwelling photosynthetically active radiation ( $Q_d$ ). In panel b) the bold and thin lines represent 7-day average air temperature ( $T_a$ ) and soil temperature ( $T_s$ ), respectively. Panel c) shows 7-day precipitation and panel d) shows 7-day average wind speed ( $u$ )..... 21

Figure 3: Energy balance components and surface properties at HP09 from the beginning of measurement in May 25, 2010 to Dec 31, 2013. In panel a), the dotted and solid lines represent 7-day average net radiation ( $R_n$ ) and soil heat flux ( $G$ ), respectively. In panel b), snow depth measured by the CSI SR50 near the flux tower is shown. In panel c), the dotted and solid lines represent 7-day average sensible heat flux ( $H$ ) and latent heat flux ( $\lambda E$ ), respectively. In panel d), the bold and thin line represent leaf area index (LAI) and understory vegetation height ( $height_{us}$ ), respectively. .... 23

Figure 4: Comparison of diurnal energy balance components at HP09 from August 3 or 4 of each year during the study period, which started May 25 2010 and ended Dec 31, 2013. Blue, red, green and teal lines represent net radiation ( $R_n$ ), latent heat flux ( $\lambda E$ ), sensible heat flux ( $H$ ) and soil heat flux ( $G$ )..... 24

Figure 5: Energy balance components and surface properties at HP11 from the beginning of measurement in June 3, 2011 to Dec 31, 2013. In panel a), the dotted and solid lines represent 7-day average net radiation ( $R_n$ ) and soil heat flux ( $G$ ), respectively. In panel b), snow depth measured by the CSI SR50 near the tripod is shown. In panel c), the dotted and solid lines represent 7-day average sensible heat flux ( $H$ ) and latent heat flux ( $\lambda E$ ), respectively. In panel d), the bold and thin lines represent leaf area index (LAI) and understory vegetation height ( $height_{us}$ ), respectively. .... 25

Figure 6: Comparison of diurnal energy balance components at HP11 from August 3 or 4 of each year during the study period, which started June 3, 2011 and ended Dec 31, 2013. Blue, red, green and teal lines represent net radiation ( $R_n$ ), latent heat flux ( $\lambda E$ ), sensible heat flux ( $H$ ) and soil heat flux ( $G$ )..... 26

Figure 7: Energy balance closure (EBC) at HP09 during the growing season (May 1 to September 30) for all years. Dots represent half-hourly flux measurements and the solid and dashed lines are the 1:1 and regression lines, respectively. Also shown are the annual value of EBC and the linear regression equation (with the coefficient of determination).  $T$  is  $H + \lambda E$ ..... 28

Figure 8: Energy balance closure (EBC) at HP09 for all years. Dots represent half-hourly flux measurements and the solid and dashed lines are the 1:1 and regression lines, respectively. Also shown are the annual value of EBC and the linear regression equation (with the coefficient of determination).  $T$  is  $H + \lambda E$ ..... 29

Figure 9: Panel a) shows 7-day average time series of daytime surface conductance ( $G_s$ ) at HP09 (blue lines) and HP11 (red lines), during all years of the study. Half-hourly time series of leaf area index (LAI) and relative water content ( $\theta_r$ ) are shown in panels a) and b), respectively. .... 30

Figure 10: Surface conductance ( $G_s$ ) dependence on photosynthetically active radiation ( $Q$ ) and vapour pressure deficit ( $D$ ) during the 3<sup>rd</sup> growing season (May-Sept) at HP09.  $Q$  and  $D$  are stratified into low (black line), medium (blue line) and high (red line) values:  $Q$ ; 0-500, 500-1500, >1500  $\mu\text{mol m}^{-2} \text{s}^{-1}$  and  $D$ ; 0-1, 1-2, >2 kPa, respectively. .... 32

Figure 11: Surface conductance ( $G_s$ ) dependence on photosynthetically active radiation ( $Q$ ) and vapour density deficit ( $D$ ) during the 3<sup>rd</sup> growing season (May-Sept) at HP11.  $Q$  and  $D$  are stratified into low (black line), medium (blue line) and high (red line) values:  $Q$ ; 0-500, 500-1500, >1500  $\mu\text{mol m}^{-2} \text{s}^{-1}$  and  $D$ ; 0-1, 1-2, >2 kPa, respectively. .... 33

Figure 12: Modelled canopy conductance ( $G_c$ ) as a function of LAI for low (200  $\mu\text{mol m}^{-2} \text{s}^{-1}$ ), medium (1000  $\mu\text{mol m}^{-2} \text{s}^{-1}$ ) and high (2000  $\mu\text{mol m}^{-2} \text{s}^{-1}$ )  $Q$ , represented by the blue, green and red lines, respectively. Panels a, b and c represent the modelled  $G_c$  at low (1 kPa), medium (2 kPa) and high (3 kPa)  $D$ , respectively.  $g_{\text{max}}$ ,  $k_Q$ ,  $Q_{50}$  and  $D_{50}$  were held constant at 14  $\text{mm s}^{-1}$ , 0.60, 200  $\mu\text{mol m}^{-2} \text{s}^{-1}$  and 1 kPa, respectively. .... 34

Figure 13: Panel a) shows ensemble monthly averages of daytime measured (PM calculated) (red) and modelled (blue) surface conductance at HP09 (dots) and HP11 (open circles), during the 3<sup>rd</sup> growing season (1 May – 30 Sept). Panel b) shows ensemble monthly averages of  $D$  at both sites. .... 36

Figure 14: Diurnal measured (blue line) and modelled (red line) surface conductance ( $G_s$ ) for one day from each growing season at HP09. Also shown are PAR ( $Q$ ) and vapor pressure deficit ( $D$ ). (second to fifth years of growth) ..... 38

Figure 15: Diurnal measured (blue line) and modelled (red line) surface conductance's ( $G_s$ ) for one day from each growing season at HP11. Also shown are PAR ( $Q$ ) and vapor density deficit ( $D$ ). (first to third years of growth) ..... 39

Figure 16: Diurnal measured (blue line) and modelled (red line)  $E$ , one day from each growing season at HP09. Also shown are  $E_s$  (black asterisks) and  $E_c$  (dotted green line) components derived from the model. (second to fifth years of growth)..... 40

Figure 17: Diurnal measured (blue line) and modelled (red line)  $E$ , one day from each growing season at HP11. Also shown are  $E_s$  (black asterisks) and  $E_c$  (dotted green line) components derived from the model (1<sup>st</sup> to 3<sup>rd</sup> years of growth)..... 41

Figure 18: Modelled (model) vs. measured (PM) daily  $E$  for the growing season (May-September) of all years at HP09. The solid line is the 1:1 line and the dashed red line represents the regression equation. Also shown is the linear regression equation (with the coefficient of determination)..... 43

Figure 19: Modelled (model) vs. measured (PM) daily  $E$  for the growing season of all years at HP11. The solid black line is the 1:1 line, and the dashed red line represents the regression equation. Also shown is the linear regression equation (with the coefficient of determination). ..... 44

Figure 20: Sensitivity of growing season (May 1 – Sept 30)  $E$  (blue line),  $E_c$  (green line) and  $E_s$  (red line) to model parameters  $k_Q$ ,  $k_A$ ,  $D_{50}$  and  $Q_{50}$  during the 4<sup>th</sup> year of growth at HP09 while maintaining model parameters  $g_{smax}$ ,  $f$  and LAI constant at values given in Table 1..... 45

Figure 21: Annual (Jan 1 –Dec 31) water balance at HP09 from the beginning of measurement in May 25, 2010 to Dec 31, 2013. Precipitation ( $P$ ) and change in soil water storage ( $\Delta W$ ), in panel b) and c), respectively, are constant each year for water balance calculations, represented by a single bar in each year. In panel a) the three color bars, blue, green and magenta, represent  $E$  measured (no EBC correction),  $E$  measured (with EBC correction) and modelled  $E$ , respectively, with the same colors representing the drainage calculated using the respective values of  $E$ . ..... 47

Figure 22: Annual (Jan 1 –Dec 31) water balance at HP11 from the beginning of measurement in June 3, 2011 to Dec 31, 2013. Precipitation ( $P$ ) and change in soil water storage ( $\Delta W$ ), in panel b) and c), respectively, are constant each year for water balance calculations, represented by a single bar in each year. In panel a) the three color bars, blue, green and magenta, represent  $E$  measured (no EBC correction),  $E$  measured (with EBC correction) and modelled  $E$ , respectively, with the same colors representing the drainage calculated using the respective values of  $E$ . ..... 48

Figure 23: Panels a) and b) show the cumulative net ecosystem productivity (NEP) at HP09 and HP11, respectively, during all years of the study period. The 1<sup>st</sup>, 2<sup>nd</sup>, 3<sup>rd</sup> 4<sup>th</sup> and 5<sup>th</sup> years of growth after HP establishment are represented by the red, blue, black, green and cyan lines, respectively. .... 49

Figure 24: Annual sums of NEP, GEP and  $R_e$  during each year of growth at HP09 (blue asterisks) and HP11 (green asterisks). ..... 50

Figure 25: 11° bins of half hourly (May 1- September 30) wind direction for each year at HP09. .... 73

Figure 26: 11° bins of half hourly (May 1- September 30) wind direction for each year at HP11. .... 74

Figure 27: Daytime flux footprint analysis showing the 50, 80 and 90% cumulative turbulent source area for each year at HP09..... 75

Figure 28: Daytime flux footprint analysis showing the 50, 80 and 90% cumulative turbulent source area for each year at HP11..... 76

Figure 29: Tripod on which EC and radiation sensors were initially mount at HP09. .... 77

Figure 30: Scaffold tower used to increase EC and radiation sensor height in response to HP growth at HP09. .... 78

Figure 31: Tripod with guy-wires on which EC and radiation sensors initially mounted at HP11. .... 79

Figure 32: Soil horizon profile (0 - 80 cm) at HP09..... 80

Figure 33: Progression of HP growth throughout the measurement period. Panel a) and b) show HP09 early and late in the 2<sup>nd</sup> year of growth, respectively. Panels c) and d) show HP09 during the 4<sup>th</sup> and 5<sup>th</sup> year of growth. .... 81

Figure 34: Soil horizon profile (0 - 80 cm) at HP11..... 82

Figure 35: Progression of HP growth throughout the measurement period at HP11. Panels a), b) and c) show HP11 during the 1<sup>st</sup>, 2<sup>nd</sup> and 3<sup>rd</sup> growing seasons. .... 83

## LIST OF SYMBOLS AND ACRONYMS

Symbols/Acronyms	Units	Definition
$A$	$\text{W m}^{-2}$	total available energy flux
$A_c$	$\text{W m}^{-2}$	canopy available energy flux
$A_s$	$\text{W m}^{-2}$	soil available energy flux
$C$		carbon
$\text{CO}_2$		carbon dioxide
CFCW		Canadian Wood Fibre Center
$\text{CH}_4$		methane
$c_p$	$\text{J kg}^{-1} \text{K}^{-1}$	specific heat of air at constant pressure
CSI		Campbell Scientific Inc.
$D$	kPa	vapor pressure deficit
DM		dry matter
$D_r$	mm	drainage below the root zone
$D_{50}$	kPa	$D$ when $g_s$ is 50% of $g_{s\max}$
$E$	mm	evapotranspiration
$E_s$	mm	evaporation
$E_c$	mm	transpiration
EBC		energy balance closure
EC		eddy-covariance
FAO		Food and Agriculture Organization
$F_c$	$\mu\text{mol m}^{-2} \text{s}^{-1}$	$\text{CO}_2$ flux density
FMA		forest management agreement
$f$		equilibrium evaporation rate multiplier
$G$	$\text{W m}^{-2}$	soil heat flux density
$G_a$	$\text{mm s}^{-1}$	aerodynamic conductance
$G_c$	$\text{mm s}^{-1}$	canopy conductance
$G_i$	$\text{mm s}^{-1}$	isothermal conductance
GPP	$\text{g C m}^{-2} \text{y}^{-1}$	gross primary productivity
$G_s$	$\text{mm s}^{-1}$	surface conductance
$g_s$	$\text{mm s}^{-1}$	stomatal conductance
$g_{s\max}$	$\text{mm s}^{-1}$	maximum stomatal conductance
$H$	$\text{W m}^{-2}$	sensible heat flux density
HP		hybrid poplar
IRGA		Infrared gas analyzer
$k_A$		canopy extinction coefficient for $A$
$k_Q$		canopy extinction coefficient for $Q$
LAI	$\text{m}^2 \text{m}^{-2}$	leaf area index
MAI	$\text{Mg DM ha}^{-1} \text{y}^{-1}$	mean annual increment

Symbols/Acronyms	Units	Definition
NEE	$\text{g C m}^{-2} \text{ time}^{-1}$	net ecosystem exchange
NEP	$\text{g C m}^{-2} \text{ time}^{-1}$	net ecosystem productivity
$P$	mm	precipitation
PM		Penman-Monteith
$Q$	$\mu\text{mol m}^{-2} \text{ s}^{-1}$	photosynthetically active radiation
$Q_d$	$\mu\text{mol m}^{-2} \text{ s}^{-1}$	downwelling photosynthetically active radiation
$Q_h$	$\mu\text{mol m}^{-2} \text{ s}^{-1}$	$Q_d$ at canopy height
$Q_{50}$	$\mu\text{mol m}^{-2} \text{ s}^{-1}$	$Q$ when $g_s$ is 50% of $g_{s\text{max}}$
$R_e$	$\text{g C m}^{-2} \text{ time}^{-1}$	ecosystem respiration
RH		relative humidity
$R_n$	$\text{W m}^{-2}$	net radiation
$S$	$\text{W m}^{-2}$	shortwave radiation
$s$	$\text{kPa K}^{-1}$	slope of the saturation vapor pressure temperature curve
$T_a$	$^{\circ}\text{C}$	air temperature
$T_s$	$^{\circ}\text{C}$	soil temperature
$u$	$\text{m s}^{-1}$	horizontal wind velocity
$u^*$	$\text{m s}^{-1}$	friction velocity
$v$	$\text{m s}^{-1}$	crosswind velocity
$w$	$\text{m s}^{-1}$	vertical wind velocity
WUE	$\text{g C (kg H}_2\text{O)}^{-1}$	water use efficiency
WUE $_i$	$\text{g C (kg H}_2\text{O)}^{-1}$	intrinsic water use efficiency
$\gamma$	$\text{kPa K}^{-1}$	psychrometric constant
$\lambda$	$\text{J kg}^{-1}$	latent heat of vaporization
$\lambda E_{eq}$	$\text{W m}^{-2}$	equilibrium evaporation rate
$\rho$	$\text{kg m}^{-3}$	air density
$\rho_a$	$\text{kg m}^{-3}$	dry air density
$\rho_Q$		reflection coefficient of $Q$
$\rho_S$		reflection coefficient of $S$
$\theta$	$\text{m}^3 \text{ m}^{-3}$	volumetric water content
$\theta_{fc}$	$\text{m}^3 \text{ m}^{-3}$	$\theta$ at field capacity
$\theta_{pw}$	$\text{m}^3 \text{ m}^{-3}$	$\theta$ at permanent wilting point
$\theta_r$		relative available water

## **Acknowledgements**

I will forever feel grateful for the time and commitment Dr. Andy Black has given me, as it is immeasurable. Although much was expected, Andy's selfless and supportive approach to mentorship allowed me to pursue my passion for learning in a challenging environment without restraint or doubt. Andy is a giant in my eyes. I would also like to extend my gratitude to Rachhpal (Paul) Jassal whose tireless work ethic, initiative, and passion toward science has been extremely inspirational for me.

Endless thanks to Nick Grant and Zoran Nestic whose company I enjoy tremendously. Nick and Zoran, through example, always gave me enormous support regarding my MSc project and, when I showed interest, gave me guidance and the tools necessary to tackle peripheral challenges. Carmela Arevalo, Catherine McNalty, Thierry Varem-Sanders, Jagtar Bhatti and Derek Sidders of the Northern Forestry Centre, all took time away from their lives to assist my project, and for that I am indebted. I am beholden to Newton Philis and Randy Gerylo, of Manitoba Conservation, who were also tremendously generous towards my project and sympathetic when I was in need, treating my project as their own.

Thanks to the Alexis Nakota Sioux First Nation who, through Yellowhead Tribal College, supported me whole-heartedly and conveyed great faith in my ability to succeed at a high level. Finally I would like to thank my friends and family for their relentless support through all of life's challenges, especially Georgeann Jones, Wesley Jones, Clyde Jones, Kateri Jones, Elvie McInerney, Michael McInerney, Kurt Lindal, Rachel Jones, Colleen McInerney, Elvie Clark, Peter Clark Sr., Kathleen Gerwing, Robin Gerwing, Kim Lovich, and Kevin Lovich.

## **Dedication**

To my grandfather, Michael Francis McInerney, who passed away shortly before I began my MSc.

To my father, Wesley Montana Jones, who passed away during my MSc.

# **1 Introduction**

## **1.1 Afforestation, biomass and bioenergy**

Afforestation is planting and/or seeding to establish forests or plantations on land not previously vegetated, classified and/or utilized as forest (FAO 2010). Afforestation of fast growing hybrid poplar (HP) plantations on agricultural land in Canada has the potential to supply renewable sources of wood products, fibre and biomass for bioenergy (Lemus et al. 2005; Larocque et al. 2013). Between 1990 and 2000 approximately 2600 ha were afforested in the Prairie Provinces, of which 2200, 250 and 150 ha were planted in Alberta, Saskatchewan and Manitoba, respectively, and 1200 ha were planted with hybrid poplar (Hall et al. 2004). The planting was done predominantly by Alberta's largest pulp and timber company, Alberta Pacific Forest Industries (Alpac Inc.), for pulp feedstock and to a far lesser extent by farmers seeking to diversify income sources and land management practices (Hall et al. 2004). The impetus for forest product companies to engage in afforestation using HP comes primarily from increased pressure to preserve old growth forest, existence of unfavourable age distributions within current stands and reduced cost associated with log hauling when HP plantations are proximal to mills. Another growing influential driver encouraging plantation forestry in the Prairie Provinces has been oil/gas development and land-use competition, particularly for Alpac Inc. who has a 6.5 million ha forest management agreement (FMA) area that lies within Alberta's 13.8 million ha bitumen reserves (Schneider et al. 2006). In view of the aforementioned trends and the fact that between 2003 and 2007 the average global afforestation rate was 5.6 million ha  $y^{-1}$  (FAO 2010); and it is predicted that by 2020, 44% of global roundwood will be supplied by plantations (FAO 2001), Canada's timber industry may have to follow suite to be competitive economically (Anderson et al. 2012).

HP and willow, both in the *Salicaceae* family, are particularly attractive afforestation species capable of supplying feedstock to the pulp and timber industry because they are fast-growing and can be coppiced, removing the need for multiple planting events. Large phenotypic variation in productivity, growth yield and fibre attributes occurs across soil, climatic gradients, management practices, planting densities and between genotypes, causing certain clonal species to perform best on low elevation mesic sites and others on high elevation xeric sites (Labrecque and Teodorescu 2005; Traux et al. 2012). Under continental climate, irrigated and fertilized 5 year old HP plantation in Wisconsin achieved an above ground mean annual increment (MAI) of 6.7 Mg dry matter (DM) ha<sup>-1</sup> y<sup>-1</sup>, and under oceanic coastal climate in Washington, a 5-year-old HP plantation achieved an MAI of 19-31 Mg DM ha<sup>-1</sup> y<sup>-1</sup> on N-fertilized plots (Hansen et al. 1988; Heilman and Fu-Guang 1993). Trial HP plantations in Canada, particularly throughout Alberta, have demonstrated MAI ranging from 7.6 to 11 Mg DM ha<sup>-1</sup> y<sup>-1</sup> in 4 to 8 year old stands, respectively, which is approximately 8 times the MAI of native trembling aspen and mixedwood stands (Jassal et al. 2014). Considering HP is fast-growing and performs well on marginal agricultural lands (Cai et al. 2011) it seems likely HP will become increasingly desirable as feedstock for bioenergy and for the pulp and lumber industry.

## **1.2 Carbon sequestration and greenhouse gas fluxes**

Additional potential uses for HP plantations, and ecosystem services they could provide, include: native plant habitat (Boothroyd-Roberts et al. 2013); riparian buffering (Fortier et al. 2010); phyto-remediation (Robinson et al. 2007); reclamation (Nave et al. 2013); biomass and soil carbon (C) sequestration (Cai et al. 2011; Jassal et al. 2013). In 2001 and 2002 there was a distinct transition away from white spruce (*Picea glauca*) afforestation in Canada towards HP afforestation, because fast growing HP was identified as a potential fuel alternative to fossil fuels

and a long-term carbon dioxide (CO<sub>2</sub>) sink that would enable Canada to achieve emission reduction commitments under Action Plan 2000 (Hall et al. 2004). Soil C has been shown to decrease during the first 5 years after conversion of agricultural land to HP plantations, after which soil C increased with age (Hansen 1993; Arevalo et al. 2011). In Spain, Sierra et al. (2012) found greater soil C increases in HP plantations compared to corn, particularly at deeper soil depths, along with increased fractions of non-oxidizable soil organic C forms. In Alberta Canada, Cai et al. (2011) found an HP plantation planted on marginal agricultural soil (Class 3, Luvisol) was a large CO<sub>2</sub> source of at least 3.3 Mg C ha<sup>-1</sup> in the 1<sup>st</sup> year of growth and became C neutral in the 5<sup>th</sup> year, whereas Jassal et al. (2013) found an HP plantation planted on high productivity agricultural soil (Class 1, Chernozem) became an annual C sink in the 3<sup>rd</sup> year of growth, demonstrating the variability in growth and C sequestration potential of HP plantations on different soil types. A comprehensive greenhouse gas (GHG) budget study in Belgium, which included measurements of CO<sub>2</sub>, nitrous oxide (N<sub>2</sub>O) and methane (CH<sub>4</sub>) fluxes, showed that an HP plantation quickly became a CO<sub>2</sub> sink in the 2<sup>nd</sup> year after planting, but emissions of N<sub>2</sub>O and CH<sub>4</sub> associated with water table and soil water content fluctuations offset the CO<sub>2</sub> gains and made the plantation a net GHG source (Verlinden et al. 2013; Zona et al. 2103). Studies of this sort emphasize the need to study other important GHG fluxes (i.e. H<sub>2</sub>O, N<sub>2</sub>O and CH<sub>4</sub>) and ecosystem processes (e.g., water balance) in conjunction with C sequestration and productivity to better understand the impacts of HP afforestation on a large scale.

### **1.3 Water balance issues and evapotranspiration modelling**

In Canada's western Prairie Provinces (Alberta, Saskatchewan and Manitoba) fresh water supply for human (e.g. residential, commercial and industrial) and agricultural (e.g. irrigation) use is primarily sourced from Rocky Mountain snowmelt and glacier wastage, which flows

through underground aquifers and the Athabasca, Saskatchewan and Nelson River systems. Considering that increases in vapour pressure deficit ( $D$ ) are projected for the Prairie Provinces, hydrometeorological models predict earlier snowmelt and springtime peak streamflow, accompanied with reduced July-September streamflow in the North and South Saskatchewan river basins (Kienzle et al. 2012; MacDonald et al. 2013). In view of the facts that anthropogenic water use (i.e. irrigation, agriculture, drinking water, oil and gas industry) has increased rapidly throughout the Prairie Provinces and large glaciers supplying the Saskatchewan River system have receded rapidly during the 20th century (Comeau et al. 2009), a fresh water crisis is impending (Schindler and Donahue 2006), which will exacerbate drought periods and negatively affect natural and crop vegetation (Schindler 2000). Dieback and inter-annual variability in the productivity of trembling aspen (*Populus tremuloides*), an important tree species in western Canada, has been documented throughout the Prairie Provinces' aspen parkland and correlated with drought events in areas that receive low precipitation ( $P$ ) and experience high  $D$  (Hogg et al. 2005; Hogg et al. 2008). Eddy covariance (EC) measurements made above trembling aspen (*Populus tremuloides*) at the Southern Old Aspen (SOA) site, one of the Boreal Ecosystem Research and Monitoring Sites (BERMS), in central Saskatchewan, Canada showed a large reduction in gross primary productivity (GPP) in response to water stress during a severe drought in the 2001- 2003 growing seasons (Krishnan et al. 2006).

Sapflow measurements have shown HP can achieve high transpiration ( $E_c$ ) rates ranging from 5 to 8 mm day<sup>-1</sup> for 2 and 13-year-old HP plantations, respectively (Allen et al. 1999; Meiresonne et al. 1999), whereas Black et al. (1996) found a 70-year-old mature trembling aspen stand with a well-established beaked hazelnut (*Corylus cornuta*) understory only reached a maximum total evapotranspiration ( $E$ ) rate of 5-6 mm day<sup>-1</sup>. In semi-arid Mongolia, Wilske et al.

(2009) found  $E$  in a 6-year-old HP plantation exceeded both  $P$  received by the site and  $E$  of a natural shrubland within the same study area. These findings raise concerns regarding the effect that large-scale HP afforestation will have on the stand level and regional scale water balance. In situations where  $E$  exceeds  $P$ , the concern is that HP will utilize groundwater previously inaccessible by shallow rooted species, particularly during drier periods, thereby reducing drainage and streamflow. In Minnesota, HP afforestation has been linked to reduced water yield and annual peak flow in the Red River (Perry et al. 2001), and in the Netherlands, Rijtema and de Vries (1994) measured a 23% reduction in drainage as a result of HP afforestation. In China, where 86% of global afforestation occurs (FAO 2010), Sun et al. (2006) predict that if large-scale HP afforestation continues in China, streamflow will be reduced by 20-40%.

#### **1.4 Objectives**

The Canadian Wood Fibre Centre (CFCW) views the aspen parkland of Canada, a transitional zone between the mixed-grass prairie to the south and boreal forest to the north, as a land base suitable for establishing fast-growing HP on a large scale (Joss et al. 2008) yet there have been few studies that have assessed the long-term C and water balance of HP in the aspen parkland. On marginal land in the aspen parkland of Alberta, Canada, Cai et al. (2011) found that annual  $P$  exceeded  $E$  in the first four years of growth, in which  $E$  varied from 281 mm in the 1st year to 323 mm in the 4th year, but in the 5<sup>th</sup> year of growth there was a drought in which  $E$  exceeded  $P$ . On highly productive agricultural land in Alberta, Jassal et al. (2013) showed  $E$  can exceed  $P$  within 3 years after HP establishment, which emphasizes the need for further research on the C and water balances of HP in the aspen parkland at the stand level so that robust C and  $E$  models can be developed to assess the impacts of HP on regional scales. To contribute to this required research, the objectives of this thesis are to:

- Measure and report the energy, water and C balances of two HP plantations planted on high productivity soil in the aspen parkland.
- Develop and test a robust surface conductance ( $G_s$ ) model capable of partitioning  $E$ , into soil evaporation ( $E_s$ ) and canopy transpiration ( $E_c$ ) components.
- Determine inter-annual variation in the water balance of two HP plantations.
- Study the linkage between C and water balances by assessing the inter-annual variation in HP plantation water use efficiency (WUE).

## 2 Theory

### 2.1 Canopy conductance model

Total latent heat flux ( $\lambda E$ ) from a land surface with plant canopy cover can be partitioned into latent heat flux from canopy transpiration ( $\lambda E_c$ ) and soil evaporation ( $\lambda E_s$ ):

$$\lambda E = \lambda E_c + \lambda E_s \quad (1)$$

Similar to  $\lambda E$  in Eq. (1), which is partitioned into  $\lambda E_c$  and  $\lambda E_s$ , total available energy ( $A$ ) can be partitioned into available energy absorbed by the canopy ( $A_c$ ) and soil ( $A_s$ ), as  $A = A_c + A_s$ . The fraction of available energy absorbed by the soil surface,  $A_s/A$ , is controlled by the attenuation of  $A$  through the canopy as a function of leaf area index (LAI),  $\tau = A_s/A = \exp(-k_A \text{LAI})$ , where  $k_A$  is an extinction coefficient for  $A$ . To complete the energy balance, the fraction of available energy absorbed by the canopy is  $A_c/A = 1 - \tau$ . The partitioning of  $A$  into  $A_s$  and  $A_c$  has strong control over the partitioning of  $\lambda E$  into  $\lambda E_s$  and  $\lambda E_c$  in Eq. (1), of which the latter can be described using the Penman-Monteith (PM) equation:

$$\lambda E_c = \frac{\varepsilon A_c + (\rho c_p / \gamma) \lambda D G_a}{\varepsilon + 1 + G_a / G_c} \quad (2)$$

where  $\varepsilon = s/\gamma$ , given  $s$  is the slope of the saturation vapour pressure vs. temperature curve ( $\text{kPa K}^{-1}$ ),  $s = de^*/dT$ , and  $\gamma$  is the psychrometric constant ( $\text{kPa K}^{-1}$ ),  $\lambda$  is the latent heat of vaporization ( $\text{J kg}^{-1}$ ),  $A_c$  is the available energy flux absorbed by the canopy ( $\text{W m}^{-2}$ ),  $\rho$  is air density ( $\text{kg m}^{-3}$ ),  $c_p$  is the specific heat of air at constant pressure ( $\text{J kg}^{-1} \text{K}^{-1}$ ),  $D$  is the vapor pressure deficit ( $\text{kPa}$ )  $G_a$  is aerodynamic conductance ( $\text{mm s}^{-1}$ ) and  $G_c$  is canopy conductance ( $\text{mm s}^{-1}$ ). Unlike  $A_c$ ,  $D$  and  $G_a$ , which are environmental parameters estimated or measured from radiation and meteorological data,  $G_c$  is a plant physiology parameter meant to describe the integrated leaf-

scale stomatal conductance ( $g_s$ ) response to variables including  $D$ , soil water content ( $\theta$ ) and downwelling photosynthetically active radiation ( $Q$ ). With low  $D$ , adequate  $\theta$  and  $Q$ , leaf stomata may achieve maximum stomatal conductance ( $g_{smax}$ ) but as  $Q$  is absorbed by leaves high in the canopy, less  $Q$  becomes available for absorption by leaves near the soil surface creating a light regime uncondusive to the stomata achieving  $g_{smax}$ , thereby  $g_s$  declines non-linearly through the canopy. An expression for  $G_c$  was derived using a  $g_{smax}$  approach (Dolman et al. 1991; Saugier and Katerji 1991; Kelliher et al. 1995) by integrating  $g_s$  with respect to cumulative LAI from the top of the canopy to the bottom assuming  $Q$  attenuates exponentially downward through the canopy with increasing cumulative LAI and a hyperbolic dependence of  $g_s$  on  $Q$ . An additional Jarvis-Stewart style (i.e., multiplicative) term (see Stewart 1988) accounting for the stomatal response to  $D$  (Leuning 1995; Leuning 2008), which assumes changes in  $D$  affect  $g_s$  at all canopy heights equally, completes the final  $G_c$  model and is written explicitly as:

$$G_c = \frac{g_{smax}}{k_Q} \ln \left[ \frac{Q_{50} + k_Q Q_h}{Q_{50} + k_Q Q_h \exp(-k_Q LAI)} \right] \left[ \frac{1}{1 + D_a / D_{50}} \right] \quad (3)$$

where  $k_Q$  is an extinction coefficient for  $Q$ ,  $Q_{50}$  and  $D_{50}$  are values of  $Q$  and  $D$ , respectively, at which  $g_s$  achieves half its maximum (i.e.,  $g_{smax}$ ) and  $Q_h$  is the value of  $Q$  at the top of the canopy. In this study description of the environmental response of  $G_c$  will be restricted to the use of Eq. (3); however, Wang et al. (2004) developed a similar expression that allows  $Q_{50}$  to vary with canopy depth which would likely be advantageous for some plantation canopies. The use of the Ball-Woodrow-Berry (BWB; Ball et al., 1987) technique to parameterize  $G_c$  (i.e., relating  $G_c$  to the ratio of net assimilation rate of the canopy (or gross ecosystem photosynthesis) to the product of  $CO_2$  concentration and  $D$  (e.g., Blanken and Black 2004; Dolman et al. 2004) will not

be considered in this study but should be considered in future work on characterizing HP plantation  $G_c$ .

## 2.2 Soil evaporation model

When soil water content near the surface of a bare soil is high,  $E_s$ , over a 24-h cycle, is  $R_n$  limited and can be estimated, to a good approximation, by using the equilibrium evaporation rate ( $\lambda E_{eq} = sR_n/(s+\gamma)$ ), which assumes that advection of heat is negligible (Denmead and McIlroy 1970; Priestley and Taylor 1972). At shorter temporal scales (hourly or half-hourly), particularly during the daytime, soil heat flux ( $G$ ) can be large and  $E_s$  is better estimated by  $A_s$  ( $sA_s/(s+\gamma)$ ). As soil water content near the soil surface declines (i.e. due to evaporation, transpiration and drainage)  $E_s$  becomes soil water supply limited (Tanner and Jury 1976) and will achieve a fraction ( $f$ ) of the  $E_{eq}$ , expressed as:

$$\lambda E_s = f \frac{s}{s+\gamma} A_s \quad (4)$$

Here  $f$  is approximated by the relative water content ( $\theta_r$ ) as follows:

$$f = \theta_r = \frac{\theta - \theta_{wp}}{\theta_{fc} - \theta_{wp}} \quad (5)$$

where  $\theta$  is the volumetric water content,  $\theta_{fc}$  is the volumetric water content at field capacity and  $\theta_{wp}$  the volumetric water content at permanent wilting point.

## 2.3 Surface conductance model

As stated in Eq. (1), total  $\lambda E$  from the vegetated surface is the sum of  $\lambda E_c$  and  $\lambda E_s$ , so substituting Eqs. (2) and (4), into Eq. (1),  $\lambda E$  can be expressed as:

$$\lambda E = \frac{\varepsilon A_c + (\rho c_p / \gamma) \lambda D G_a}{\varepsilon + 1 + G_a / G_c} + f \frac{s}{s + \gamma} A_s \quad (6)$$

It can also be expressed using the PM equation with a bulk surface conductance ( $G_s$ ) as follows:

$$\lambda E = \frac{\varepsilon A + (\rho c_p / \gamma) \lambda D G_a}{\varepsilon + 1 + G_a / G_s} \quad (7)$$

It should be noted that  $G_a$  in Eqs. (6) and (7) are slightly different since in Eq. (6) it is the aerodynamic conductance between only the foliage and the atmosphere while in Eq. (7) it is the conductance between soil and foliage and the atmosphere. The differences between the two are expected to be small. The calculation of  $G_a$  is described in the Methods below (Eq. 13).

In order to derive an expression showing the dependence of  $G_s$  on canopy transpiration and soil evaporation parameters, Kelliher et al. (1995) combined Eqs. (6) and (7) as follows:

$$\frac{\varepsilon A + (\rho c_p / \gamma) \lambda D G_a}{\varepsilon + 1 + G_a / G_s} = \frac{\varepsilon A_c + (\rho c_p / \gamma) \lambda D G_a}{\varepsilon + 1 + G_a / G_c} + f \frac{s}{s + \gamma} A_s \quad (8)$$

By recognizing  $G_i = A / [(\rho c_p / \gamma) D]$  as the isothermal conductance with units of diffusive conductance  $\text{mm s}^{-1}$  (Monteith 1965; Monteith 2008) and available energy partitioning definitions,  $\tau = A_s / A$ ,  $1 - \tau = A_c / A$ , they expressed Eq. (8) in dimensionless form before inverting it to provide a six-parameter expression of  $G_s$  containing five parameters,  $g_{s\max}$ ,  $k_A$ ,  $k_Q$ ,  $Q_{50}$ ,  $D_{50}$ , from Eq. (3) and one,  $f$ , from Eq. (4):

$$G_s = G_c \left[ \frac{1 + \frac{\tau G_a}{(\varepsilon + 1) G_c} \left[ f - \frac{(\varepsilon + 1)(1 - f) G_c}{G_a} \right] + \frac{G_a}{\varepsilon G_i}}{1 - \tau \left[ f - \frac{(\varepsilon + 1)(1 - f) G_c}{G_a} \right] + \frac{G_a}{\varepsilon G_i}} \right] \quad (9)$$

The values of the all six model parameters and the sources from which they came can be seen in Table 1. In this study the  $G_s$  model will be assessed by (i) comparing values of  $G_s$  calculated using Eq (9) with those obtained by inversion of Eq (7) and (ii) comparing values of  $E$  calculated using Eq (7) with those measured using EC.  $E$  was obtained by dividing  $\lambda E$  by the latent heat of vaporization ( $\lambda$ ).

Table 1.  $G_c$  and  $G_s$  model input parameters with their respective equations, values and sources.

Parameter	Equation	Value	Source
$g_{smax}$	(3)	14 mm s <sup>-1</sup>	Kim et al. 2008
$Q_{50}$	(3)	100 $\mu\text{mol m}^{-2} \text{s}^{-1}$	Kim et al. 2008
$D_{50}$	(3)	1 kPa	Kim et al. 2008
$k_Q$	(3)	0.6	Leuning et al. 2008
$k_A$	$\tau = A_s/A = \exp(-k_A \text{LAI})$	0.6	Leuning et al. 2008
$f$	(9)	$\theta_r$	Volumetric water content data (m <sup>-3</sup> m <sup>-3</sup> )
LAI	(3) and $\tau = A_s/A = \exp(-k_A \text{LAI})$	Figures 3d and 5d	Barr et al. 2004

### 3 Methods

#### 3.1 Site descriptions

The research involved two study sites: 1) HP09, located at the northwestern edge of the aspen parkland near Edmonton, AB (53° 42' 27.8" N, 113° 37' 46.9" W, 690 m.a.s.l.); and 2) HP11, located at the southeastern edge of the aspen parkland near Winnipeg, MB (50° 03' 8.1" N, 96° 46' 51.9" W, 233 m.a.s.l.), Canada. Both sites experience cold winters and relatively warm summers with moderate precipitation, typical of a continental climate, and differ little with respect to 30-year (1981-2010) mean annual air temperature, which were 3.5 °C and 3.4 °C at HP09 and at HP11, respectively; however, annual precipitation for the same period was significantly higher at HP11 (458 mm) than HP09 (364 mm). The sites are characterized by high-productivity clay loam Chernozemic (class 1) soil (Appendix B.2). Soil samples taken after site preparation, which involved one disk cultivation at 30 cm and a second at 10 cm, showed soil bulk density was lowest in the surface layer (0-5 cm) with values of 900 and 860 kg m<sup>-3</sup> at HP09 and HP11, respectively. At HP09 maximum bulk density, 1370 kg m<sup>-3</sup>, was measured at the deepest soil sampling depth (100 cm), but at HP11 maximum bulk density, 1340 kg m<sup>-3</sup>, was near the 20-cm depth after which it declined with increasing depth. In June 2009 and May 2011, 20 ha and 24 ha area, at HP09 and HP11, respectively, were planted with rooted cuttings of primarily Walker sp. (*Populus deltoides* x *Populus petrowskyana*) at 2 m x 2 m grid spacing. In early May 2010 and June 2011, we began measuring climate variables and EC fluxes of CO<sub>2</sub>, H<sub>2</sub>O vapor and sensible heat above HP09 and HP11, respectively. A detailed description of HP09 site preparation and management along with climate and EC instrumentation preceding 2013 is given in Jassal et al. (2013), but it is worth noting that in June 2013 EC sensors at HP09 were raised to 6 m in response to HP growth. At HP11, EC sensors were positioned at an initial height of 2 m above the soil surface, supported on a horizontal boom extending 1.5 m southwest

from the instrumentation tripod. In June 2013, EC sensors were raised to a height of 3 m in response to HP growth. Site fetch extended 130, 160, 130, 260 m and 340, 100, 330, 270 m in north (N), east (E), south (S) and west (W) directions at HP09 and HP11, respectively. As expected for central Alberta wind predominantly came from the W at HP09, during all years. Daytime flux footprint analysis at HP09 (Appendix A.2) showed the 80% cumulative flux contour was within 150, 100, 200 and 200 m of the EC tower during 2010, 2011, 2012 and 2013, respectively. Given the results of the flux footprint analysis and the westward fetch at HP09 was 260 m, we are confident that source fluxes were from within the HP plantation. At HP11, wind predominantly came from two directions, NW and SE (Appendix A.1), and daytime flux footprint analysis (Appendix A.2) showed that the 80% cumulative flux contour was within 150 m of the EC tower, well within the fetch in NW and SE directions.

### **3.2 Climate measurements**

A humidity and temperature probe (HMP-35C, Vaisala Oyj, Helsinki, Finland) mounted at 2 m height measured half-hourly average relative humidity (RH) and air temperature ( $T_a$ ). A 2-axis sonic anemometer (model M Windsonic, Gill Instruments Ltd., Lymington, UK) mounted at EC instrument height measured half-hourly average horizontal wind speed ( $u$ ) and direction. Precipitation ( $P$ ) was obtained from half-hourly rainfall and snow depth measurements made using a tipping-bucket (0.1 mm) rain gauge (model TR525M, Texas Electronics Inc., Dallas, TX, USA) and a sonic ranging sensor (model SR50, Campbell Scientific Inc. (CSI), Logan, UT, USA) mounted 1.5 m above the ground, respectively. Measurements of half-hourly soil temperature ( $T_s$ ) and volumetric water content ( $\theta$ ) were made at the following depths: 3, 15, 30, 60, 100 cm and 3, 10, 20, 50, 80 cm using copper-constantan thermocouples (model 105T, CSI) and time-domain reflectometer (TDR) probes (model CS616, CSI), respectively. Soil samples

were taken biannually at all sensor depths to determine bulk density and gravimetric water content for the calibration of the TDR probes. Climate variables (including radiation and soil heat flux - see next section) were measured using a datalogger (model CR3000, CSI) and solid state multiplexer (model AM25T, CSI) every 5 seconds, and from these measurements half-hourly averages were calculated and downloaded daily to the UBC Biometeorology and Soil Physics Laboratory using a cellular modem (Raven, model XT, Sierra Wireless Inc., Richmond, BC, Canada). For HP09, half hourly  $P$ ,  $u$ ,  $T_a$  and RH were retrieved from Alberta Agriculture weather stations (<http://agriculture.alberta.ca/acis/alberta-weather-data-viewer.jsp>), the main one being only 1 km away, for gap filling purposes (see below). For HP11, data from Environment Canada weather stations were used, with the two closest stations, Selkirk and Dugald, being located 14 km north and 19 km south of the site, respectively.

### 3.3 Energy balance measurements and closure

The energy balance of a land surface can be written as:

$$R_n = H + \lambda E + G + \Delta S \quad (10)$$

where  $H$  is sensible heat flux and  $\Delta S$  is the change in energy storage between the ground and the height of  $R_n$ ,  $H$  and  $\lambda E$  measurements.  $R_n$  was calculated as the sum of the downwelling shortwave and longwave radiation minus the sum of the upwelling shortwave and longwave radiation. Downwelling and upwelling shortwave and longwave radiation were measured using upward and downward facing pyranometers and pyrgeometers, respectively, with a four-way net radiometer (model CNR1, Kipp and Zonen, The Netherlands) mounted at the 3-m height. Downwelling and upwelling photosynthetically active radiation ( $Q$ ) was measured using a quantum sensor (LI-190, LI-COR Inc.) also mounted at the 3-m height. Five soil heat flux plates

(model HFT3, CSI) at 3-cm depth were located at varying distances from the trees to account for the spatial variability in soil heat flux. The value of  $G$  was obtained by adding to the heat flux plate measurements the rate of heat storage in the 3 cm of soil above the heat flux plate calculated using soil thermocouple and volumetric water content (to obtain the soil heat capacity) data. Energy balance closure (EBC), calculated as  $(H + \lambda E)/(R_n - G - \Delta S)$ , was used to assess the accuracy of the  $H$  and  $\lambda E$  measurements they were not corrected to close the energy balance.

### 3.4 EC instrumentation and flux calculations

EC sensors comprised a 3-axis sonic anemometer (model CSAT3, CSI), an infrared gas analyzer (IRGA), (an open-path sensor, model LI-7500, LI-COR Inc., Lincoln, NE, USA at HP09 and an enclosed-path sensor, model LI-7200, LI-COR Inc. at HP11) and a fine wire (75  $\mu\text{m}$ ) chromel-constantan thermocouple positioned near the sonic array to provide a high frequency (HF) measurement of  $T_a$ . The air flow rate for the LI-7200 was 15 L  $\text{min}^{-1}$ . The distance between the CSAT3 array and both the LI-7500 array and the air intake of the LI-7200 was 15-20 cm to both minimize sensor separation and disturbance of air passing through the sonic array. HF CSAT3, LI-7500, LI-7200 and thermocouple signals were collected on a data logger (model CR3000, CSI) equipped with a CompactFlash module (NL115, CSI) capable of holding 2 megabyte (MB) memory cards, through a synchronous-device-for-measurement (SDM) connection. Sampling frequency at HP09 was 10 Hz in summer and 5 Hz in winter (to save power) while at HP11 it was 5 Hz during 2011 and 2012, and 10 Hz in 2013. Logger calculated half-hourly fluxes of  $\text{CO}_2$ , water vapor and sensible heat were downloaded daily using a cellular modem (Raven, model XT, Sierra Wireless Inc.) connection and raw HF data stored on the CompactFlash memory card was collected every 2-4 weeks, couriered to UBC, after which

fluxes were recalculated and compared to daily logger calculated fluxes at UBC (and used to assess HF data quality).

Half-hourly fluxes of gas constituents, CO<sub>2</sub> ( $F_c$ ) and H<sub>2</sub>O vapor ( $E$ ), were calculated by block averaging the covariance of the vertical wind speed ( $w$ ) and their mixing ratios,  $s_c$  and  $s_H$ , respectively, multiplied by the dry air density ( $\rho_a$ ), e.g., for CO<sub>2</sub>,

$$F_c = \overline{\rho_a w' s_c'} \quad (11)$$

using mixing ratios, rather than densities or mole fractions, accounts for air density effects on fluxes (Webb et al. 1980). No linear detrending of HF data was performed. The overbar and primes denote half-hourly mean and fluctuations from the mean, respectively. Three coordinate rotations were performed on the wind vector components for each half hour, making half-hourly  $\bar{v} = \bar{w} = 0$ , in order to align  $u$  parallel to the mean wind direction and  $w$  normal to the mean wind streamlines (Aubinet et al. 2000). Sensible heat flux was calculated as the covariance of  $w$  and  $T_a$  measured by the sonic anemometer and the covariance of the  $w$  and  $T_a$  measured by the fine wire thermocouple. Net ecosystem exchange (NEE) of CO<sub>2</sub> was calculated as the sum of  $F_c$  and the rate of CO<sub>2</sub> storage change in the air column ( $F_s$ ) between the height of the  $F_c$  measurement ( $h$ ) and the soil surface, i.e.,  $NEE = F_c + F_s$ .  $F_s$  was calculated as the change in the average CO<sub>2</sub> mixing ratio ( $\Delta s_c$ ) between the half hours immediately before and after the given half hour, divided by the change in time ( $\Delta t = 1\text{hr} = 3600\text{s}$ ), and multiplied by  $\rho_a$  and  $h$ , i.e.,  $F_s = \rho_a h (\Delta s_c / \Delta t)$ . Net ecosystem productivity (NEP) was calculated as  $NEP = -NEE$ . Nighttime NEE values, under well mixed conditions, i.e.,  $u^* > u^*_{\text{threshold}}$ , were assumed equal to ecosystem respiration ( $R_e$ ) and were used to develop an annual exponential relationship between  $R_e$  and  $T_s$  and  $R_e$ , which was used to estimate daytime  $R_e$ . Gross primary productivity (GPP) (often referred

to as gross ecosystem photosynthesis, GEP) was calculated by adding daytime NEP to daytime  $R_e$ , i.e.,  $GPP = NEP + R_e$ . GPP gaps were filled using a Michaelis-Menten (rectangular hyperbolic) relationship between GPP and  $Q$ . The  $u^*_{\text{threshold}}$  was found by plotting NEE against  $u^*$  and visually determining the  $u^*$  value at which no further increase in NEE flux values occurred as  $u^*$  increased. For comparison of modelled and measured annual  $E$ , large gaps in daytime  $E$  were filled using linear regression of  $E$  and available energy ( $A$ ), whereas small gaps of two hours or less were filled using simple linear interpolation.

Data quality assurance (QA) was enhanced through the following measurement replications, suitable for data gap filling, and routine comparison of key variables: 1) Two HF measurements of  $T_a$  were provided by the CSAT3 (speed of sound) and chromel-constantan thermocouple, and a third, the half-hourly  $T_a$  measurement, was provided by the HMP35-C sensor; 2) Half-hourly RH was measured by the HMP35-C sensor and derived using the  $H_2O$  mixing ratio from the IRGA; 3) Half-hourly wind speed and direction were replicated using the CSAT 3 and Windsonic anemometers; 4) Downwelling  $Q$  was measured by the LI-190 and routinely compared with downwelling shortwave radiation measured from the CNR-4 sensor since the ratio is relatively constant. Data quality control (QC) was achieved through three stages of data cleaning: 1) First stage “cleaning” involved rejecting HF data if EC instrument diagnostic flags occupied >30% of HF time series or if they exceeded reasonable minimum and maximum bounds on measurement values. Half hourly flux spikes, not removed by the aforementioned method, were also visually inspected and rejected if HF data deviated from the general time series (i.e. non-stationary); 2) Second stage cleaning involved combining data logger calculated, UBC calculated and replicate fluxes, climate and soil values in order to create a near-complete annual dataset; 3) Final calculations (i.e.  $R_e$ , GPP, air-column  $CO_2$  storage) were performed in

the third stage cleaning after small gaps, not filled in second stage cleaning, were filled using linear interpolation, mean diurnal variation or regression methods. All data cleaning, calculations and analysis were performed in MATLAB® (The MathWorks, Inc.).

### 3.5 Water balance

The site water balance is expressed simply as

$$P = E + \Delta W + D_r \quad (12)$$

where  $P$  (mm) is precipitation calculated by adding the calculated increment in snow water equivalent (SWE) and rain-gauge measured rainfall,  $E$  (mm) is evapotranspiration measured using the EC method, and  $\Delta W$  (mm) is the root depth integrated water storage change calculated using measured  $\theta$  data as follows:  $\sum_{(i=1)}^n \theta_i \Delta z_i$ ,  $D_r$  (mm) is the drainage below the root zone calculated as a residual of the water balance ( $D_r = P - E - \Delta W$ ). Since  $\Delta W$  is often negligible, especially when measured over an annual cycle, the water balance equation can be reduced to  $D_r = P - E$  (Jassal et al. 2013). This simplification implies that in situations when  $P$  exceeds  $E$  drainage is positive, meaning water is flowing downward out of the root zone, and when  $E$  exceeds  $P$  drainage is negative, indicating water is flowing upward into the root zone (capillary rise). Due to the limited number of site visits that could be made to maintain drainage sensors and tensiometers, no direct measurement of  $D_r$  was made in this study.

### 3.6 Canopy and boundary layer characteristics

LAI was estimated using an empirical relationship found by Barr et al. (2004) correlating LAI with the ratio of  $Q$  reflectance and shortwave radiation reflectance,  $\rho_Q/\rho_S$ , for trembling aspen. Daily values of  $\rho_Q/\rho_S$  were calculated as the mean of four half hourly  $\rho_Q/\rho_S$  values during the daytime, two before and two after 12 pm (local), which removed reflectance's when the

elevation angle of the sun was low. Linear interpolation of daily values was used to fill non-representative daily values, suitably for modelling work.

The aerodynamic conductance ( $G_a$ ) for sensible heat and mass transfer, corrected for atmospheric stability effects, was calculated as:

$$\frac{1}{G_a} = \frac{u/u_* + 2/k + (\psi_m - \psi_h)/k}{u_*} \quad (13)$$

where  $k$  is the von Kármán constant ( $=0.40$ ),  $u$  is the wind speed,  $u_*$  is friction velocity and  $\psi_m$  and  $\psi_h$  are the stability correction factors for momentum and sensible heat, respectively (Brümmer et al. 2012; Garrett 1978). The stability correction factors were calculated using Monin-Obukhov similarity theory (Monteith and Unsworth 2008). The zero plane displacement height ( $d$ ) was calculated once each year as  $2/3$  of the canopy height ( $h$ ), and was subtracted from instrument height ( $z$ ) to calculate  $z - d$  (Campbell and Norman 1998) (Table 3, Appendix A.3). The degree of coupling between the atmospheric surface layer and vegetation, i.e the relative control of  $G_a$  and  $G_c$  on  $E_c$  was described using the McNaughton and Jarvis (1983) decoupling coefficient, given as:

$$\Omega = \frac{s/\gamma + 1}{s/\gamma + 1 + G_a/G_c} \quad (14)$$

in which  $\Omega$  approaches unity as  $G_c \gg \gg G_a$  implying the atmospheric surface layer and canopy are highly decoupled, and  $G_a$  dominates control over  $E_c$ . In the opposite case, where  $G_c \ll \ll G_a$ ,  $\Omega$  approaches zero indicating  $E_c$  is controlled by  $G_c$  and that the atmospheric surface layer and canopy are highly coupled.

## 4 Results

### 4.1 Weather

During the study period, average  $T_a$  at HP09 (Figure 1) was less than at HP11 (3.8 and 4.6 °C, respectively), yet the coldest seven-day period, in January 2013 (Figure 2), and the coldest half-hourly  $T_a$  value of -38.4 °C, were observed at HP11.

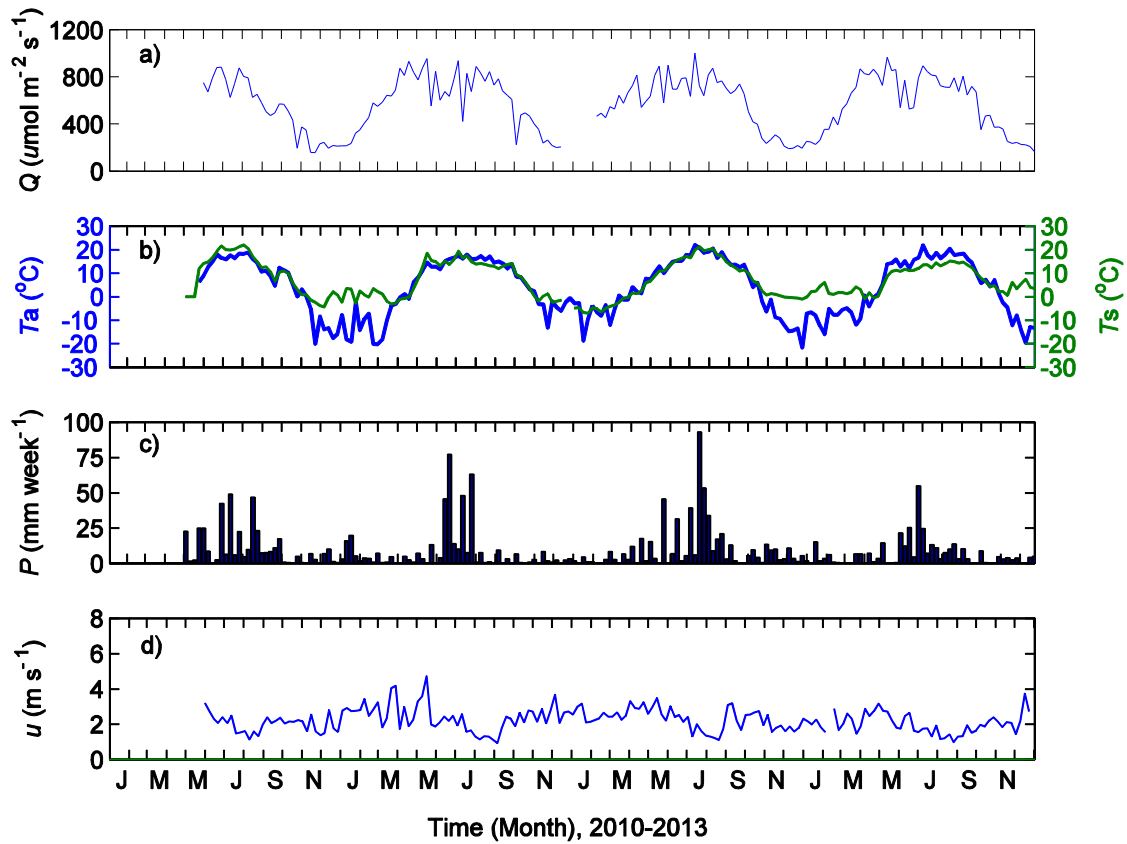


Figure 1: Climate variables at HP09 from the beginning of measurement in May 25, 2010 to Dec 31, 2013. Panel a) shows daytime 7-day average downwelling photosynthetically active radiation ( $Q_d$ ). In panel b) the bold and thin lines represent 7-day average air temperature ( $T_a$ ) and soil temperature ( $T_s$ ), respectively. Panel c) shows 7-day precipitation ( $P$ ) and panel d) shows 7-day average wind speed ( $u$ ).

During each growing season the shallowest depth  $T_s$  measurements at HP09 and HP11 (positioned at 5 and 3 cm, respectively) were similar to and exceeded  $T_a$  at certain times (Figures 1 and 2), which is attributable to low LAI and consequently a relatively high proportion of bare

soil at times (shortly after planting and before leaf emergence or after leaf senescence in each year, and following tillage) throughout the study. The onset of snow in winter caused  $T_s$  to decouple from  $T_a$  (Figures 1 and 2), due to insulative properties of snow, allowing  $T_s$  to remain near freezing ( $0^{\circ}\text{C}$ ) until snowmelt in spring. In contrast, during the winter of 2011/2012 late onset (mid to late November) and a shallow snowpack at both sites caused  $T_s$  to stay coupled with  $T_a$  through much of the winter (Figures 1 and 2).

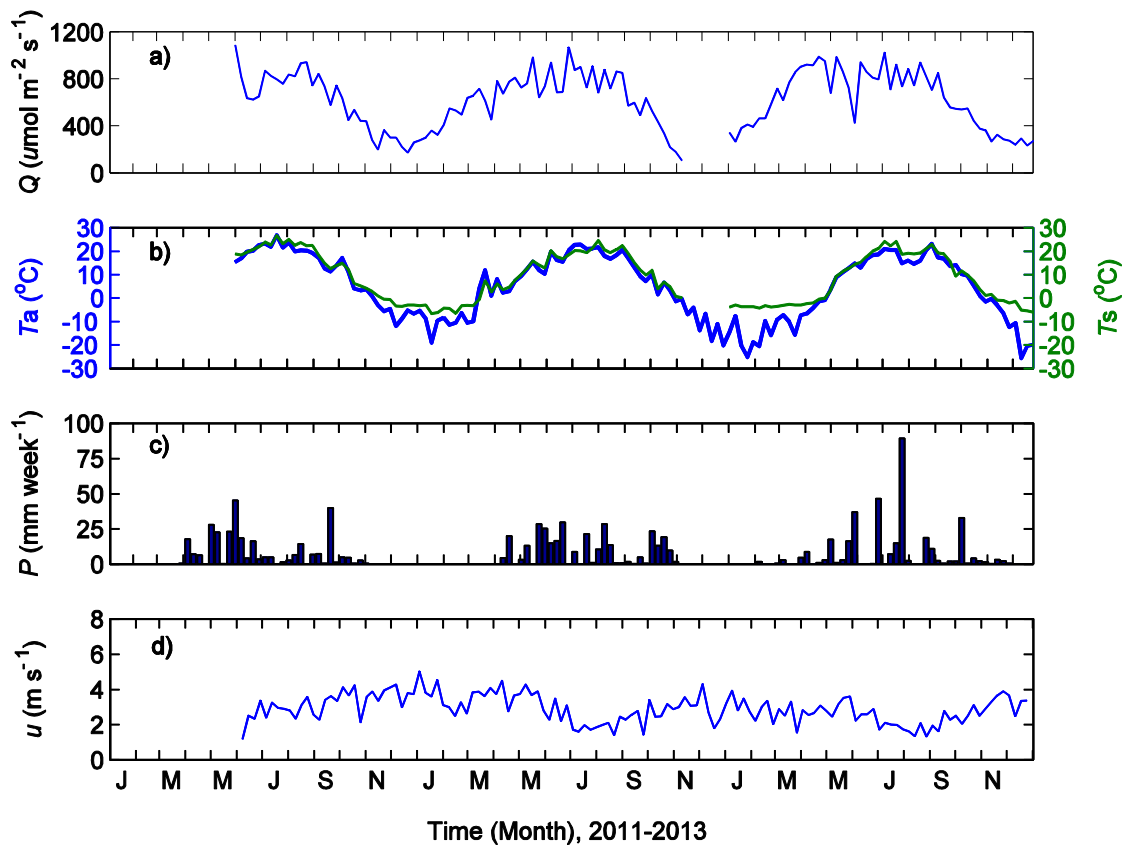


Figure 2: Climate variables at HP11 from the beginning of measurement in June 3, 2011 to Dec 31, 2013. Panel a) shows daytime 7-day average downwelling photosynthetically active radiation ( $Q_d$ ). In panel b) the bold and thin lines represent 7-day average air temperature ( $T_a$ ) and soil temperature ( $T_s$ ), respectively. Panel c) shows 7-day precipitation and panel d) shows 7-day average wind speed ( $u$ ).

Precipitation fell mainly as rainfall between May and August at both sites, but predominantly in June and July at HP09 and May and June at HP11, typically followed by a dry period in August

and July at the respective sites (Figures 1 and 2). Each year during July there was an abrupt reduction in  $u$  (Figures 1 and 2), which was on average higher at HP11,  $2.9 \text{ m s}^{-1}$ , than at HP09,  $2.2 \text{ m s}^{-1}$ , during the study period.

## **4.2 Surface properties and energy balance**

### **4.2.1 Seasonal and diurnal energy balance components**

$R_n$  at both sites typically peaked after the summer solstice in late June through much of July (Figures 3 and 4), temporally adjacent to troughs in  $R_n$  associated with reduced downwelling shortwave radiation ( $S_d$ ) resulting from cloud cover during frequent large storm events during the growing season. As expected, the timing of snowmelt during spring had a large impact on the growing season length because snowmelt decreased surface albedo allowing  $G$  to become positive and provide heat necessary for leaf emergence and plant growth (Figure 3 and 5). As LAI and understory vegetation height began to increase during the growing season resulting in a decrease in  $G$  from its peak in spring, which typically occurred 2 weeks after snowmelt. The growing season ended in late September or early October due to the decline of  $S_d$  and  $T_a$ , which causes  $R_n$  and  $G$  to become negative as the soil surface emits heat accumulated throughout the growing season (Figures 3 and 5). At both sites the Bowen ratio ( $\beta$ ), the ratio of  $H$  to  $\lambda E$ , maintained a value close to 1 following snowmelt, indicating that  $A$  was partitioned evenly between  $H$  and  $\lambda E$ , after which  $\beta$  clearly deviated from 1 (Figure 3 and 5). At HP09, during leaf emergence  $\beta$  declined rapidly as  $\lambda E$  began to dominate  $H$  with abrupt increases in  $\beta$  occurring during cultivation events and dry periods throughout the growing season, particularly in 2013 (Figure 3). At HP11, leaf emergence was delayed, particularly in 2012, and caused  $\beta$  to exceed 1 until leaf emergence when it declined, but rarely below a value of 1 (Figure 5).

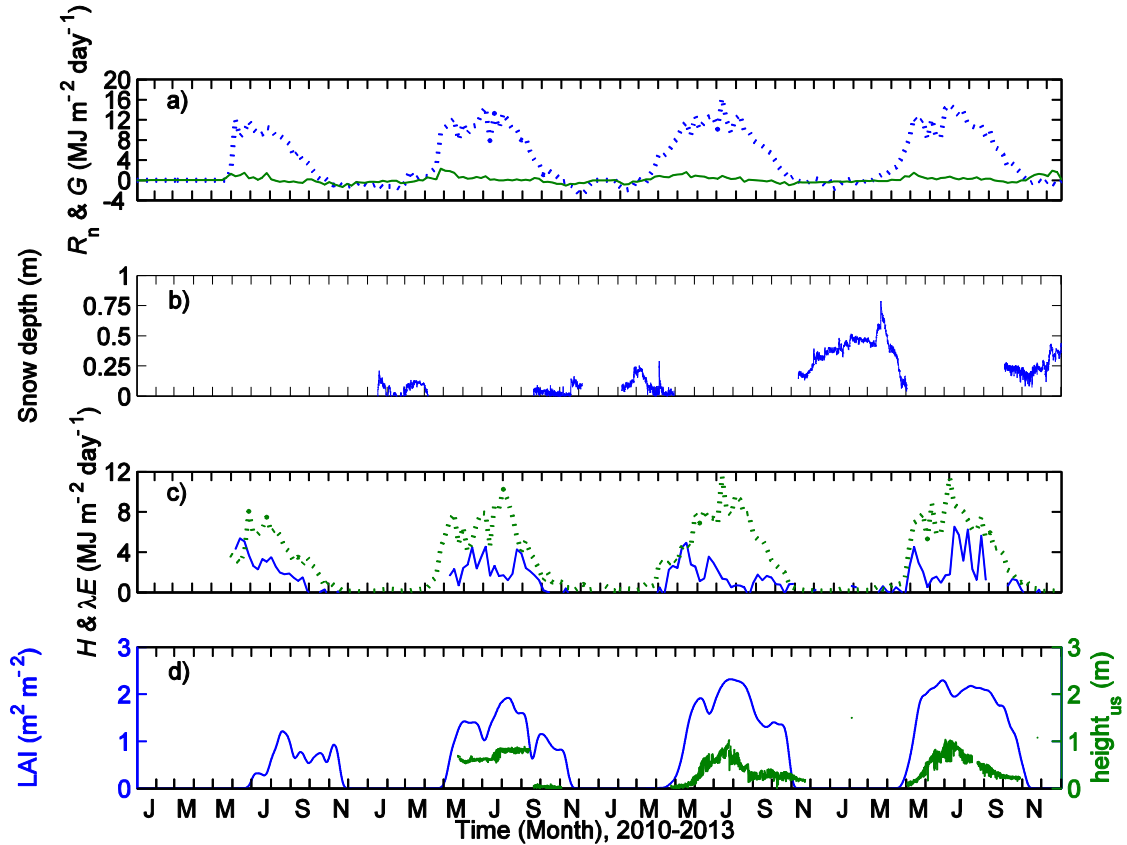


Figure 3: Energy balance components and surface properties at HP09 from the beginning of measurement in May 25, 2010 to Dec 31, 2013. In panel a), the dotted and solid lines represent 7-day average net radiation ( $R_n$ ) and soil heat flux ( $G$ ), respectively. In panel b), snow depth measured by the CSI SR50 near the flux tower is shown. In panel c), the dotted and solid lines represent 7-day average sensible heat flux ( $H$ ) and latent heat flux ( $\lambda E$ ), respectively. In panel d), the bold and thin line represent leaf area index (LAI) and understory vegetation height ( $height_{us}$ ), respectively.

Throughout the study  $\beta$  at HP09 was consistently below 1, reaching values as low as 0.1, whereas  $\beta$  at HP11 was consistently above 1, reaching values as high as 2 for much of 2011, mainly due to drought, followed by a steady decline in subsequent years as the plantation became established and  $\lambda E$  became more dominant (Figures 4 and 6). The aforementioned differences observed between  $\beta$  at HP09 and HP11 can be in part attributed to differences in LAI.

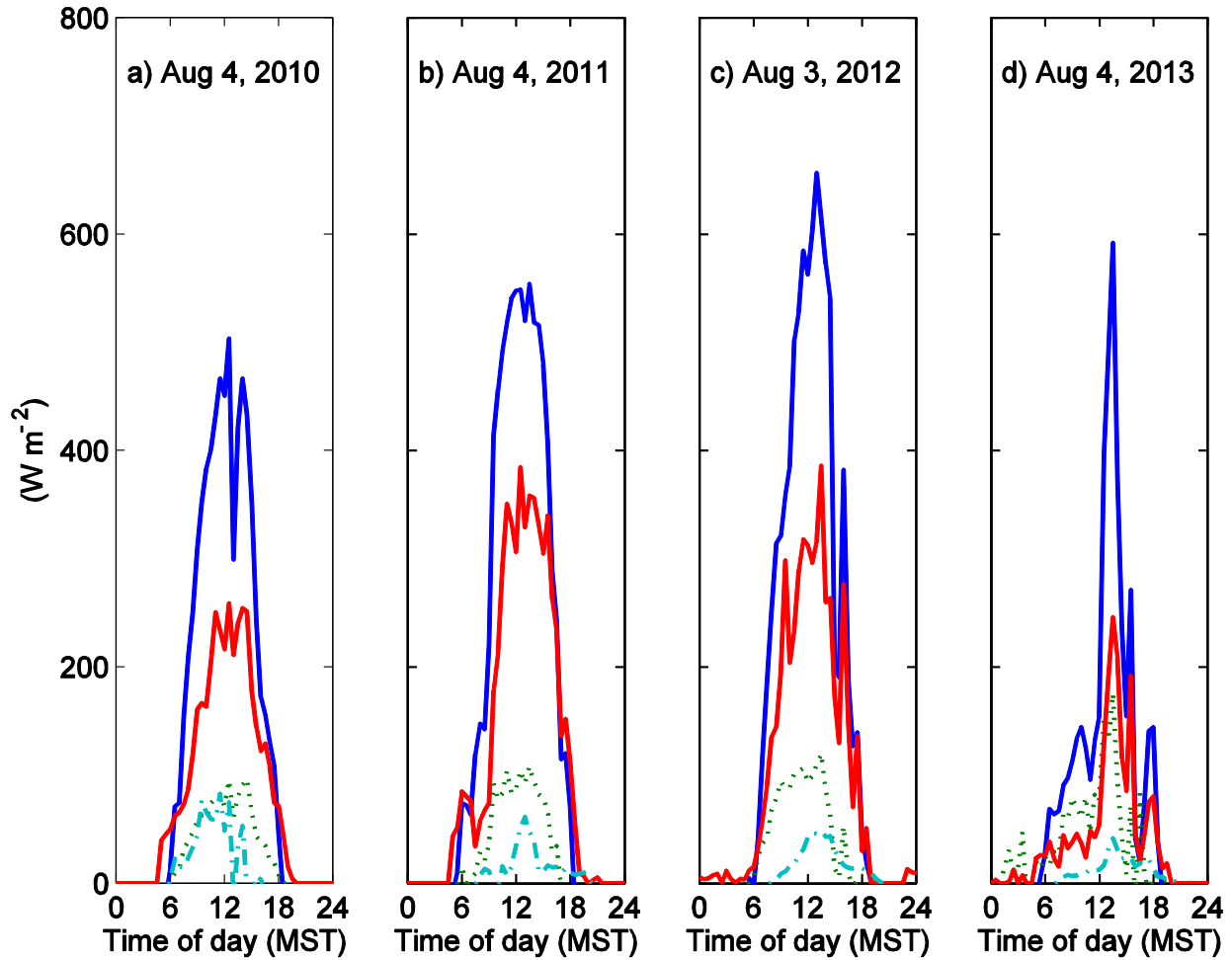


Figure 4: Comparison of diurnal energy balance components at HP09 from August 3 or 4 of each year during the study period, which started May 25 2010 and ended Dec 31, 2013. Blue, red, green and teal lines represent net radiation ( $R_n$ ), latent heat flux ( $\lambda E$ ), sensible heat flux ( $H$ ) and soil heat flux ( $G$ ).

During the 2<sup>nd</sup> year of growth at HP09 and HP11, 2010 and 2012, respectively, LAI was highest at HP11 but in the 3<sup>rd</sup> year of growth, 2011 and 2013, respectively, LAI was higher at HP09 (Figures 3 and 5). The maximum LAI was achieved during July of each year, reaching a maximum for all years of 2.3 and 1.7  $\text{m}^3 \text{m}^{-3}$  at HP09 and HP11 (Figures 3 and 5), respectively, with subsequent declines in LAI due to cultivation events, and/or senescence, which varied temporally from year to year.

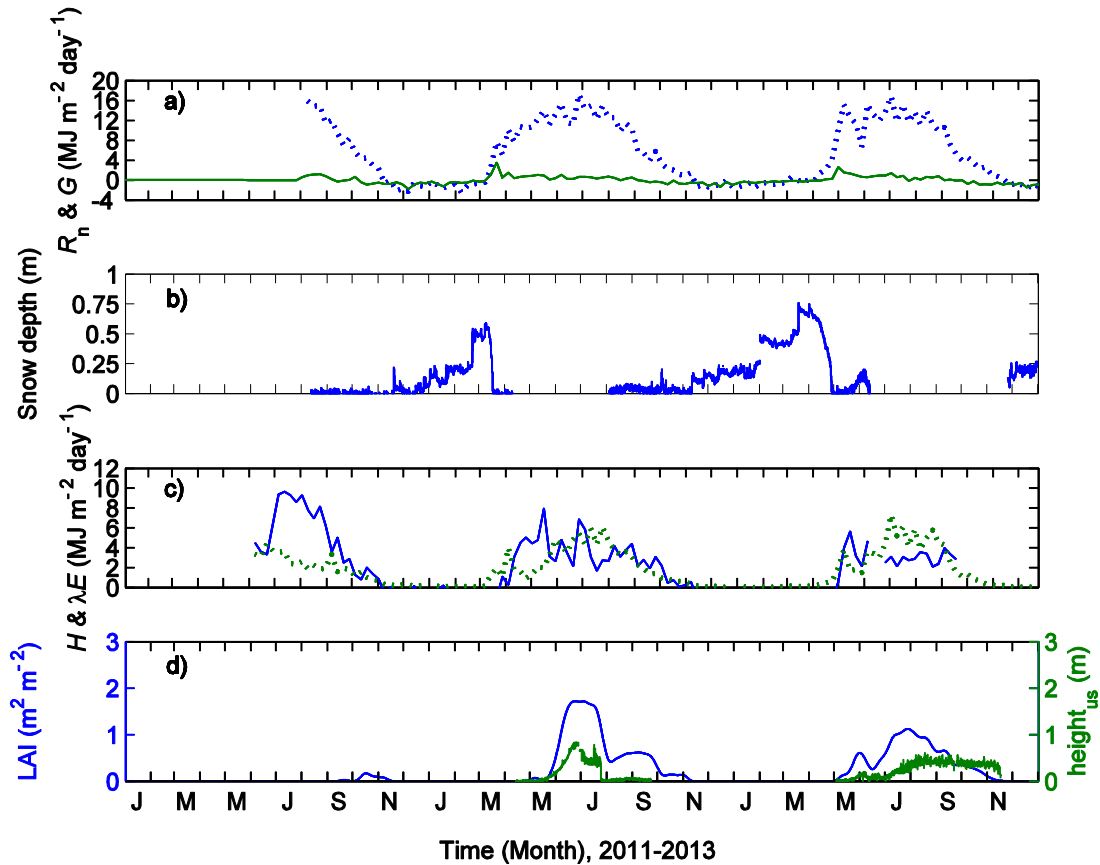


Figure 5: Energy balance components and surface properties at HP11 from the beginning of measurement in June 3, 2011 to Dec 31, 2013. In panel a), the dotted and solid lines represent 7-day average net radiation ( $R_n$ ) and soil heat flux ( $G$ ), respectively. In panel b), snow depth measured by the CSI SR50 near the tripod is shown. In panel c), the dotted and solid lines represent 7-day average sensible heat flux ( $H$ ) and latent heat flux ( $\lambda E$ ), respectively. In panel d), the bold and thin lines represent leaf area index (LAI) and understory vegetation height ( $\text{height}_{us}$ ), respectively.

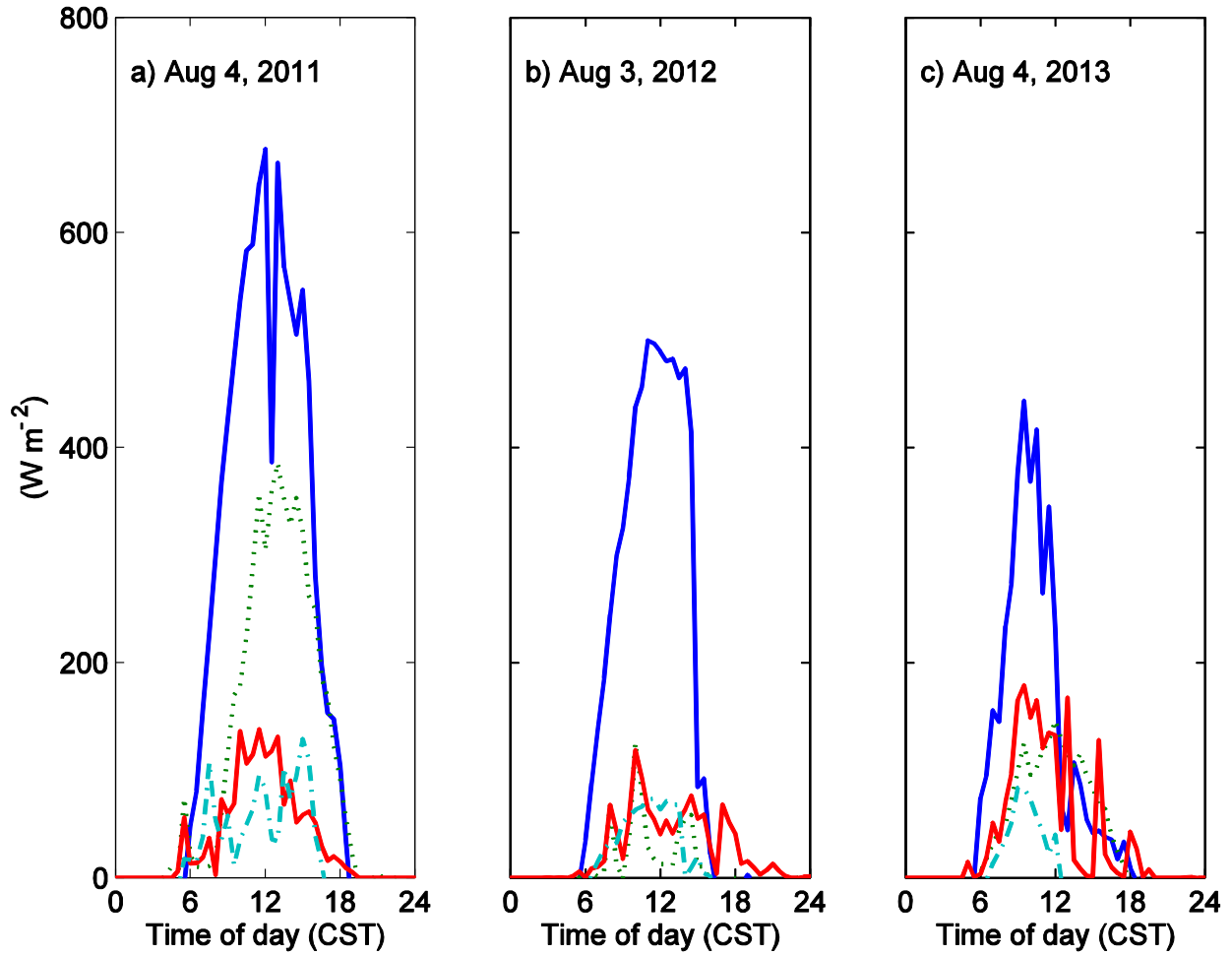


Figure 6: Comparison of diurnal energy balance components at HP11 from August 3 or 4 of each year during the study period, which started June 3, 2011 and ended Dec 31, 2013. Blue, red, green and teal lines represent net radiation ( $R_n$ ), latent heat flux ( $\lambda E$ ), sensible heat flux ( $H$ ) and soil heat flux ( $G$ ).

#### 4.2.2 Energy balance closure

At HP09, the growing season (May 1 to September 30) EBC was consistently good, i.e., close to unity, for all years during the study (Figure 7), where in 2010, 2011, 2012 and 2013 the growing season values of EBC were 0.93, 0.91, 0.87 and 0.92 (Figure 7), respectively. On the other hand, the slope of the regression line ( $H + \lambda E$  vs.  $A$ ) was always less than the EBC, equalling 0.70, 0.82, 0.77, 0.74, and the y-intercepts were large, equalling 21.8, 9.6, 11.3 and 24.0  $\text{W m}^{-2}$ , respectively. At HP11, the energy balance closure fraction was consistently poor, never achieving an energy balance closure fraction over 0.70, measured as 0.67, 0.66 and 0.65 during 2011, 2012 and 2013 (Figure 8). Unlike HP09 the slopes of the regression lines each year, 0.62, 0.62, 0.60 were of equal magnitude to the EBC and the y-intercepts were relatively small, equalling 7.5, 4.2, 5.4  $\text{W m}^{-2}$  in 2011, 2012 and 2013, respectively.

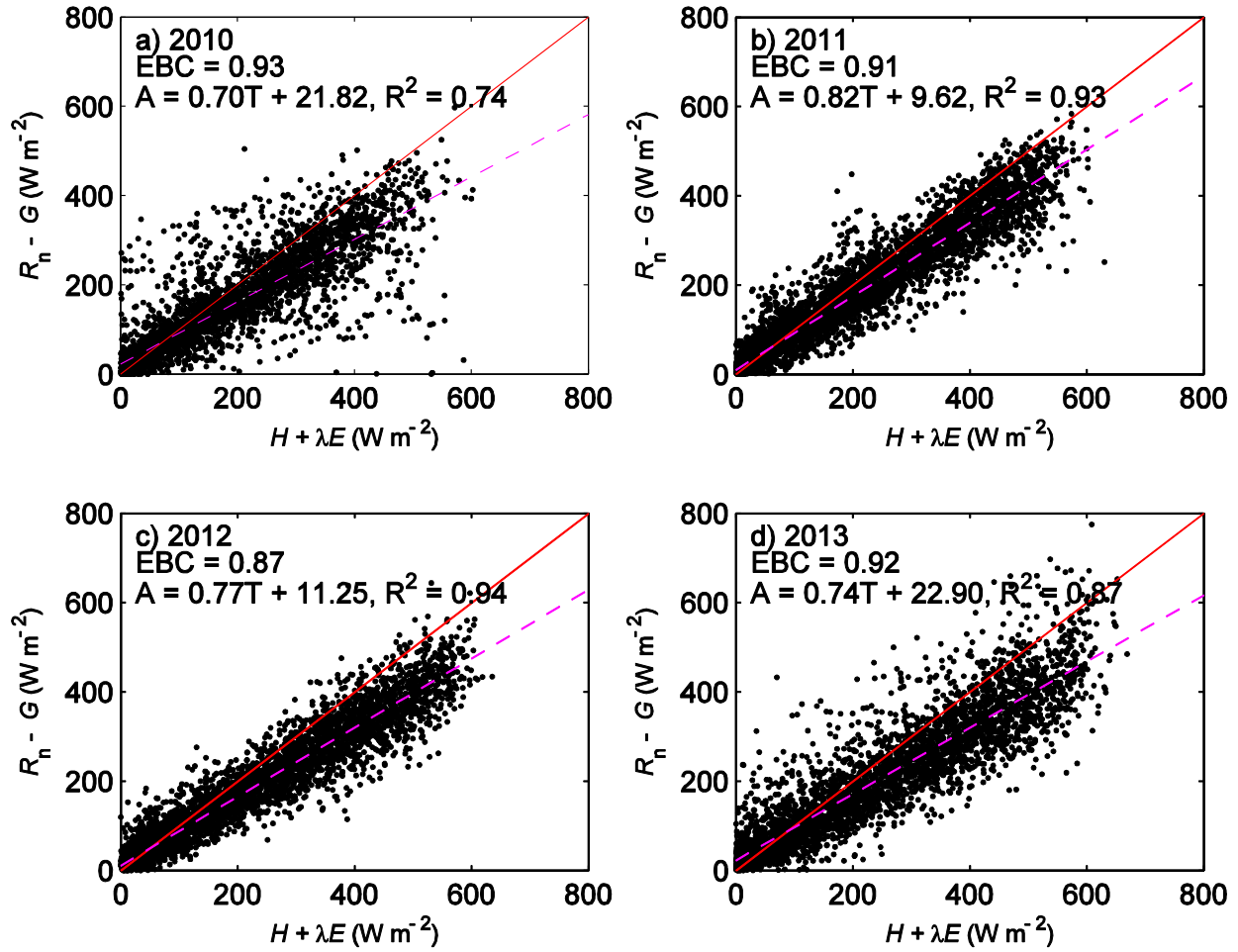


Figure 7: Energy balance closure (EBC) at HP09 during the growing season (May 1 to September 30) for all years. Dots represent half-hourly flux measurements and the solid and dashed lines are the 1:1 and regression lines, respectively. Also shown are the annual value of EBC and the linear regression equation (with the coefficient of determination).  $T$  is  $H + \lambda E$ .

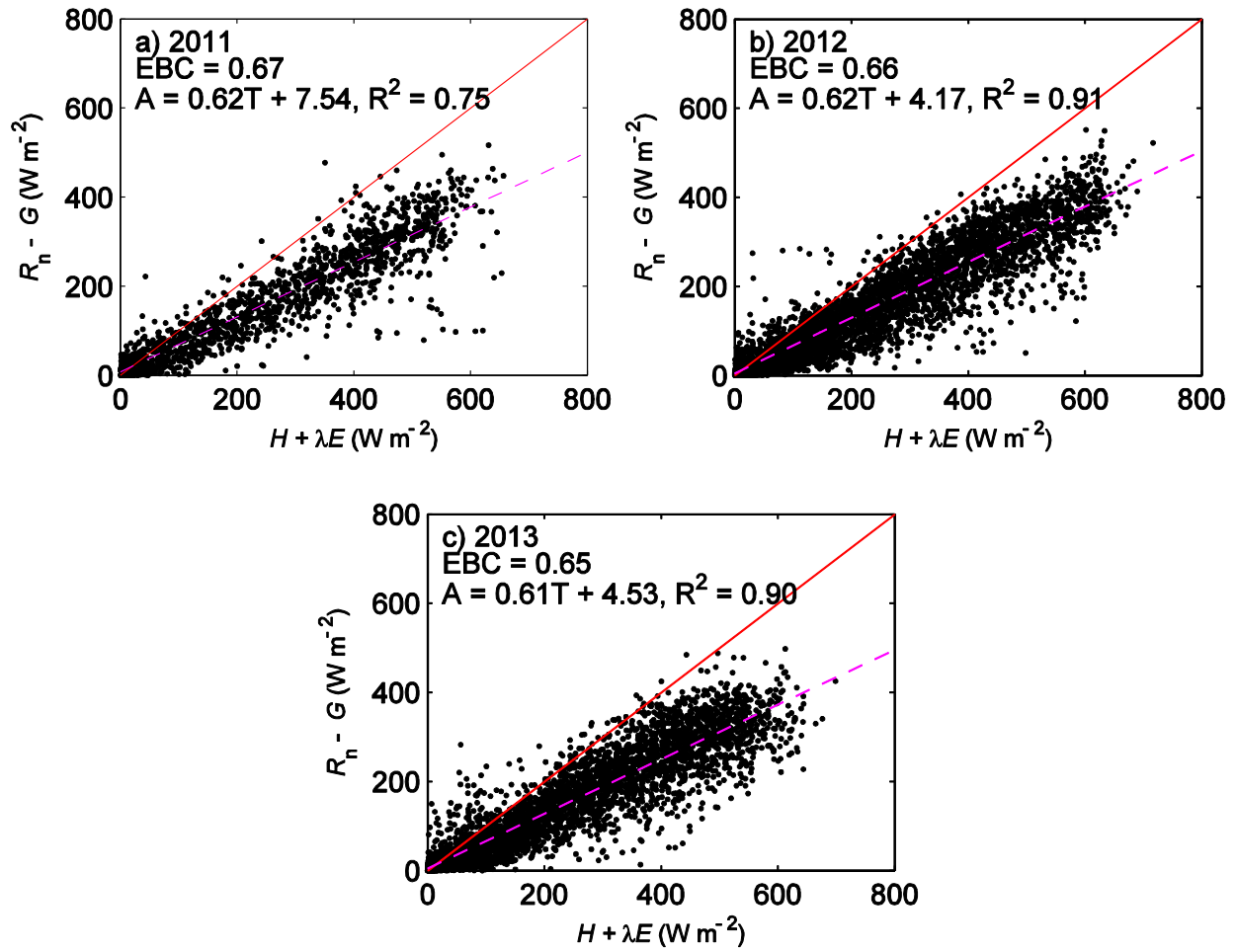


Figure 8: Energy balance closure (EBC) at HP09 for all years. Dots represent half-hourly flux measurements and the solid and dashed lines are the 1:1 and regression lines, respectively. Also shown are the annual value of EBC and the linear regression equation (with the coefficient of determination).  $T$  is  $H + \lambda E$ .

### 4.3 Surface conductance

#### 4.3.1 Seasonal and annual surface conductance

The seasonal patterns of surface conductance ( $G_s$ ), calculated using the inverted Penman-Monteith equation, were consistent from year to year at both sites but there were clear differences between sites, particularly during the growing season (Figure 9a).

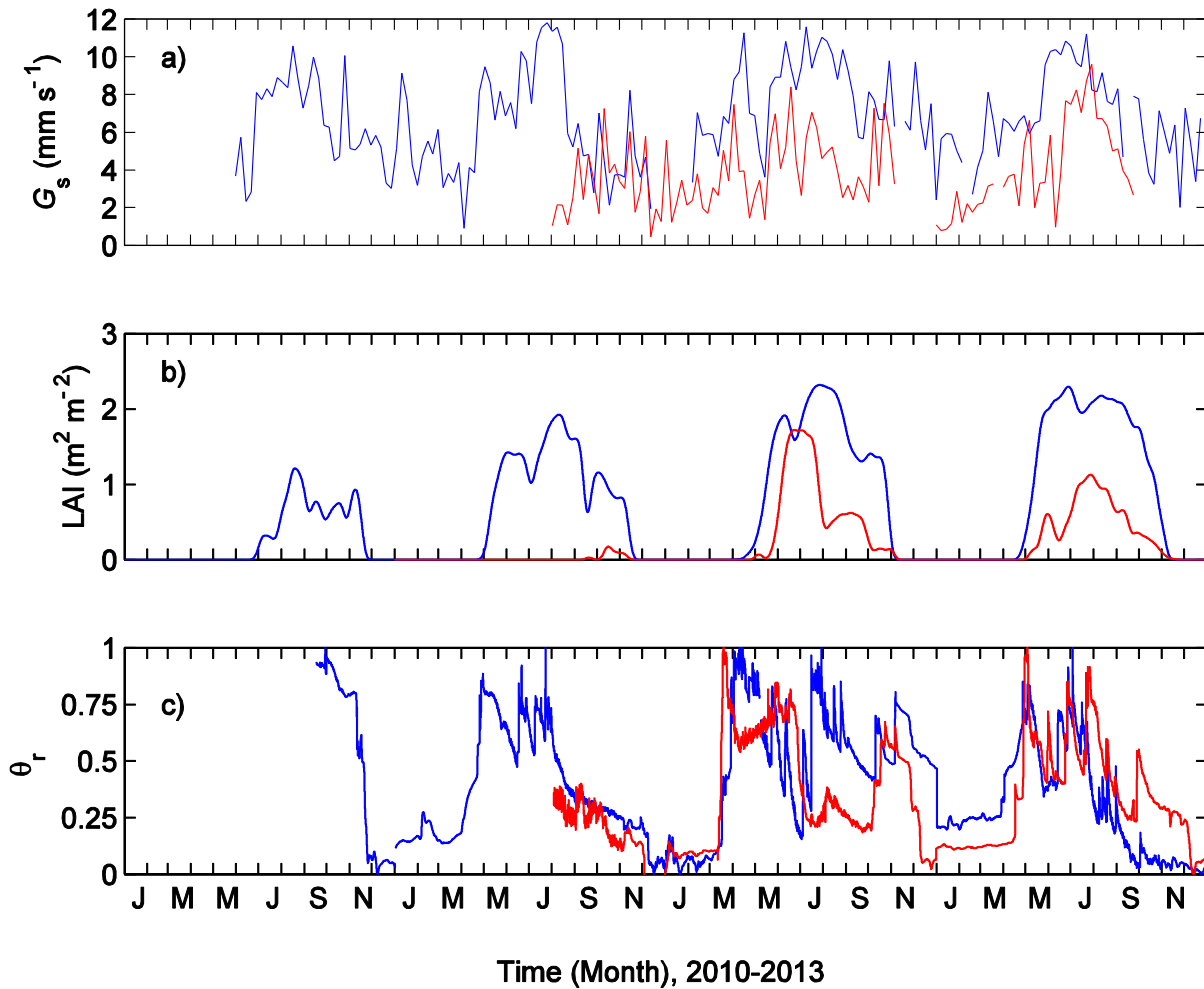


Figure 9: Panel a) shows 7-day average time series of daytime surface conductance ( $G_s$ ) at HP09 (blue lines) and HP11 (red lines), during all years of the study. Half-hourly time series of leaf area index (LAI) and relative water content ( $\theta_r$ ) are shown in panels a) and b), respectively.

During the snow covered dormant season (October 1 –April 30), HP09 and HP11 had similar  $G_s$  values (Figure 9a), most noticeably during winter 2011/2012, which can be expected given

climate and surface characteristics are similar at both sites during these periods (Figures 1 and 2). Typically, during the late dormant season (March 1 – April 31),  $G_s$  spiked, likely a result of sublimation and/or  $E_s$ , as  $T_s$  near the soil surface approached zero, but quickly declined as relative soil water content ( $\theta_r$ ) near the surface declined (Figure 9a and 9c). At both sites, after leaf emergence,  $G_s$  and LAI were correlated and increased linearly until both LAI and  $G_s$  reached their maximum, typically in July, after which  $G_s$  declined sharply due to reduced  $\theta_r$  resulting from high  $E$  and dry atmospheric conditions during late June and early July (Figure 9b). At HP09 intermittent rainfall in late July and early August allowed  $G_s$  to increase again which sustained HP, and understory regrowth after cultivation events, along with LAI until early September each year. At HP11 early rainfall (May) and a lack of summertime rainfall caused  $\theta_r$  and  $G_s$  to decline through July and August, especially in 2012, inducing early senescence which can be seen through decreasing LAI and understory regrowth after cultivation. In 2013, HP11 received less early rainfall and more summertime rainfall than in 2012 resulting in less vigorous growth and LAI development during late June and early July, but more sustained growth and LAI development in August and early September.

#### 4.3.2 Controls on surface conductance

$G_s$  had a strong dependence on  $Q$  and  $D$  at HP09 and HP11 (Figures 10 and 11, respectively), but dependence on  $\theta$  was less clear. Figure 11a shows that at low  $D$  (<1 kPa),  $G_s$  increased almost linearly with  $Q$ , indicating that  $G_s$  was limited by  $Q$  during conditions when  $D$  was low, but at medium (1-2 kPa) and high (>2 kPa)  $D$ ,  $G_s$  began to plateau as  $Q$  reached high levels. This plateauing is indicative of stomatal closure response and/or a soil-surface mulching effect induced by warm and dry atmospheric conditions. This can also be seen at low  $Q$  (0-500  $\mu\text{mol m}^{-2} \text{s}^{-1}$ ) at HP09 (Figure 10b), but more interestingly at all  $Q$  levels at HP11 (Figure 11b).

At HP09, despite  $G_s$  increases observed at  $D < 0.3$  kPa,  $G_s$  generally declined exponentially with increased  $D$  (Figure 10b), but at HP11  $G_s$  declined linearly with increased  $D$  (Figure 11b).

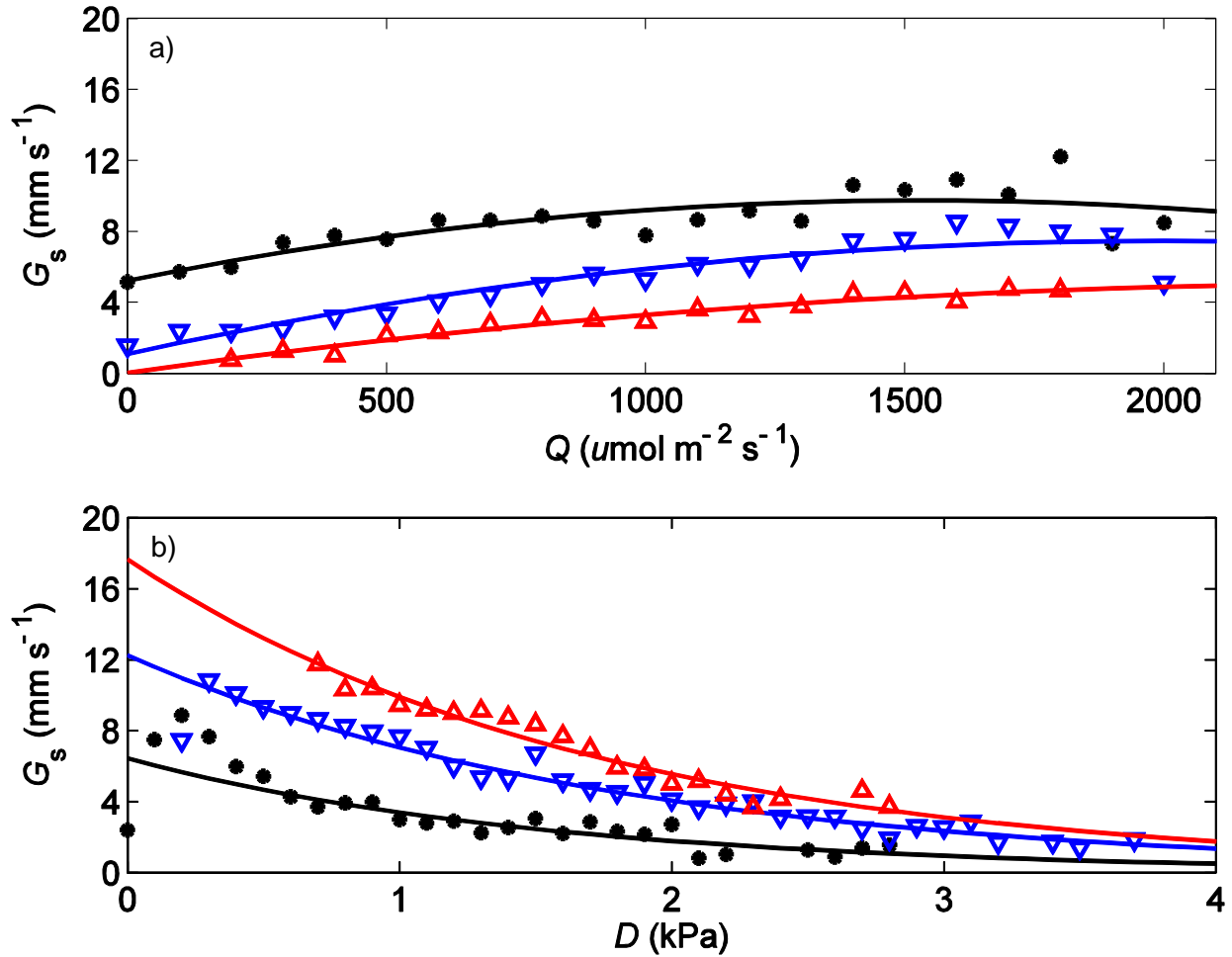


Figure 10: Surface conductance ( $G_s$ ) dependence on photosynthetically active radiation ( $Q$ ) and vapour pressure deficit ( $D$ ) during the 3<sup>rd</sup> growing season (May-Sept) at HP09.  $Q$  and  $D$  are stratified into low (black line), medium (blue line) and high (red line) values:  $Q$ ; 0-500, 500-1500, >1500  $\mu\text{mol m}^{-2} \text{s}^{-1}$  and  $D$ ; 0-1, 1-2, >2 kPa, respectively.

Noting the difference in scale on the vertical axes in Figures 10 and 11 it is clear  $G_s$  at HP11 was systematically lower than at HP09. I hypothesize that reduced  $G_s$  at HP11 was a result of drought stress (Figure 9c) that occurred immediately after plantation establishment, which has had a lasting impacted on stomatal conductance in the following two years.

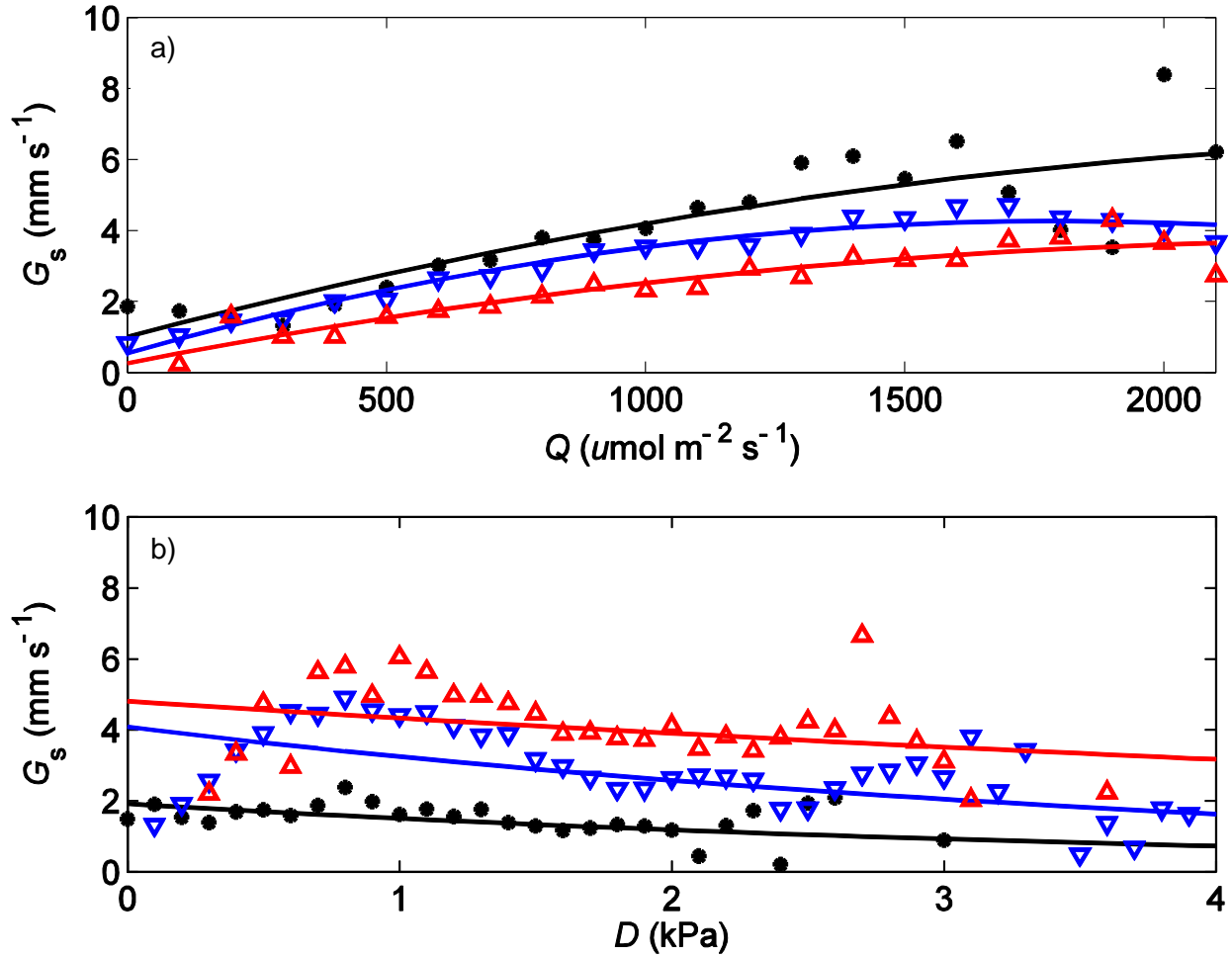


Figure 11: Surface conductance ( $G_s$ ) dependence on photosynthetically active radiation ( $Q$ ) and vapour density deficit ( $D$ ) during the 3<sup>rd</sup> growing season (May-Sept) at HP11.  $Q$  and  $D$  are stratified into low (black line), medium (blue line) and high (red line) values:  $Q$ ; 0-500, 500-1500, >1500  $\mu\text{mol m}^{-2} \text{s}^{-1}$  and  $D$ ; 0-1, 1-2, >2 kPa, respectively.

#### 4.4 Canopy and surface conductance model

##### 4.4.1 Canopy conductance model

Modelled  $G_c$ , calculated using Eq. (3), increased linearly with LAI as it increased from 0 to almost 3 during medium (1000  $\mu\text{mol m}^{-2} \text{s}^{-1}$ ) and high  $Q$  conditions (2000  $\mu\text{mol m}^{-2} \text{s}^{-1}$ ), but it only increased linearly with LAI up to an LAI of 2 during low  $Q$  conditions (200  $\mu\text{mol m}^{-2} \text{s}^{-1}$ ) (Figure 12).

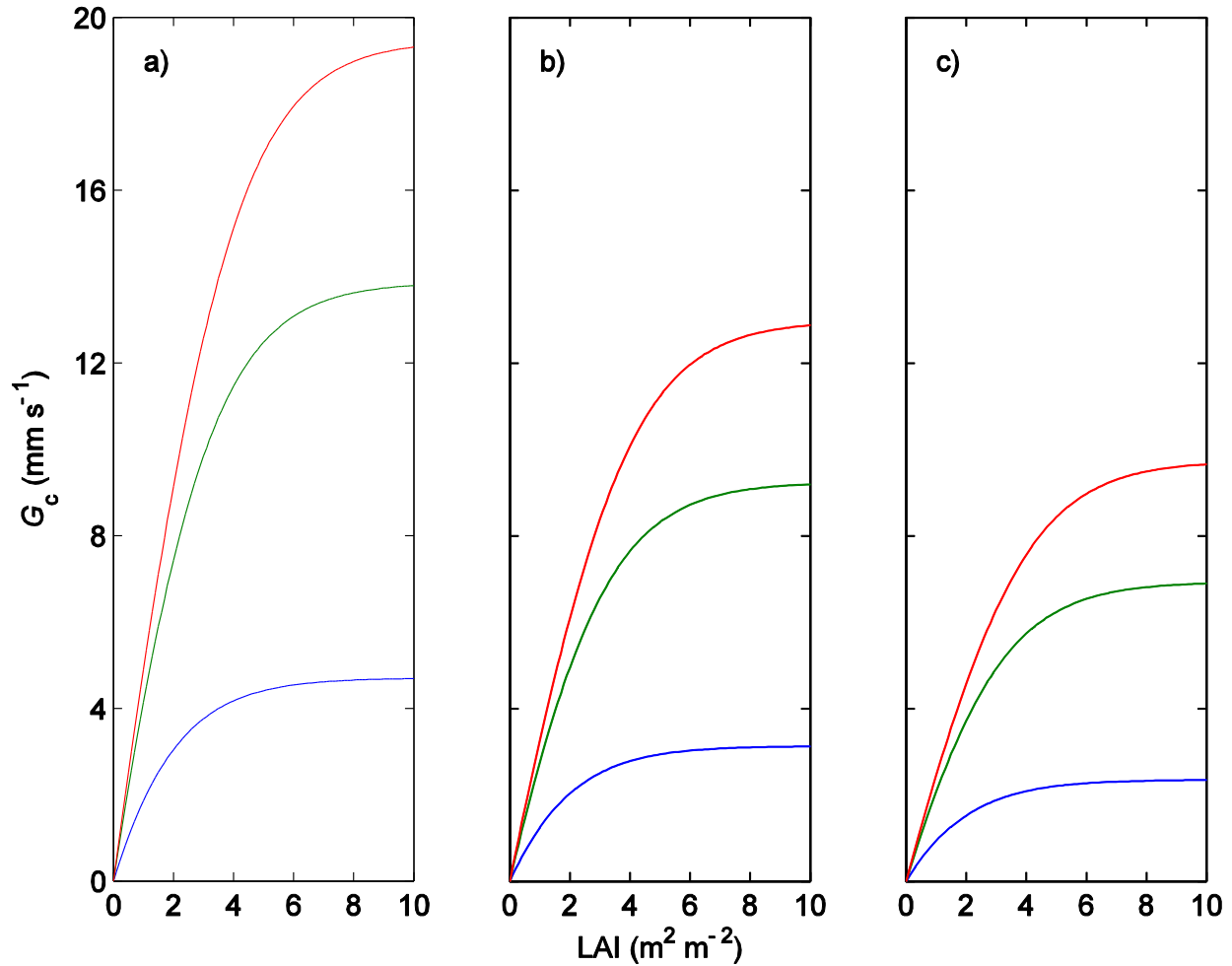


Figure 12: Modelled canopy conductance ( $G_c$ ) as a function of LAI for low ( $200 \mu\text{mol m}^{-2} \text{s}^{-1}$ ), medium ( $1000 \mu\text{mol m}^{-2} \text{s}^{-1}$ ) and high ( $2000 \mu\text{mol m}^{-2} \text{s}^{-1}$ )  $Q$ , represented by the blue, green and red lines, respectively. Panels a, b and c represent the modelled  $G_c$  at low (1 kPa), medium (2 kPa) and high (3 kPa)  $D$ , respectively.  $g_{\text{smax}}$ ,  $k_Q$ ,  $Q_{50}$  and  $D_{50}$  were held constant at  $14 \text{ mm s}^{-1}$ ,  $0.60$ ,  $200 \mu\text{mol m}^{-2} \text{s}^{-1}$  and  $1 \text{ kPa}$ , respectively.

At all levels of  $Q$  and  $D$ ,  $G_c$  began to plateau as LAI exceeded a value of 3, indicative of a  $Q$  saturation effect within the canopy (Figure 12). Conceptually, as LAI increases so too does interception of  $Q$  near the top of the canopy, providing an optimal light regime, which allows stomata of those leaves to achieve high stomatal conductance. Conversely, due to increased  $Q$  interception, stomata on leaves lower in the canopy and close to the bole will receive less  $Q$ , preventing the stomata from achieving high stomatal conductance. The  $G_c$  model achieves its maximum values, at all  $Q$  levels, when  $D$  is low (1 kPa) and declines systemically as  $D$  increases

toward medium (2 kPa) and high (3 kPa)  $D$  (Figure 12). This behavior of the model describes the diminished stomatal conductance resulting from stomatal closure when  $D$  is high, which is observable in the data (Figures 10b and 11b).

#### 4.4.2 Diurnal and seasonal performance of the surface conductance model

Modelled  $G_s$ , calculated using Eq. (7), showed good seasonal and diurnal agreement with  $G_s$  calculated from the inverted PM equation, using EC-measured  $E$  at both HP09 and HP11 (Figures 13, 14 and 15). Each spring (April and May) during the snow free period, pre-leaf-emergence period and the beginning of leaf development,  $D$  was generally low ( $< 1$  kPa) and the diurnal behavior of  $G_s$ , both PM calculated and modelled, was correlated with  $Q$  and more explicitly with  $A_s$  (results not shown). This behavior is expected for PM calculated  $G_s$ , given that our dataset showed that  $G_s$  increased linearly with  $Q$  when  $D$  was low ( $< 1$  kPa) (Figures 10 and 11), and for modelled  $G_s$  by recognizing that when LAI is zero Eq. (6) reduces to Eq. (4) with  $A_s = A$ . Figure 13 shows that during the month of May in the 3<sup>rd</sup> growing season at HP11, in which LAI was low and developing, both  $D$  and measured and modelled  $G_s$  peak near 12:00 Central Standard Time (CST) with  $D$  imposing only slight restrictions on  $G_s$  in the afternoon, creating an almost symmetric increase and decrease in  $G_s$  through the morning and late-afternoon, respectively. Diurnal symmetry was not observed in the 3<sup>rd</sup> growing season during the month of May at HP09, but instead a sharp increase in  $G_s$  observed before 10:00 Mountain Standard Time (MST) was followed by a steady decline in  $G_s$ , as  $D$  began to peak in the afternoon (Figure 13). These observable differences in  $G_s$  during May of the 3<sup>rd</sup> growing season at HP09 are indicative of a stomatal closure response after noon attributable to higher LAI and  $D$  compared to HP11 (Figure 13). At both sites,  $G_s$  increased through June, when there were discrepancies between

measured and modelled  $G_s$  values, until reaching its highest values in July, when there was excellent agreement between measured and modelled  $G_s$ .

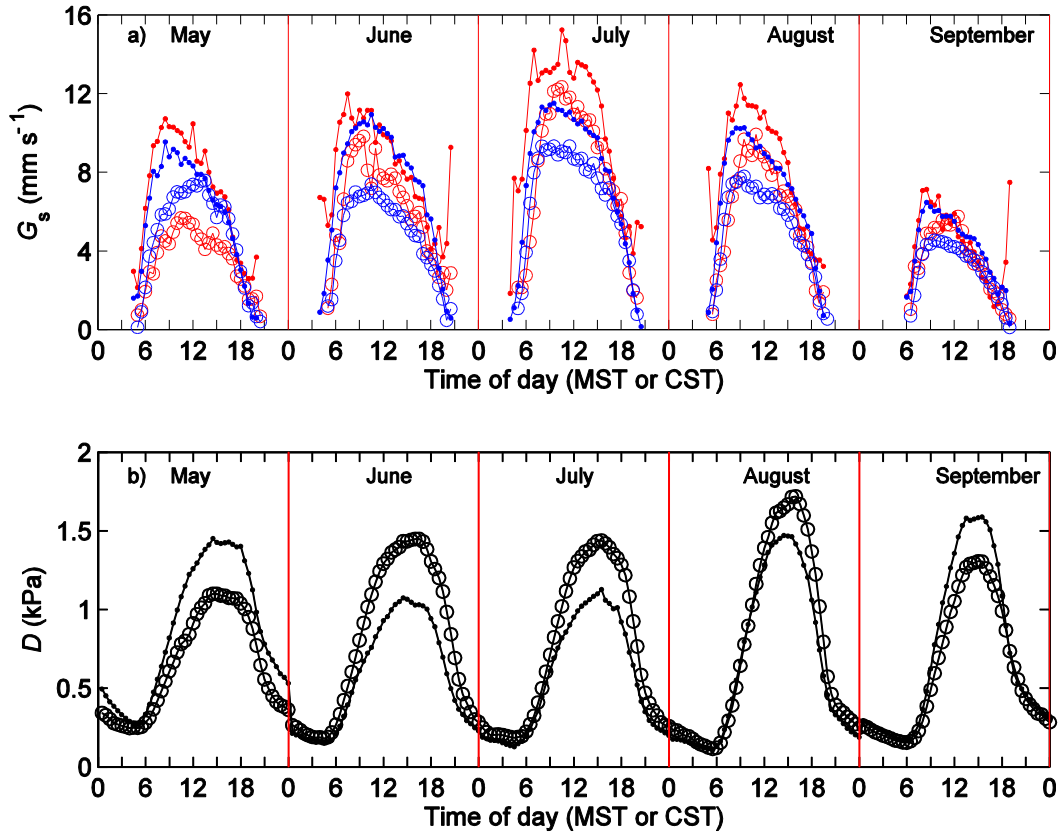


Figure 13: Panel a) shows ensemble monthly averages of daytime measured (PM calculated) (red) and modelled (blue) surface conductance at HP09 (dots) and HP11 (open circles), during the 3<sup>rd</sup> growing season (1 May – 30 Sept). Panel b) shows ensemble monthly averages of  $D$  at both sites.

The diurnal cycles of  $G_s$  during June, July and August were similar between sites despite clear differences in LAI and  $D$ , characterized with morning  $G_s$  maxima of 9-12 and 11-16 mm s<sup>-1</sup>, occurring at 8:00 and 6:00 CST in each month for HP11 and HP09, respectively, followed by an abrupt continuous decline into the afternoon and evening hours (Figure 13). In the month of July, throughout the study period, a clear difference gradually developed between sites regarding the diurnal cycle of  $G_s$ . During July, measured and modelled  $G_s$  at HP11 maintained the typical aforementioned diurnal cycle but at HP09, instead of immediately beginning a steady decline

after the morning maximum, held the maximum near  $12\text{-}14 \text{ mm s}^{-1}$  until 12:00 MST, which I attribute to a site specific soil and atmospheric moisture between sites (Figure 13). Throughout the  $\sim 4$  year study period, June and July rainfall was greater at HP09, (140 and 130 mm, respectively) in the 3<sup>rd</sup> season (Figure 1), which resulted in the average daytime maximum  $D$  remaining low (near 1 kPa) through June and July (Figure 13). In contrast, June and July rainfall at HP11 during the 3<sup>rd</sup> season was low (Figure 2) (50 and 110 mm, respectively), resulting in consistently higher  $D$  with the average daytime maximum near 1.5 kPa, and lower  $G_s$  during the peak growing season (Figure 13). During August  $G_s$  began to decline at both sites as the average daytime maximum  $D$  reached a yearly maximum equal to or greater than 1.5 kPa. Regarding the performance of the  $G_s$  model, discrepancies between measured and modelled  $G_s$  observed in August closely resembled those in June (Figure 13). Of all the five growing season months average daytime maximum  $G_s$  was lowest in September, only achieving a maximum value of  $5\text{-}8 \text{ mm s}^{-1}$ , and was characterized by a diurnal cycle more similar to May than the other three growing season months.

Figures 14 and 15 compare measured and modelled  $G_s$  for a selected day from each growing season for HP09 and HP11, respectively. Both figures show that the  $G_s$  model performs well in reproducing the diurnal course of  $G_s$ . The model clearly accounts for the strong controlling effect of  $D$ .

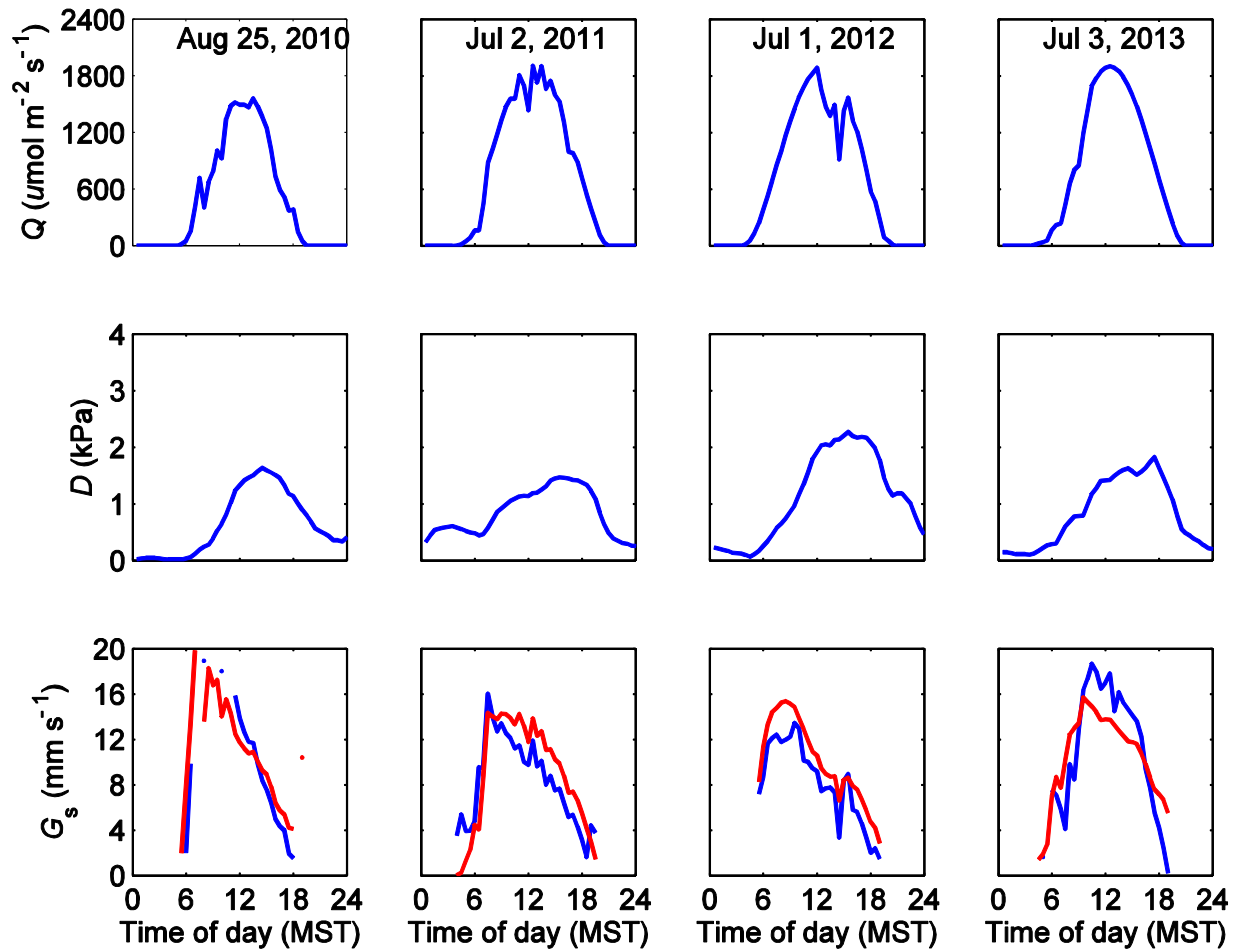


Figure 14: Diurnal measured (blue line) and modelled (red line) surface conductance ( $G_s$ ) for one day from each growing season at HP09. Also shown are PAR ( $Q$ ) and vapor pressure deficit ( $D$ ). (second to fifth years of growth)

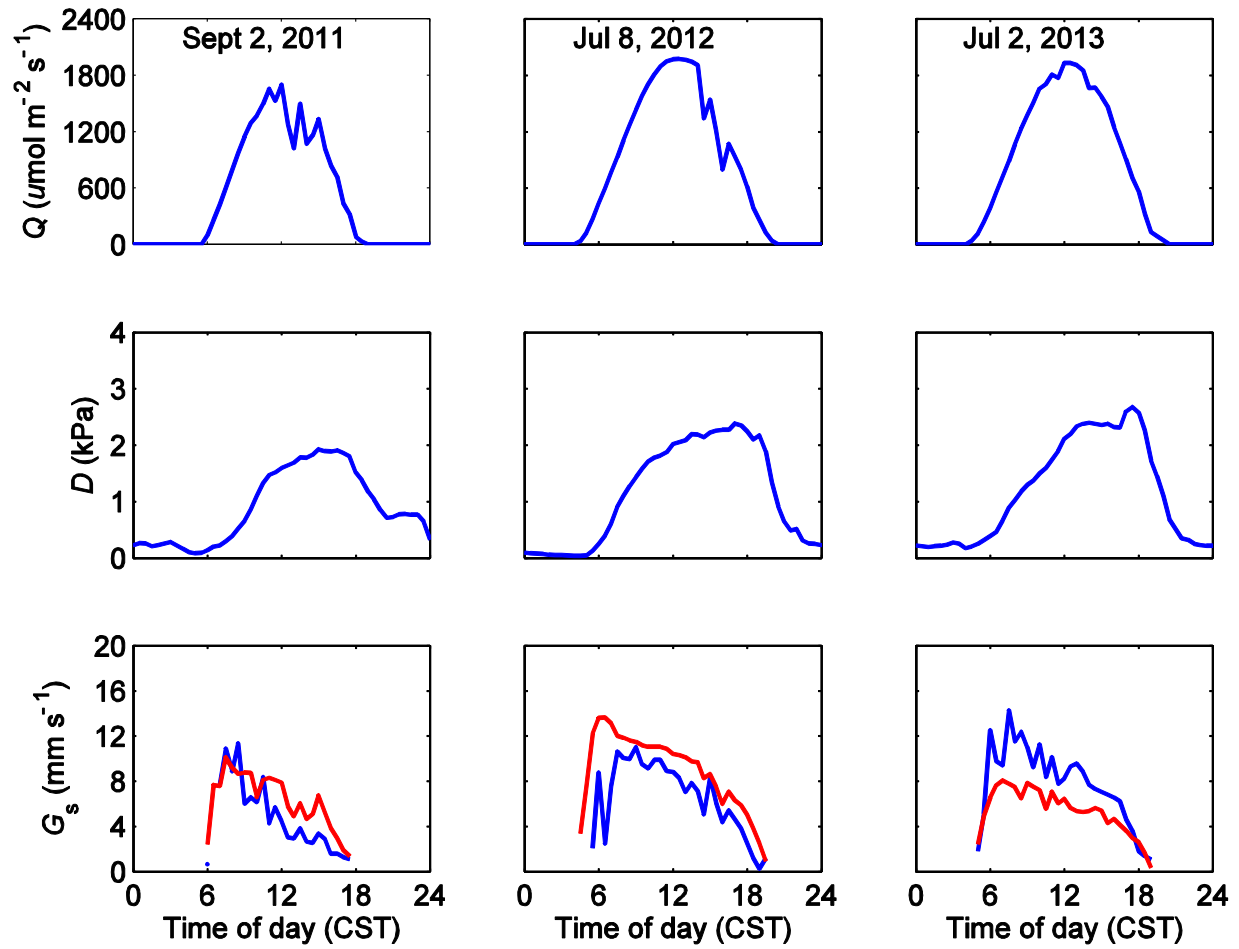


Figure 15: Diurnal measured (blue line) and modelled (red line) surface conductance's ( $G_s$ ) for one day from each growing season at HP11. Also shown are PAR ( $Q$ ) and vapor density deficit ( $D$ ). (first to third years of growth)

### 4.4.3 Diurnal and annual evapotranspiration partitioning

Figures 16 and 17 show the measured and modelled diurnal courses of  $E$  at HP09 and HP11 that correspond to the  $G_s$  values for the same days shown in Figures 14 and 15, respectively, and also show values of  $E_s$  and  $E_c$  calculated using Eqs. (4) and (2), respectively. Unlike  $G_s$ , which typically peaked in the morning,  $E$  typically peaked between 12:00 and 14:00 (MST or CST) when both  $R_n$  and  $G_s$  were high, with the maximum daily measured  $E$  throughout the study being 8.4 and 7.8 mm d<sup>-1</sup> at HP09 and HP11, respectively.

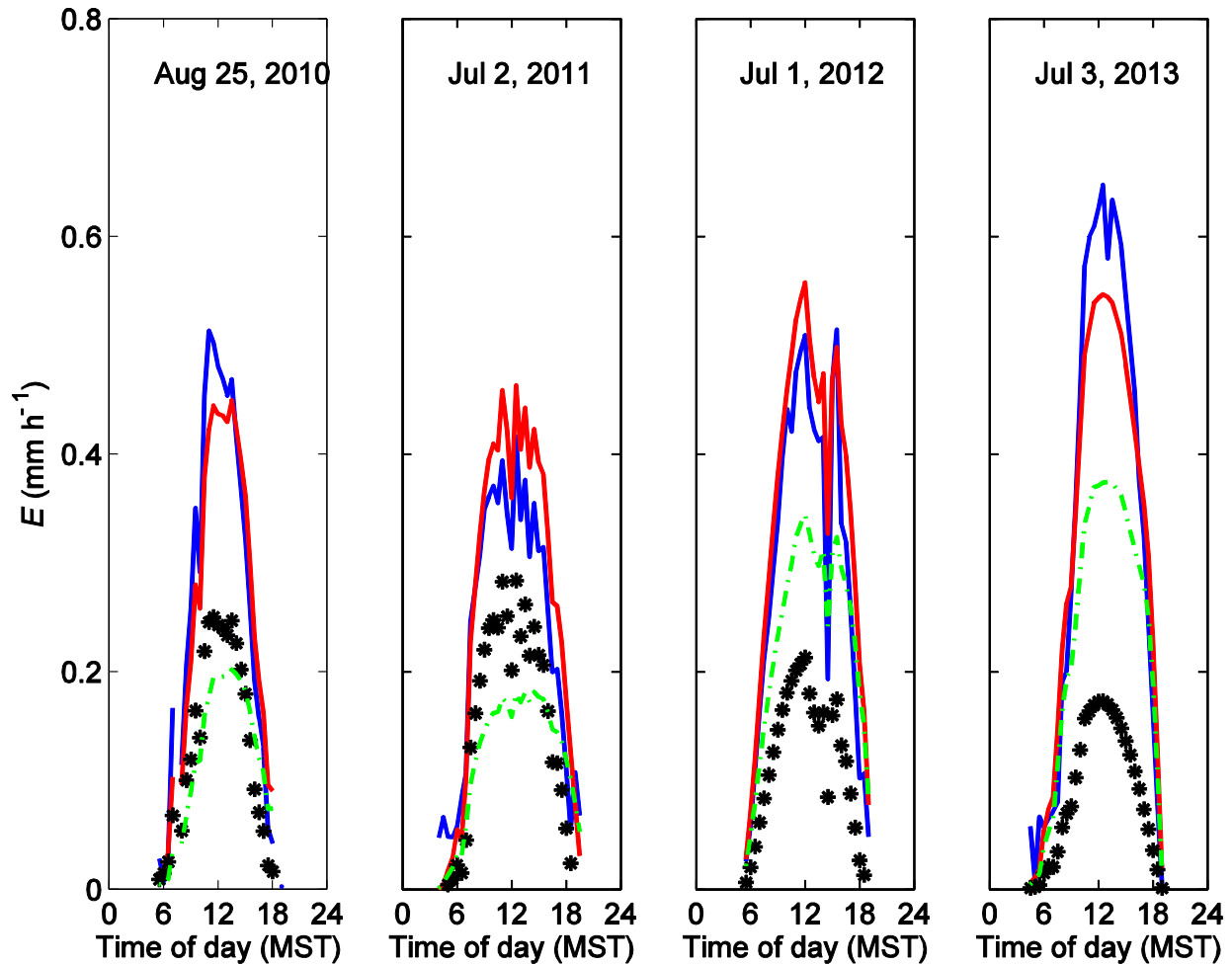


Figure 16: Diurnal measured (blue line) and modelled (red line)  $E$ , one day from each growing season at HP09. Also shown are  $E_s$  (black asterisks) and  $E_c$  (dotted green line) components derived from the model. (second to fifth years of growth)

Based on the diurnal cycle of the modelled  $E$ ,  $E_s$  and  $E_c$  in Figures 16 and 17 the tendency for  $E$  to peak after noon is due to prolonged  $E_c$  rather than  $E_s$  indicating the surface boundary layer and the canopy are highly coupled. In contrast  $E_s$  typically peaked when  $R_n$  peaked, which occurred shortly before or at noon. Figure 17 shows a clear example during 2 September, 2011 at HP11, when the ground was bare, where  $E_s$  and  $E$  are very similar and decline steadily after noon rather than sustaining into the afternoon, as seen in subsequent years with vegetation.

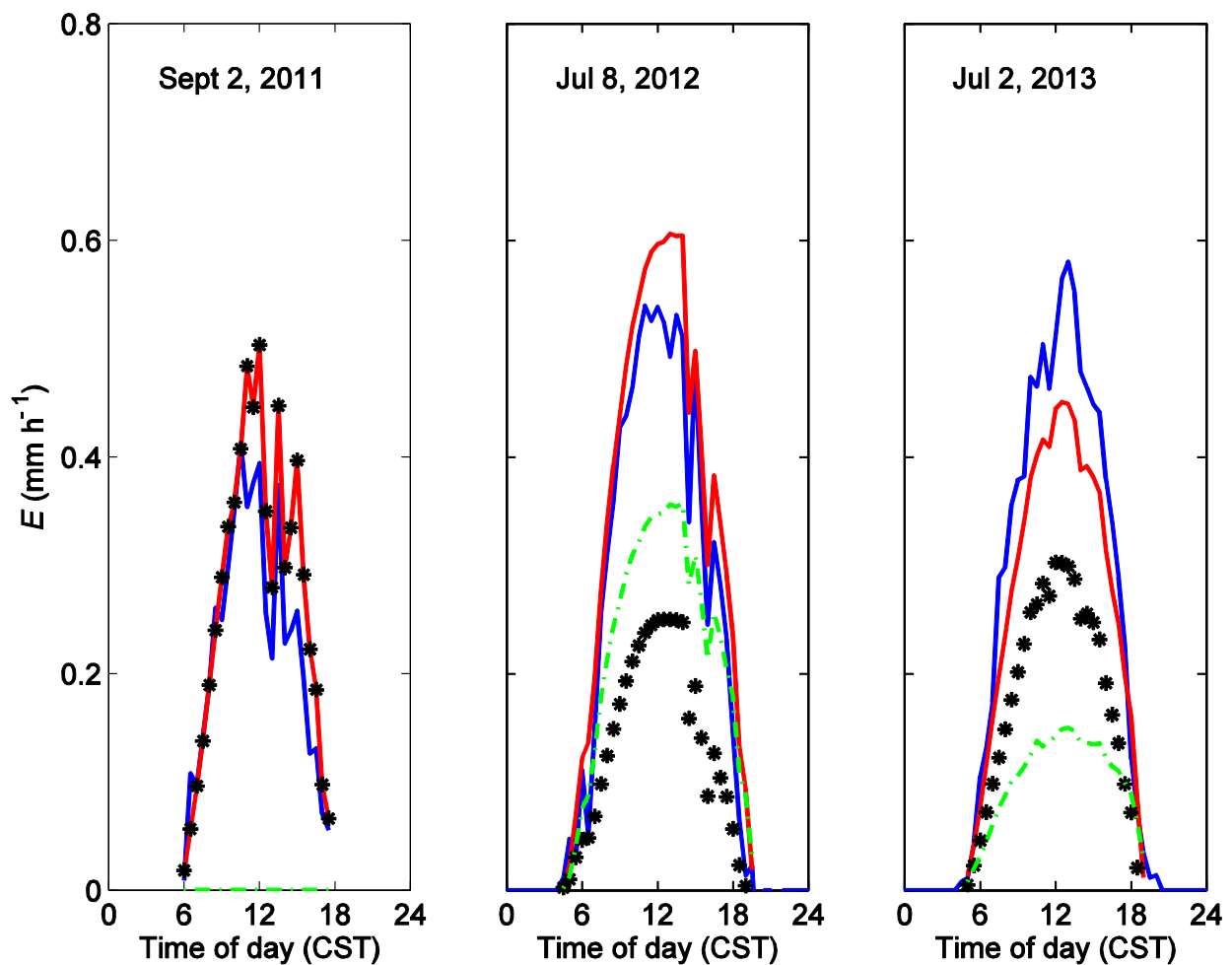


Figure 17: Diurnal measured (blue line) and modelled (red line)  $E$ , one day from each growing season at HP11. Also shown are  $E_s$  (black asterisks) and  $E_c$  (dotted green line) components derived from the model (1<sup>st</sup> to 3<sup>rd</sup> years of growth).

The degree of coupling between the surface boundary layer and the surface (i.e., value of the decoupling coefficient,  $\Omega$ ) also changed seasonally, particularly after the 1<sup>st</sup> year of growth, maintaining a high value during the snow and pre-leaf-emergence period (i.e.,  $\Omega$  high), when  $E_s$  dominated  $E$ , followed by a gradually lower value as the LAI and  $E_c$  became a larger proportion of  $E$ . At HP09,  $E$  was partitioned almost equally between  $E_s$  and  $E_c$  in the 2<sup>nd</sup> growing season (2010), but in the subsequent 3<sup>rd</sup>, 4<sup>th</sup> and 5<sup>th</sup> growing seasons  $E_c$  dominated the  $E$  flux, exceeding  $E_s$  during the growing season and annually, as  $E_c$  increased and  $E_s$  decreased every year after HP establishment. In the 1<sup>st</sup> growing season at HP11  $E_s$  accounted for 202 mm of the 204 mm total  $E$  measured between 8 August and 31 Dec, 2011, with only 2 mm occurring as  $E_c$ . Despite  $E_c$  increasing in magnitude in the following 2<sup>nd</sup> and 3<sup>rd</sup> growing seasons at HP11,  $E_s$  remained dominant over  $E_c$ , which only accounted for 153 mm of the 364 mm total  $E$  flux in the 3<sup>rd</sup> season. On an annual basis total daily daytime  $E$  calculated, by substituting  $G_s$  from the  $G_s$  model (Eq. (9)) into the Penman-Monteith equation, showed good agreement at both sites with total daily daytime  $E$  measured using the EC technique but clearly agreement was better at HP09 compared to HP11 (Figures 18 and 19). During all four years at HP09 measurements and modelled annual agreement was excellent, with the slope of the regression exceeding 0.85 every year (Figure 18). At HP11, annual agreement between measured and modelled daily  $E$  was poorer, particularly during the 1<sup>st</sup> and 2<sup>nd</sup> growing season, but steadily improved and eventually achieved good agreement in the 3<sup>rd</sup> year of growth.

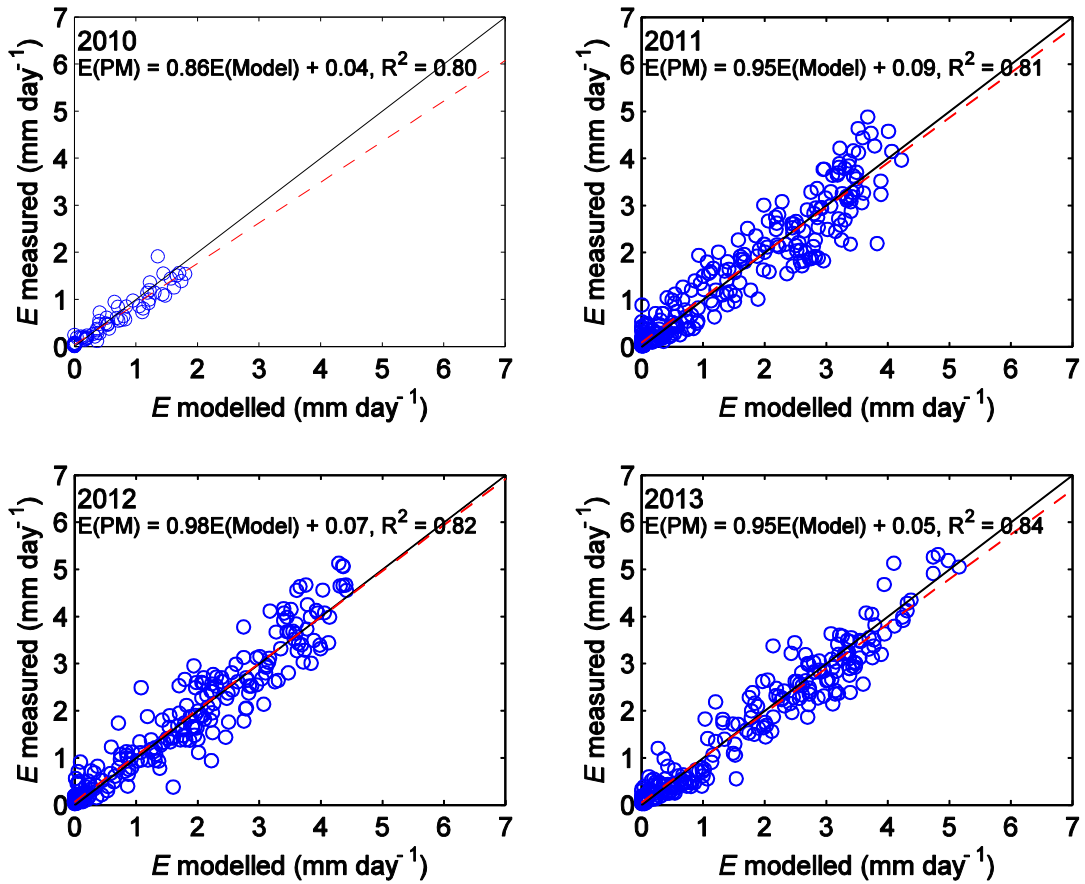


Figure 18: Modelled (model) vs. measured (PM) daily  $E$  for the growing season (May–September) of all years at HP09. The solid line is the 1:1 line and the dashed red line represents the regression equation. Also shown is the linear regression equation (with the coefficient of determination).

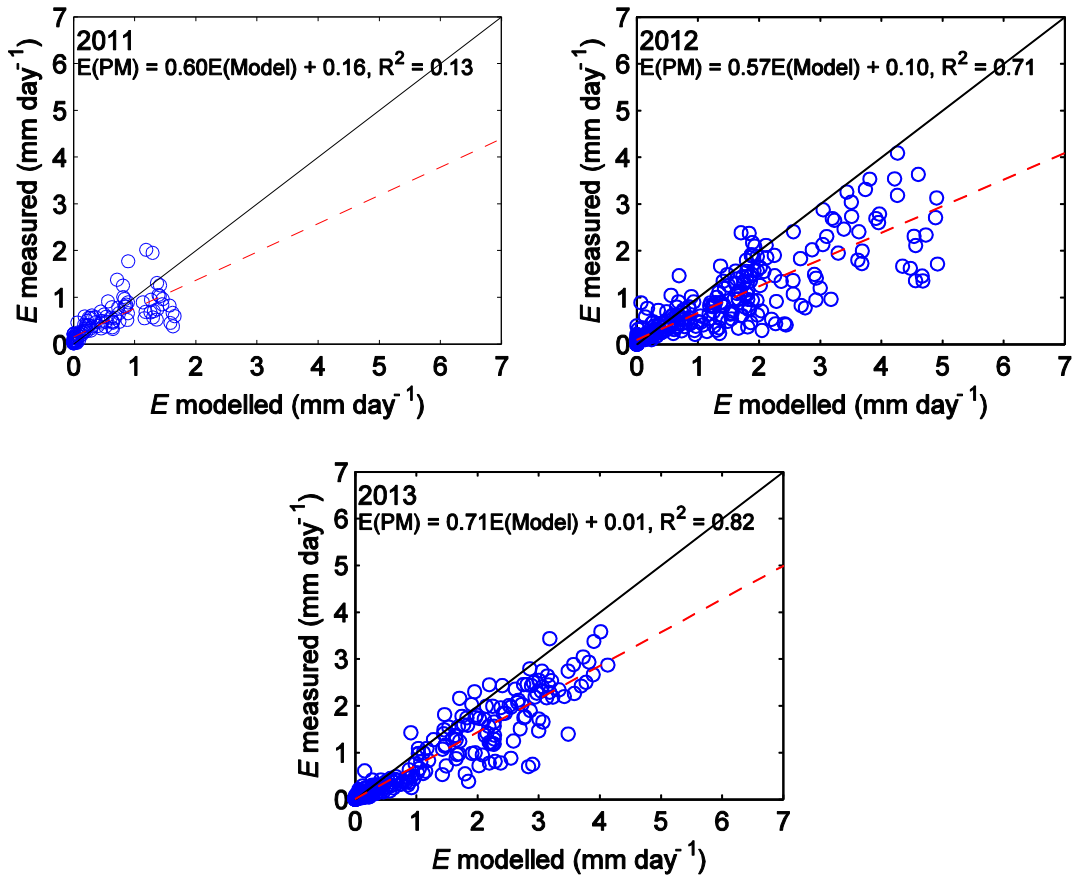


Figure 19: Modelled (model) vs. measured (PM) daily  $E$  for the growing season of all years at HP11. The solid black line is the 1:1 line, and the dashed red line represents the regression equation. Also shown is the linear regression equation (with the coefficient of determination).

The sensitivities of  $E$ ,  $E_c$  and  $E_s$  to changes in  $k_A$ ,  $k_Q$ ,  $Q_{50}$  and  $D_{50}$  are shown in Figure 20. It is clear that  $E$  is insensitive to changes in  $k_A$ , but the partitioning of  $E$  into  $E_c$  and  $E_s$  is highly sensitive to changes in  $k_A$ . Similarly,  $E$  is relatively insensitive to changes in  $k_Q$  but, unlike  $k_A$ ,  $k_Q$  has no effect on the value of  $E_s$  and has a non-linear effect on the value of  $E_c$ .  $Q_{50}$  and  $D_{50}$  also have no effect on the value of  $E_s$  but, when changed,  $Q_{50}$  and  $D_{50}$  have a large impact on the value of  $E_c$  and subsequently  $E$ . This is expected given that  $Q_{50}$  and  $D_{50}$ , along with  $k_Q$ , are restricted to the  $G_c$  model (Eq. (3)) and have no consequence for the value of  $E_s$ .

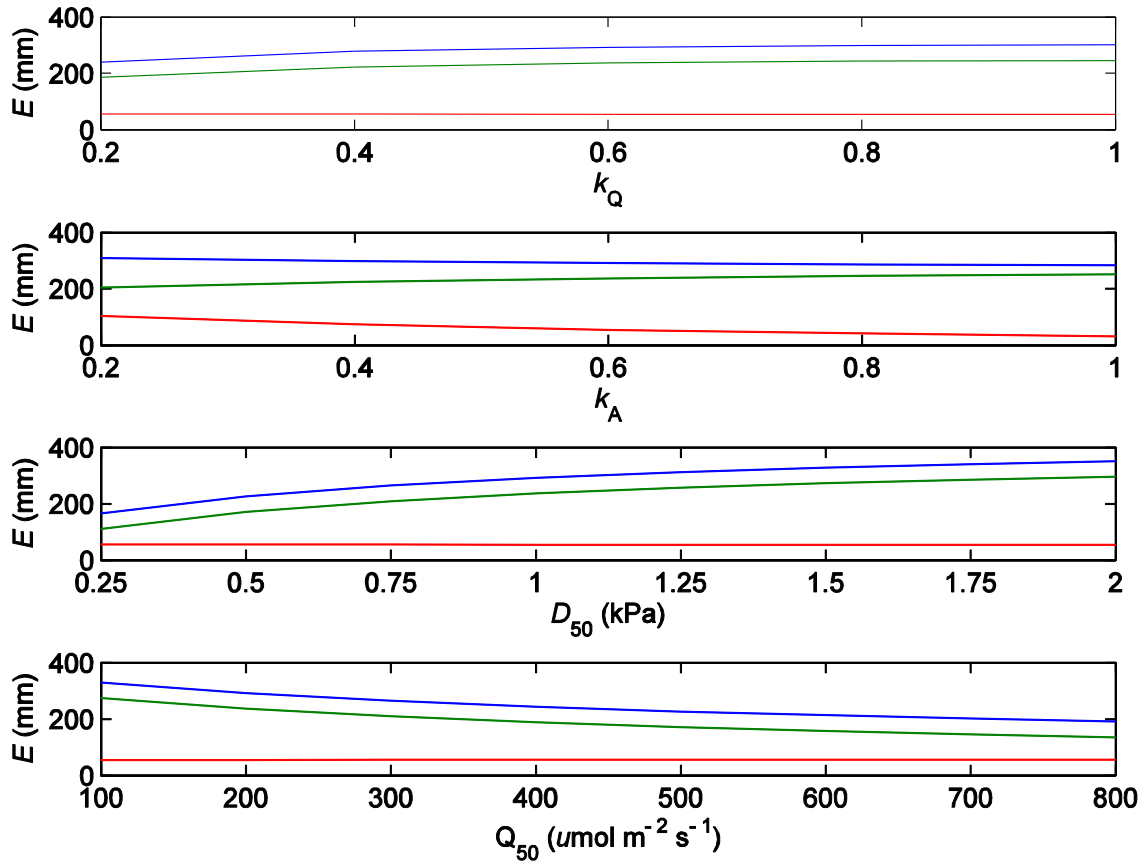


Figure 20: Sensitivity of growing season (May 1 – Sept 30)  $E$  (blue line),  $E_c$  (green line) and  $E_s$  (red line) to model parameters  $k_Q$ ,  $k_A$ ,  $D_{50}$  and  $Q_{50}$  during the 4<sup>th</sup> year of growth at HP09 while maintaining model parameters  $g_{\text{smax}}$ ,  $f$  and LAI constant at values given in Table 1.

## 4.5 Annual water balance and water use efficiency

### 4.5.1 Water balance

Figures 21 and 22 show all components of the annual water balance ( $P = E + \Delta W + D_r$ ) for all years of the study at HP09 and HP11, respectively. During the course of the study,  $P$  and  $E$  at both sites were similar in magnitude and up until the 2<sup>nd</sup> year of growth positive annual drainage from the root zone were calculated at both sites, and even during the 3<sup>rd</sup> year of growth at HP11. At HP09, negative annual drainage (capillary rise) was calculated during the 3<sup>rd</sup> year of growth, after which in the 4<sup>th</sup> year the site received 541 mm of  $P$ , well above the 30-year annual average, and drainage became slightly positive given that  $E$  was 485 mm at the site. During the 5<sup>th</sup> year HP09 received 334 mm of  $P$ , below the 30-year annual average of 364 mm, and remarkably the total annual  $E$  measured at the site using the EC technique far exceed annual  $P$ , equalling 462 mm.

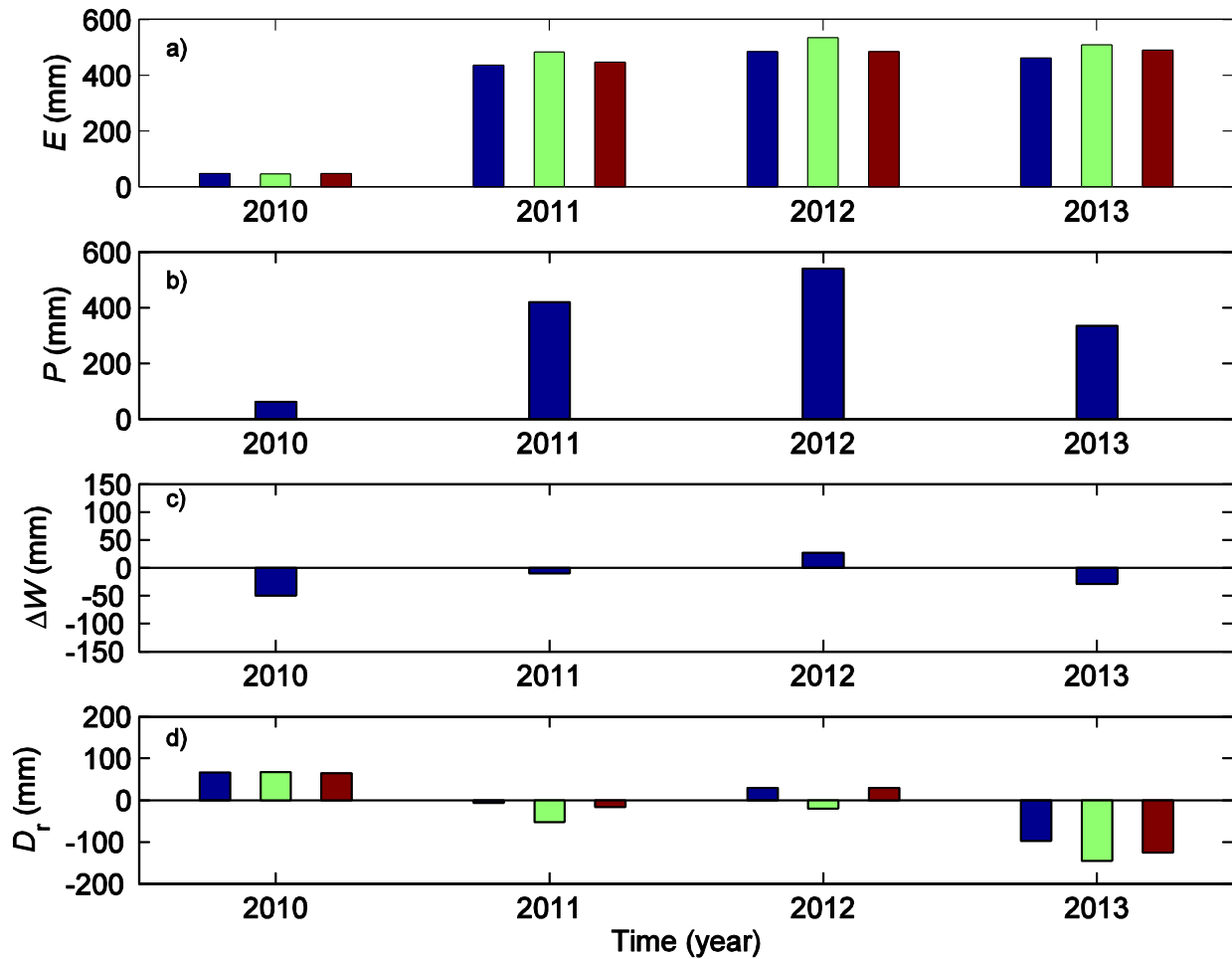


Figure 21: Annual (Jan 1 –Dec 31) water balance at HP09 from the beginning of measurement in May 25, 2010 to Dec 31, 2013. Precipitation ( $P$ ) and change in soil water storage ( $\Delta W$ ), in panel b) and c), respectively, are constant each year for water balance calculations, represented by a single bar in each year. In panel a) the three color bars, blue, green and magenta, represent  $E$  measured (no EBC correction),  $E$  measured (with EBC correction) and modelled  $E$ , respectively, with the same colors representing the drainage calculated using the respective values of  $E$ .

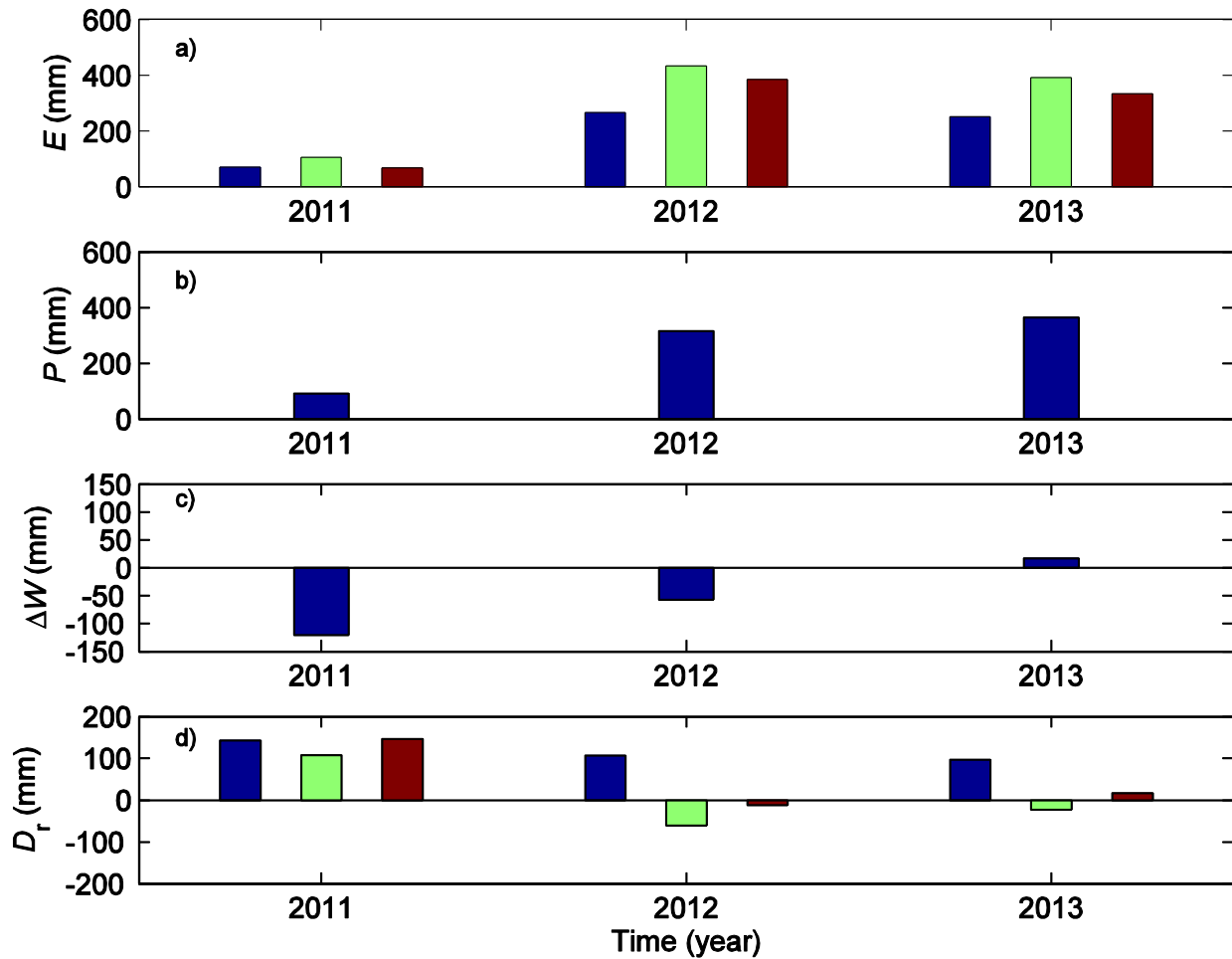


Figure 22: Annual (Jan 1 –Dec 31) water balance at HP11 from the beginning of measurement in June 3, 2011 to Dec 31, 2013. Precipitation ( $P$ ) and change in soil water storage ( $\Delta W$ ), in panel b) and c), respectively, are constant each year for water balance calculations, represented by a single bar in each year. In panel a) the three color bars, blue, green and magenta, represent  $E$  measured (no EBC correction),  $E$  measured (with EBC correction) and modelled  $E$ , respectively, with the same colors representing the drainage calculated using the respective values of  $E$ .

#### 4.5.2 Carbon balance

NEP at both sites remained negative, a source of C, until the end of the 2<sup>nd</sup> year of growth. Annual NEP at HP11 was estimated to be  $-160 \text{ g C m}^{-2} \text{ y}^{-1}$  for the 1<sup>st</sup> year, measured as  $-88 \text{ g C m}^{-2}$  between May 8 and Dec 31, 2011, whereas NEP was not measured at HP09 during the 1<sup>st</sup> year of growth (Figure 23). During the entire 2<sup>nd</sup> year of growth HP09 was a strong source of C with an estimated NEP of  $-140 \text{ g C m}^{-2} \text{ y}^{-1}$ , based on measured NEP of  $-64 \text{ g C m}^{-2}$  between June 1 and Dec, 2010 (Figure 23).

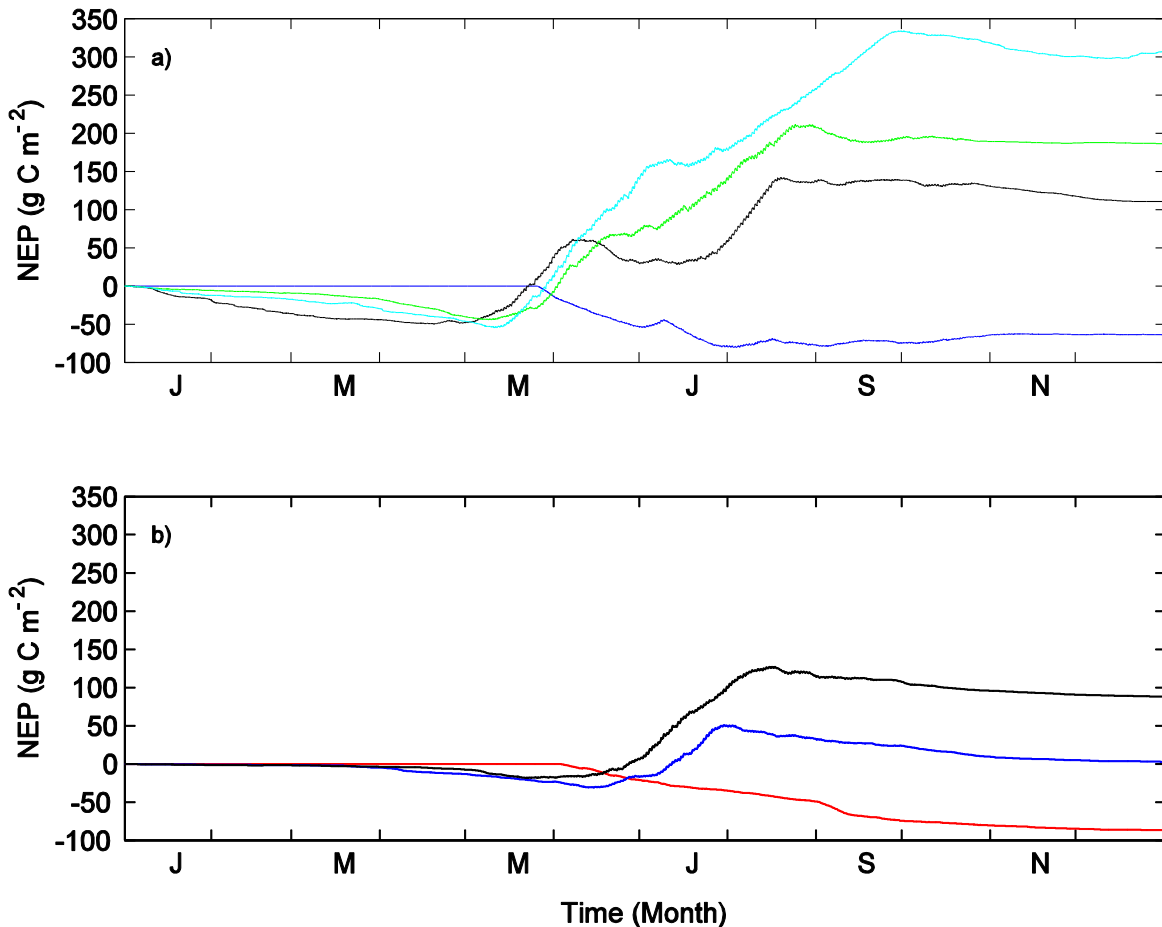


Figure 23: Panels a) and b) show the cumulative net ecosystem productivity (NEP) at HP09 and HP11, respectively, during all years of the study period. The 1<sup>st</sup>, 2<sup>nd</sup>, 3<sup>rd</sup>, 4<sup>th</sup> and 5<sup>th</sup> years of growth after HP establishment are represented by the red, blue, black, green and cyan lines, respectively.

In contrast, HP11 was a small C sink during June and July of the 2<sup>nd</sup> year as LAI increased rapidly and GPP began to exceed  $R_e$ , but slowly became a small C source as GPP declined during September, October, November and December, with annual NEP equalling  $-22 \text{ g C m}^{-2} \text{ y}^{-1}$  (Figure 24 and Table 2). In the 3<sup>rd</sup> year of growth, both plantations became C sinks, when NEP was measured as 110 and  $95 \text{ g C m}^{-2} \text{ y}^{-1}$  at HP09 and HP11, respectively (Figure 24 and Table 2). At HP09 during the 4<sup>th</sup> and 5<sup>th</sup> years of growth, for which there are no matching data from HP11, NEP increased continuously and was measured as 186 and  $307 \text{ g C m}^{-2} \text{ y}^{-1}$ , respectively (Figure 24 and Table 2).

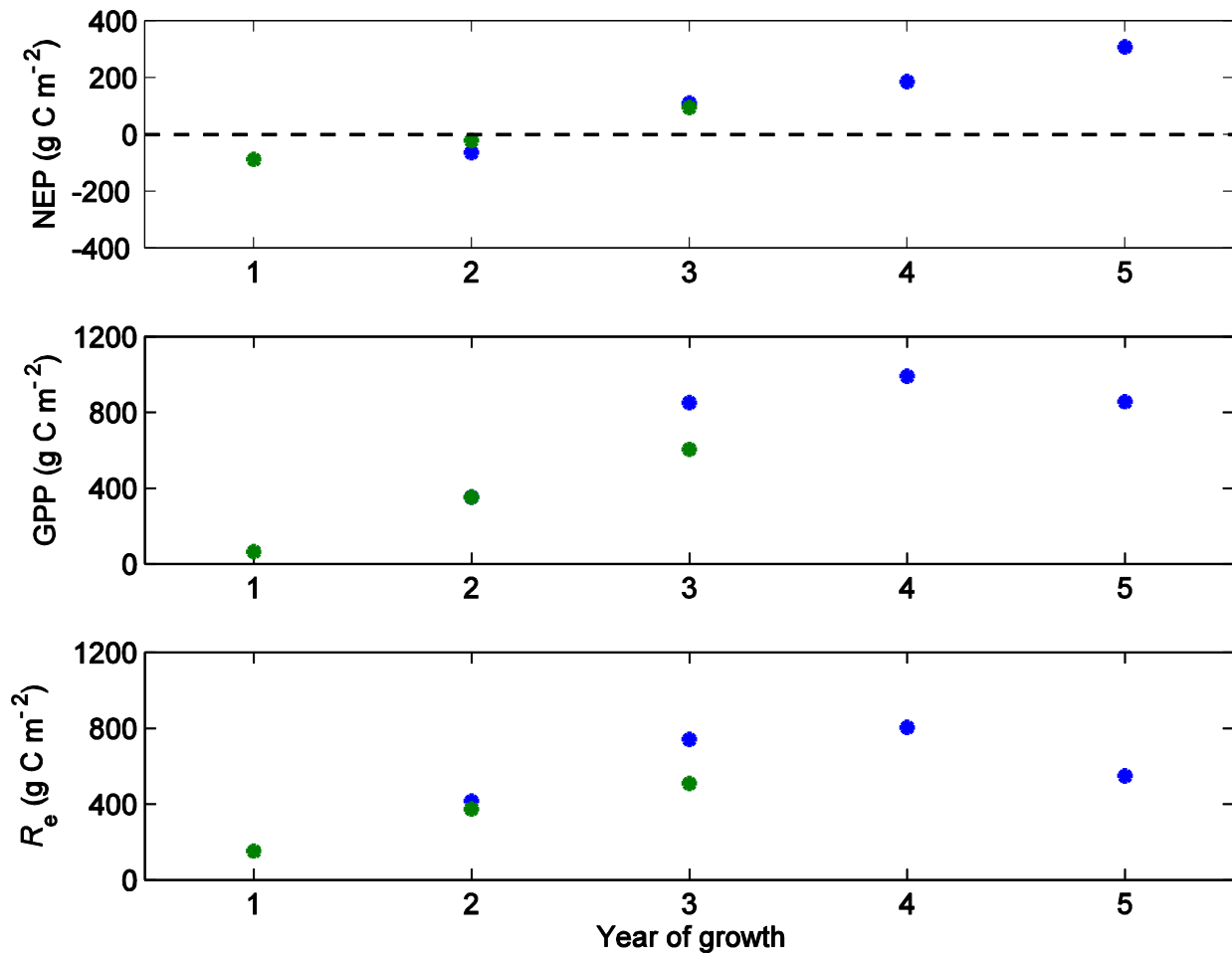


Figure 24: Annual sums of NEP, GEP and  $R_e$  during each year of growth at HP09 (blue asterisks) and HP11 (green asterisks).

### 4.5.3 Water use efficiency

Annual water use efficiency, calculated as  $GPP/E$ , increased every year after plantation establishment at both HP09 and HP11. In the 1<sup>st</sup> year of growth at HP11, for which there are no matching data from HP09, GPP and WUE were low, measured as  $64 \text{ g C m}^{-2} \text{ y}^{-1}$  and  $0.43 \text{ g C kg}^{-1} \text{ H}_2\text{O}$ , respectively (Table 2).

Table 2: Annual NEP, GPP,  $R_e$ ,  $E$  and WUE at both sites for each year of the study period.

Site	Annual values	Year			
		2010	2011	2012	2013
HP09	<b>Year of growth</b>	<b>2<sup>nd</sup></b>	<b>3<sup>rd</sup></b>	<b>4<sup>th</sup></b>	<b>5<sup>th</sup></b>
	NEP ( $\text{g C m}^{-2} \text{ y}^{-1}$ )	-64*	110	186	307
	GPP ( $\text{g C m}^{-2} \text{ y}^{-1}$ )	352*	851	990	856
	$R_e$ ( $\text{g C m}^{-2} \text{ y}^{-1}$ )	416*	741	804	549
	$E$ (mm)	276*	437	485	462
	WUE ( $\text{g C kg}^{-1} \text{ H}_2\text{O}$ )	1.31*	1.95	2.04	1.86
HP11	<b>Year of growth</b>	-	<b>1<sup>st</sup></b>	<b>2<sup>nd</sup></b>	<b>3<sup>rd</sup></b>
	NEP ( $\text{g C m}^{-2} \text{ y}^{-1}$ )	-	-88*	-22	95
	GPP ( $\text{g C m}^{-2} \text{ y}^{-1}$ )	-	64*	351	604
	$R_e$ ( $\text{g C m}^{-2} \text{ y}^{-1}$ )	-	152*	373	509
	$E$ (mm)	-	149*	266	242
	WUE ( $\text{g C kg}^{-1} \text{ H}_2\text{O}$ )	-	0.43*	1.32	2.5

\* Indicates values were measured or calculated from the beginning of measurement, rather than on an annual basis, which was June 1, 2010 and May 8, 2011 at HP09 and HP11, respectively, until the end of the calendar year (Dec 31).

In the 2<sup>nd</sup> year GPP and WUE increased dramatically to  $351 \text{ g C m}^{-2} \text{ y}^{-1}$  and  $1.32 \text{ g C kg}^{-1} \text{ H}_2\text{O}$  at HP11 and was strikingly similar at HP09, equalling  $352 \text{ g C m}^{-2} \text{ y}^{-1}$  and  $1.31 \text{ g C kg}^{-1} \text{ H}_2\text{O}$ . In the 3<sup>rd</sup> growing season, the sites began to differ substantially regarding GPP and WUE (Table 2). At HP09, GPP was higher in the 3<sup>rd</sup> year of growth compared to HP11 with annual values equal to  $851$  and  $604 \text{ g C m}^{-2} \text{ y}^{-1}$ , respectively, but the WUE was lower at HP09 compared to HP11, equalling  $1.95$  and  $2.5 \text{ g C kg}^{-1} \text{ H}_2\text{O}$ , respectively (Table 2). At HP09, in the 4<sup>th</sup> growing season GPP and WUE increased to values of  $990 \text{ g C m}^{-2} \text{ y}^{-1}$  and  $2.04 \text{ g C kg}^{-1} \text{ H}_2\text{O}$ , but unexpectedly GPP decreased in the 5<sup>th</sup> year of growth to  $856 \text{ g C m}^{-2} \text{ y}^{-1}$  and a decrease in WUE was observed

at  $1.86 \text{ g C kg}^{-1} \text{ H}_2\text{O}$  (Table 2). The observed decline in GPP during the 5<sup>th</sup> year at HP09 is likely the result of a fungal infection (*Cytospora* sp.), which was visually identifiable during all of 2013 and killed 100% of the terminal stems on the HP individuals in the plantation, reducing LAI and consequently GPP and *E*.

## 5 Discussion

### 5.1 Surface and canopy conductance model

Good agreement was found during the first 5 years after HP afforestation between  $E$  measured using EC and  $E$  calculated using the  $G_s$  model, which treats latent heat flux from the plant canopy ( $\lambda E_c$ ) and soil surface ( $\lambda E_s$ ) as two separate evaporation streams using the PM and modified equilibrium evaporation equations, respectively (Kelliher et al. 1995; Leuning et al. 2008). A two-source model seems appropriate in most circumstances but particularly in this study by virtue of the highly dynamic nature of newly established afforestation systems, that are often characterized by high proportions of bare ground and variability in LAI, both seasonally and annually. With the same  $G_s$  model, modified to include an optimized static soil moisture function ( $f$ ), Leuning et al. (2008) found good agreement between measured and modelled  $E$  at 15 globally distributed flux stations, encompassing coniferous, deciduous, mixedwood, grassland, crop and wetland sites, demonstrating the robust nature of the PM equation. Given that  $G_s$  is considered to apply to two surfaces (i.e., trees and soil) rather than one, “bulk” surface, the challenge lies in parameterizing a  $G_c$  sub-model and a soil evaporation sub-model. Rather than modelling  $G_c$  using a Jarvis-Stewart least squares approach in which empirical relationships are determined between  $G_c$  and chosen micrometeorological/soil variables (Stewart 1988; Stewart and Gay 1989) or a more process-based approach which incorporates carbon (C) assimilation into parameterizing  $G_c$  like the Ball-Woodrow-Berry model (Ball et al. 1987; Blanken and Black 2004), I used a maximum stomatal conductance ( $g_{smax}$ ) approach derived to describe the cumulative leaf level physiological response of individual stomata to varying photosynthetically active radiation ( $Q$ ) as a function of cumulative leaf area index through the canopy (Dolman et al. 1991; Saugier and Katerji 1991). This approach is attractive for

modelling  $G_c$  because it accounts for changing stomatal conductance depending on depth in the canopy. It takes advantage of  $g_s$  measurements that were taken at various positions within the canopy (low, mid and high), using a porometer, which have shown stomata high in the canopy may achieve  $g_s$  closer in value to  $g_{smax}$ , a physiological maximum, whereas stomata lower and deeper in the canopy envelope receiving less  $Q$  will not (Ceulemans et al. 1988; Dolman et al. 1991; Meinzer et al. 1997; Kim et al. 2008). Given that a hyperbolic dependence of  $G_s$  on  $D$  was observed in my data and is well documented across various vegetated surfaces in the literature (Stewart 1988; Wu et al. 2000; Humphrey et al. 2003; Blanken and Black 2004) a hyperbolic expression was used in the  $G_c$  model, in a multiplicative manner, following Leuning (1995). The incorporation of a  $D$  expression which assumes the same  $D$  throughout the canopy represents a limitation of the model, as it fails to account for changes in  $D$  associated with canopy closure and a well-developed understory (Dolman et al. 1991; Blanken and Black 2004). Another consideration for the  $G_s$  model used in this study is the need to properly differentiate and apply separate treatments of  $G_a$  for the “bulk” surface and for the plant canopy (say,  $G_{ac}$ ), as they are likely to be different. Black and Kelliher (1989) were able to accurately describe the boundary layer conductance of individual leaves and subsequently the plant canopy  $G_{ac}$  of a Douglas fir understory, and such an approach may improve model performance particularly in highly coupled canopies. Nevertheless, no such treatment was applied in this study or others that use the same  $G_s$  model with the argument that  $E$  is relatively insensitive to changes in  $G_a$  (Kelliher et al. 1995; Leuning et al. 2008; Zhang et al. 2008). Dependencies of  $G_s$  on soil water near the soil surface were incorporated into the  $E_s$  term of the  $G_s$  model, using a relative water content function, yet no such dependency was applied to the  $E_c$  term and may become increasingly relevant regarding transpiration limitation in drought prone regions (e.g., Harris et al. 2004).

Despite the aforementioned shortcomings of the  $G_s$  model, which could be verified without serious alteration of the  $G_s$  model, the model was remarkably robust, following the complexities of PM calculated  $G_s$  over fine temporal scales (half-hourly and daily), attributable to the physiological based  $G_c$  sub model. Another important attribute of the  $G_s$  model is the fact that EC measurements were not needed to parameterize the model, which frees the  $G_s$  model from empirically drawn relationships. Overall, The  $G_s$  model was highly sensitive to changes in LAI and  $g_{\text{max}}$  but highly insensitive to changes  $Q_{50}$ ,  $D_{50}$ ,  $k_Q$ ,  $k_A$ .

## 5.2 Energy balance

Lack of energy balance closure, the failure of the sum of the EC measured convective fluxes ( $\lambda E + H$ ) to equal the available energy flux at the surface ( $R_n - G - \Delta S$ ), is prevalent and well documented at flux stations around the globe (Blanken et al. 1997; Wilson and Baldocchi 2000; Wilson et al. 2002; Baldocchi 2003; Foken et al. 2006; Leuning et al. 2008; Kidston et al. 2010; Barr et al. 2012). Lack of closure may occur for several reasons: 1) errors and/or lack of representativeness in measurement of: i)  $R_n$ , ii)  $G$ , iii) convective fluxes  $H$  and  $\lambda E$ , and iv) energy storage in the biomass, soil and air between the soil heat flux plates and height of measurement; 2) Horizontal or vertical advection of energy resulting from failure to satisfy the one-dimensional transport, assumed when performing eddy-covariance flux measurements; 3) low and high frequency spectral losses resulting from short averaging periods and inadequately low sampling frequency, respectively.

Over a heterogeneous corn (*Zea mays*) field, Foken et al. (2006) found low frequency spectral losses resulted in underestimation of  $\lambda E$ , rather than high frequency spectral losses. Similarly, Kidston et al. (2010) found low frequency spectral losses may partly explain underestimation of  $\lambda E$  over a mature jack pine (*Pinus banksiana*) stand and found high

frequency spectral losses associated with attenuation of the water vapour mixing ratio within the air sampling tube accounted for underestimation of  $\lambda E$  over a clear-cut jack pine stand and errors increased with decreasing  $D$ . Similarly in my study, when energy balance correction was applied to  $\lambda E$  and  $H$  fluxes at both flux stations, maintaining the measured Bowen ratio i.e.  $H/\lambda E$  (Barr et al. 2012), the magnitude of the correction relative to the uncorrected convective fluxes increased as  $D$  decreased.

Horizontal and/or vertical advection (Novick et al. 2014) of energy, out of or into the control volume, between the height of convective flux measurement and the soil surface can result in underestimation of turbulent fluxes, particularly during stable atmospheric boundary layer conditions at nighttime. At global FLUXNET sites Wilson et al. (2002) found EBC improved as  $u^*$  increased, indicating EBC is directly correlated with turbulent mixing. To overcome underestimation bias associated with stable atmospheric nighttime conditions, a friction velocity ( $u^*$ ) threshold was empirically determined, which delineated weak and strong turbulent conditions below and above the  $u^*$  threshold, respectively, after which all fluxes below the threshold were excluded from further analysis. At HP09, additional scrutiny of nighttime fluxes stemmed from the expansion of the source flux footprint which, given insufficient fetch at HP09, expanded beyond the spatial limits of the HP plantation. In contrast, both sites had adequate daytime fetch during all years of the study period, based on flux footprint analysis, which gave me confidence regarding the representativeness of daytime  $H$ ,  $F_c$ ,  $\lambda E$  flux measurements.

Lack of representativeness of  $G$  and  $R_n$  were thought to be large sources of error throughout the study, particularly at HP11. Considering that both sites were cultivated mechanically, soil heat flux plates were positioned in a designated area to prevent sensor damage

and were cultivated separately, by hand. Mechanical cultivation of the plantation always preceded the hand cultivation causing  $G$  to be underestimated, because the understory vegetation: 1) had a dissimilar albedo to that of the soil surface; and 2) absorbed radiation that would otherwise reach the soil surface and soil heat flux plates. The representativeness errors associated with  $R_n$  were in part a result of instrument positioning and orientation in relation to the flux tower, rows of HP trees and understory vegetation, particularly at HP11. During the 1<sup>st</sup> and 2<sup>nd</sup> growing seasons the trees grew rapidly closer to the initial  $R_n$  measurement height of 2 m, at both sites, which reduced the view factor and representativeness of the  $R_n$  measurement. Given that, in the 3<sup>rd</sup> growing season, the net radiometers at both sites were raised to a height of 4 and 3 m at HP09 and HP11, respectively, and no increase in energy balance closure fraction was observed,  $R_n$  representativeness errors related to net radiometer height were not likely the cause of the systematically poor energy balance closure fraction observed at HP11. It is hypothesized overestimation of  $R_n$  and  $A$  throughout the study period resulted from the fact that the net radiometer was positioned too closely to the flux tower at HP11, causing the flux tower to influence  $R_n$  measurements, and that the net radiometer was located above and oriented parallel to an unplanted row for the duration of the study. This is believed to be the largest source of error that caused HP11 to achieve such poor energy balance closure year after year, akin to Kidston et al. (2010) who found, despite errors associated with frequency covariance losses, flux tower radiative forcing was the largest source of error regarding  $R_n$  measurement that caused poor EBC. For this study no measure of energy storage within biomass was made, and undoubtedly represents a fraction of the energy balance closure residual, but does not explain the extremely poor closure at HP11 given HP09 achieved good closure and was subject to the same energy storage measurement errors. Scaling up from EC measurements, Barr et al. (2012) found that

correcting  $H$  and  $\lambda E$ , i.e. maintaining the Bowen ratio (Blanken et al. 1997), to close the energy balance led to water balance closure in the White Gull Creek watershed. Ding et al. (2010) also found correcting  $H$  and  $\lambda E$  to close the energy balance improved agreement between EC measured and lysimeter measured  $E$ , but given the lack of EBC resulted from a number of errors in this study, which are not completely understood, EBC corrected fluxes were not used for annual water and carbon balance calculations, only for qualitative analysis. Regarding modelling efforts, it is important to note that  $A$ , calculated from  $R_n$  and  $G$  measurements, was an input to the  $G_s$  model and caused errors in  $R_n$  and  $G$  to propagate through the  $G_s$  model which was avoided by other authors using  $A$  calculated from the sum  $H$  and  $\lambda E$  (Leuning et al. 2008). Given that the utility of the  $G_s$  model lay in its ability to predict  $\lambda E$ , from  $R_n$  and  $G$  measurements, it seems more appropriate to use  $A$  calculated from  $R_n$  and  $G$  measurements rather than  $A$  calculated from the sum of EC measured  $H$  and  $\lambda E$ .

### **5.3 Water balance**

The two HP plantations in our study, HP09 and HP11, differed notably regarding the annual water balance, despite both being planted on class 1 (high productivity) soil and experiencing similar climate. Water balance analysis showed that annual  $E$  and  $P$  at HP09 were similar in magnitude and as a result drainage alternated between positive and negative values during the first 5 years of growth. At HP11  $P$  exceeded  $E$  during the first 3 years of the study resulting in positive annual drainage, similar to Cai et al. (2011) who found positive annual drainage during the first 3 years of growth on a far less productive, class 3 (marginally productive) soil. A plausible explanation for suppressed  $E$  at HP11 is the drought conditions that occurred immediately after plantation establishment at the site in June 2011, which killed ~20% of the original HP stock, and may have caused xylem cavitation and hydraulic failure in

surviving individuals. In Colorado, Anderegg et al. (2012) found drought-affected trembling aspen were less capable of withstanding future droughts due to both abrupt and gradual xylem fatigue which reduced aspen hydraulic conductivity and productivity. If, early in the lifecycle, HP xylem were physically damaged during drought conditions at HP11, it may explain the early senescence observed, correlated with dry conditions in July and August (Figure 2), and systematically low  $G_s$ , GPP and LAI each year at HP11 (Table 2 and Figure 13). In comparison  $G_s$ , GPP and LAI were high at HP09 which received precipitation above the 30-year annual average and experienced no drought like conditions during the study. As a result,  $E$  was large each year and annual drainage became slightly negative (capillary rise) in only the 3<sup>rd</sup> growing season and became largely negative in the 5<sup>th</sup> growing season, similar in magnitude to negative drainage measured in semi-arid Inner Mongolia but far exceeding negative drainage calculated in the 5<sup>th</sup> growing season on marginal land in Alberta, Canada (Wilske et al. 2009; Cai et al. 2011). EC measurements between 1994 and 2003 above a mature trembling aspen in the southern boreal forest of Saskatchewan showed annual  $P$  generally exceeded annual  $E$ , but during a drought period between 2001 and 2003 in Canada's Western Prairie Provinces,  $E$  exceeded  $P$  resulting in water table decline and negative drainage equal to ~350 mm during the 3 year drought period (Barr et al. 2007). Results such as these, and those found in this study reveal the delicate balance between  $P$  and  $E$  in the aspen parkland and the boreal forest of Canada. Trembling aspen dieback has been well documented in North America (Hogg et al. 2005; Hogg et al. 2008; Michaelian et al. 2011; Anderegg et al. 2012). Reduced drainage has been correlated with large-scale afforestation (Rijtema and de Vries 1994; Perry et al. 2001), and fresh water sources (glaciers) are diminishing and major tributaries (rivers) are drying (Comeau et al. 2009; Kienzle et al. 2012; MacDonald et al. 2013). Therefore, water balance studies and evapotranspiration

modelling efforts are invaluable and necessary to evaluate possible drawbacks regarding large-scale HP afforestation effects on groundwater, as well as the possible benefits regarding biomass and soil C sequestration.

#### 5.4 Carbon balance

Both sites in this study were C sources, i.e.,  $NEP < 0$ , until the end of the 2<sup>nd</sup> year of growth, as  $R_e$  exceeded GPP. In Belgium, Zona et al. (2013) found HP planted on a sandy loam soil receiving ~700 mm of annual  $P$  quickly shifted to a C sink in the 2<sup>nd</sup> year of growth, whereas Cai et al. (2011) found HP planted on silty-clay Luvisolic soil in Alberta, Canada receiving ~350 mm of annual  $P$  remained a C source until the 5<sup>th</sup> year of growth, a drought year, in which the plantation sequestered a meager  $17 \text{ g C m}^{-2} \text{ y}^{-1}$ . In this study NEP in the 3<sup>rd</sup> year of growth was strikingly similar between sites but the magnitudes of  $R_e$  and GPP were disparate. Drought suppressed GPP at HP11 was correlated with lower  $R_e$  values indicating GPP was directly correlated with autotrophic respiration ( $R_a$ ; Barr et al. 2007), which becomes increasingly dominant over heterotrophic respiration ( $R_e$ ) as the HP plantations aged (Arevalo et al. 2010; Arevalo et al. 2011). Both  $R_e$  and GPP increased each year of the study at both sites except in the 5<sup>th</sup> year of growth at HP09, when a *Cytospora* sp. fungal infection was observed and suppressed both  $R_e$  and GPP, but GPP to a lesser extent than  $R_e$  likely due to the uninfected understory which partially compensated for decline in HP GPP. Although the HP plantations in this study became C sinks relatively quickly it is important to consider that no measure of C flux was made during or preceding site preparation, which is an admitted shortcoming of studies akin to ours (Zona et al. 2013; Verlinden et al. 2013). Another short-coming of this C balance analysis lies in the lack of data and knowledge regarding soil C sequestration at the two sites, which is considered a long-term storage medium in relation to biomass. Sierra et al. (2013) found

agricultural land converted from corn to HP sequestered an average  $1.6 \text{ Mg C ha}^{-1} \text{ y}^{-1}$  in the soil during a 30 year rotation, particularly in the top 20 cm of the soil profile, and studies done in Alberta show conversion of agricultural land to HP causes soil C to decline initially, after which soil C begins to accumulate with plantation age (Sierra et al. 2013; Arevalo et al. 2010; Arevalo et al. 2011). Nevertheless the opposite has been reported in some studies. For example, Vesterdal et al. (2002) found that soil C declined on the top 25 cm of the soil profile and a synthesis of soil C sequestration after afforestation performed by Nave et al. (2013) found that gains on agricultural lands were insignificant, but that afforestation on reclamation sites significantly increased soil C, particularly near the soil surface. Studies like this one are important to quantify the C balance of whole ecosystems, but it will be important for future efforts to properly quantify the specific C sinks within ecosystems to assess the long-term soil C sequestration potential of HP plantations and afforested ecosystems in general.

## **5.5 Water use efficiency**

WUE increased every year of the study at both sites. In the 2<sup>nd</sup> year of growth, for which we have measurements from both sites, WUE at the two sites was similar but in the 3<sup>rd</sup> year of growth WUE at HP11 was higher than at HP09, despite having a much lower GPP. This is likely due to the fact that stomatal conductance dynamics affect exchange of  $\text{CO}_2$  and  $\text{H}_2\text{O}$  vapour at the leaf scale equally. Over a 12 year old HP plantation in Italy, Migliavacca et al. (2009) found growing season (April to September) WUE was equal to  $4.26 \text{ g C kg}^{-1} \text{ H}_2\text{O}$  in 2002 (12<sup>th</sup> year of growth) and declined to  $3.07 \text{ g C kg}^{-1} \text{ H}_2\text{O}$  during a drought in the following year (2003). In contrast, Brümmer et al. (2012) found WUE of a 70-year-old trembling aspen stand showed little change during the 2001-2003 drought mentioned above, given  $E$  and  $GPP$  declined proportionally. This may indicate relatively young HP are more susceptible to changes in soil

moisture potential than mature native aspen stands, causing their intrinsic water use efficiency ( $WUE_i = WUE \times D$ ) (Beer et al. 2009) to decline during drought events. Despite WUE increasing every year after HP establishment it remained relatively unchanged from the 4<sup>th</sup> to 5<sup>th</sup> year of growth at HP09 despite the fact the site experienced no drought conditions, which wasn't expected, and may be attributable to a reduction in  $WUE_i$  as a result of the previously mentioned *Cytospora sp.* infection. It will be interesting to see how and investigate why WUE and  $WUE_i$  change as HP age as it will enable us to better understand HP response to disturbance and drought, particularly in a highly dynamic grassland-forest transition zone such as the aspen parkland.

## 6 Conclusions

I parameterized canopy conductance ( $G_c$ ) and soil evaporation ( $E_s$ ) sub-models which were subsequently input to a surface conductance ( $G_s$ ) model that showed excellent agreement across annual, daily and hourly temporal scales with  $G_s$  calculated using the inverted Penman-Monteith (PM) equation and eddy-covariance (EC) measured evapotranspiration ( $E$ ) above two HP plantations.  $G_s$  calculated from EC flux data showed strong dependence on photosynthetically active radiation ( $Q$ ) and vapor pressure deficit ( $D$ ), but there was a less clear relationship with soil water. A soil water supply function ( $f$ ) set equal to the relative soil water content was incorporated in the  $E_s$  sub-model which greatly improved  $E$  predictions during leafless periods, but soil moisture effects were not incorporated in the  $G_c$  sub-model but may become increasingly relevant during severe drought conditions as the plantations grow older. The robust nature of the  $G_c$  sub-model allowed the larger  $G_s$  model to exemplify the strong diurnal stomatal closure response and seasonal changes seen in  $G_s$  calculated from EC flux data, without drawing empirical relationships between EC derived  $G_s$  and measured variables. A definite strength of the two-source model was the fact it allowed separate parameterizations of  $E_s$  and  $E_c$ , enabling accurate predictions of  $E$  in an intensively managed and highly dynamic deciduous ecosystem, accurately predicting  $E_s$  during the leafless periods of the year and  $E_c$  during spring leaf-out, full-leaf periods and fall senescence. Separate from  $G_s$  modelling efforts I was able to show:

- Two HP plantations grown on high productivity (Class 1) Chernozemic soil shifted from being C sources to C sinks in the 3<sup>rd</sup> growing season.
- Annual  $E$  increased with plantation age in proportion to increases in  $E_c$  and GPP, and could exceed  $P$  after only three years of growth.

- WUE increased with plantation age but was independent of productivity given stomatal controls affect CO<sub>2</sub> and H<sub>2</sub>O gas exchange at the leaf level equally.

## References

- Allen, S. J., Hall, R. L., and Rosier, P. T. W. (1999). Transpiration by two poplar varieties grown as coppice for biomass production. *Tree Physiology*, *19*: 493–501.
- Anderegg, W. R. L., Berry, J. A., Smith, D. D., Sperry, J. S., Anderegg, L. D. L., and Field, C. B. (2012). The roles of hydraulic and carbon stress in a widespread climate-induced forest die-off. *Proceedings of the National Academy of Sciences of the United States of America*, *109*: 233–237.
- Anderson, J. A., Armstrong, G. W., Luckert, M. K., and Adamowicz, W. L. (2012). Optimal zoning of forested land considering the contribution of exotic plantations. *Mathematical and Computational Forestry and Natural-Resources Sciences*, *4*: 92–104.
- Arevalo, C. B. M., Bhatti, J. S., Chang, S. X., Jassal, R. S., and Sidders, D. (2010). Soil respiration in four different land use systems in north central Alberta, Canada. *Journal of Geophysical Research*, *115*: 1-12.
- Arevalo, C. B. M., Bhatti, J. S., Chang, S. X., and Sidders, D. (2011). Land use change effects on ecosystem carbon balance: From agricultural to hybrid poplar plantation. *Agriculture, Ecosystems & Environment*, *141*: 342–349.
- Aubinet, M., Grelle, A., Ibrom, A., Rannik, U., Moncrieff, J., Foken, T., Kowalski, A.S., Martin, P.H., Berbigier, P., Bernhofer, CH., Clement, R., Elbers, J., Granier, A., Grunwald, T., Morgenstern, K., Pilegaard, K., Rebmann, C., Snuders, W., Valentini, R. and Vesala, T. (2000). Estimates of the Annual Net Carbon and Water Exchange of Forests: The EUROFLUX Methodology. *Advances In Ecological Research*, *30*: 113–175.
- Baldocchi, D. D. (2003). Assessing the eddy covariance technique for evaluating carbon dioxide exchange rates of ecosystems: past, present and future. *Global Change Biology*, *9*: 479–492.
- Ball, J. T., Woodrow, I. E., and Berry J. A. (1987). A model predicting stomatal conductance and its contribution to the control of photosynthesis under different environmental conditions. *In: Progress in Photosynthesis Research*, Biggins J (ed.). Martinus Nijhoff Publishers: Dordrecht; 221–224.
- Barr, A. G., van der Kamp, G., Black, T. A., McCaughey, J. H., and Nescic, Z. (2012). Energy balance closure at the BERMS flux towers in relation to the water balance of the White Gull Creek watershed 1999–2009. *Agricultural and Forest Meteorology*, *153*: 3–13.
- Barr, A. G., Black, T. A., Hogg, E. H., Griffis, T. J., Morgenstern, K., Kljun, N., and Nescic, Z. (2007). Climatic controls on the carbon and water balances of a boreal aspen forest, 1994–2003. *Global Change Biology*, *13*: 561–576.

- Barr, A. G., Black, T. A., Hogg, E. H., Kljun, N., Morgenstern, K., and Nesic, Z. (2004). Inter-annual variability in the leaf area index of a boreal aspen-hazelnut forest in relation to net ecosystem production. *Agricultural and Forest Meteorology*, 126: 237–255.
- Beer, C., Ciais, P., Reichstein, M., Baldocchi, D., Law, B. E., Papale, D., Sousanna, J. F., Ammann, C., Buchmann, N., Frank, D., Gianelle, D., Janssens, I. A., Knohl, A., Köstner, B., Moors, E., Roupsard, O., Verbeeck, H., Vesala, T., Williams, C. A., and Wohlfahrt, G. (2009). Temporal and among-site variability of inherent water use efficiency at the ecosystem level. *Global Biogeochemical Cycles*, 23: 1–13.
- Black, T. A., den Hartog, G., Neumann, H. H., Blanken, P. D., Yang, P. C., Russell, C., Nesic, Z., Lee, X., Chen, S. G., Staebler, R., and Novak, M. D. (1996). Annual cycles of water vapour and carbon dioxide fluxes in and above a boreal aspen forest. *Global Change Biology*, 2: 219–229.
- Black, T. A., Kelliher, F. M., Wallace, J. S., Stewart, J. B., Monteith, J. L., and Jarvis, P. G. (1989). Processes controlling understorey evapotranspiration [and discussion]. *Philosophical Transactions of the Royal Society B: Biological Sciences*, 324: 207–231.
- Blanken, P. D., and Black, T. A. (2004). The canopy conductance of a boreal aspen forest, Prince Albert National Park, Canada. *Hydrological Processes*, 18: 1561–1578.
- Blanken, P. D., Black, T. A., Yang, P. C., Neumann, H. H., Nesic, Z., Staebler, R., den Hartog, G., Novak, M. D., and Lee, X. (1997). Energy balance and canopy conductance of a boreal aspen forest: partitioning overstory and understory components. *Journal of Geophysical Research*, 102: 28915–28927.
- Boothroyd-Roberts, K., Gagnon, D., and Truax, B. (2013). Hybrid poplar plantations are suitable habitat for reintroduced forest herbs with conservation status. *SpringerPlus*, 2: 507.
- Brümmer, C., Black, T. A., Jassal, R. S., Grant, N. J., Spittlehouse, D. L., Chen, B., Nesic, Z., Amiro, B. D., Arain, M. A., Barr, A. G., Bourque, C. P. A., Coursolle, C., Dunn, A. L., Flanagan, L. B., Humphreys, E. R., Lafleur, P. M., Margolis, H. A., McCaughey, J. H., and Wofsy, S. C. (2012). How climate and vegetation type influence evapotranspiration and water use efficiency in Canadian forest, peatland and grassland ecosystems. *Agricultural and Forest Meteorology*, 153: 14–30.
- Brye, K. R., Norman, J. M., Bundy, L. G., and Gower, S. T. (2000). Water-budget evaluation of prairie and maize ecosystems. *Soil Science Society of America Journal*, 64: 715–724.
- Cai, T., Price, D. T., Orchansky, A. L., and Thomas, B. R. (2011). Carbon, water, and energy exchanges of a hybrid poplar plantation during the first five years following planting. *Ecosystems*, 14: 658–671.
- Campbell, G. S., and Norman, J. M. (1998). *An introduction to environmental physics*. 2<sup>nd</sup> edition. Springer, New York.

- Ceulemans, R., Impens, I., and Imler, R. (1988). Stomatal conductance and stomatal behavior in *Populus* clones and hybrids. *Canadian Journal of Botany*, 66: 1404–1414.
- Comeau, L. E. L., Pietroniro, A., and Demuth, M. N. (2009). Glacier contribution to the North and South Saskatchewan Rivers. *Hydrological Processes*, 23: 2640–2653.
- Denmead, O. T., and McIlroy, I. C. (1970). Measurements of non-potential evaporation from wheat. *Agricultural Meteorology*, 7: 285–302.
- Ding, R., Kang, S., Li, F., Zhang, Y., Tong, L., and Sun, Q. (2010). Evaluating eddy covariance method by large-scale weighing lysimeter in a maize field of northwest China. *Agricultural Water Management*, 98: 87–95.
- Dolman, A. J., Maximov, T. C., Moors, E. J., Maximov, A. P., Elbers, J. A., Kononov, A. V., Waterloo, M. J., and van der Molen, M. K. (2004). Net ecosystem exchange of carbon dioxide and water of far eastern Siberian Larch (*Larix dahurica*) on permafrost. *Biogeosciences Discussions*, 1: 275–309.
- Dolman, A. J., Gash, J. H. C., Roberts, J., and Shuttleworth, W. J. (1991). Stomatal and surface conductance of tropical rainforest. *Agricultural and Forest Meteorology*, 54: 303–318.
- Foken, T., Wimmer, F., Mauder, M., Thomas, C., and Liebethal, C. (2006). Some aspects of the energy balance closure problem. *Atmospheric Chemistry and Physics*, 6: 4395–4402.
- Fortier, J., Gagnon, D., Truax, B., Lambert, F. (2010). Biomass and volume yield after 6 years in multiclonal hybrid poplar riparian buffer strips. *Biomass and Bioenergy*, 34: 1028-1040.
- Garratt, J.R. (1978). Transfer characteristics for a heterogeneous surface of large aerodynamic roughness. *Quarterly Journal of the Royal Meteorological Society*, 104: 491–502.
- Food and Agriculture Organization of the United Nations (FAO) (2010). Global forest resources assessment 2010: 1–378.
- Hall, R. J., Joss, B. N., Sidders, D. M., and Keddy, T. J. (2004). The FAACS backcast: Afforestation activity in the Prairie Provinces (1990–2002). *The Forestry Chronicle*, 80: 727–735.
- Hansen, E. A. (1993). Soil carbon sequestration beneath hybrid poplar plantations in the North Central United States. *Biomass & Bioenergy*, 5: 431-436.
- Hansen, E. A., McLaughlin, R. A., and Pope, P. E. (1988). Biomass and nitrogen dynamics of hybrid poplar on two different soils: implications for fertilization strategy. *Canadian Journal of Forest Research*, 18: 223–230.

- Harris, P. P., Huntingford, C., Cox, P. M., Gash, J. H. C., and Malhi, Y. (2004). Effect of soil moisture on canopy conductance of Amazonian rainforest. *Agricultural and Forest Meteorology*, 122: 215–227.
- Heilman, P. E., and Fu-Guang, X. (1993). Influence of nitrogen on growth and productivity of short-rotation *Populus trichocarpa* x *Populus deltoides* hybrids. *Canadian Journal of Forest Research*, 23: 1863–1869.
- Hogg, E. H. (Ted), Brandt, J. P., and Michaelian, M. (2008). Impacts of a regional drought on the productivity, dieback, and biomass of western Canadian aspen forests. *Canadian Journal of Forest Research*, 38: 1373–1384.
- Hogg, E. H. (Ted), Brandt, J. P., & Kochtubajda, B. (2005). Factors affecting interannual variation in growth of western Canadian aspen forests during 1951–2000. *Canadian Journal of Forest Research*, 35: 610–622.
- Humphreys, E. R., Black, T. A., Ethier, G. J., Drewitt, G. B., Spittlehouse, D. L., Jork, E.M., Nesic, Z., and Livingston, N. J. (2003). Annual and seasonal variability of sensible and latent heat fluxes above a coastal Douglas-fir forest, British Columbia, Canada. *Agricultural and Forest Meteorology*, 115: 109–125.
- Jassal, R. S., Black, T. A., Arevalo, C., Jones, H., Bhatti, J. S., and Sidders, D. (2013). Carbon sequestration and water use of a young hybrid poplar plantation in north-central Alberta. *Biomass and Bioenergy*, 56: 323–333.
- Jassal, R.S., Black, T.A., Jones, H. (2014). Scope of plantation forestry in the aspen parkland of Alberta - A White Paper. Alberta Innovates-Biosolutions, Biological GHG Management Program. January 2014.
- Joss, B. N., Hall, R. J., Sidders, D. M., and Keddy, T. J. (2008). Fuzzy-logic modeling of land suitability for hybrid poplar across the Prairie Provinces of Canada. *Environment Monitoring and Assessment*, 141: 79–96.
- Kelliher, F. M., Leuning, R., Raupach, M. R., and Schulze, E. D. (1995). Maximum conductances for evaporation from global vegetation types. *Agricultural and Forest Meteorology*, 73: 1-16.
- Kidston, J., Brümmer, C., Black, T. A., Morgenstern, K., Nesic, Z., McCaughey, J. H., and Barr, A. G. (2010). Energy balance closure using eddy covariance above two different land surfaces and implications for CO<sub>2</sub> flux measurements. *Boundary-Layer Meteorology*, 136: 193–218.
- Kienzle, S. W., Nemeth, M. W., Byrne, J. M., and MacDonald, R. J. (2012). Simulating the hydrological impacts of climate change in the upper North Saskatchewan River basin, Alberta, Canada. *Journal of Hydrology*, 412-413: 76–89.

- Kim, H.-S., Oren, R., and Hinckley, T. M. (2008). Actual and potential transpiration and carbon assimilation in an irrigated poplar plantation. *Tree Physiology*, 28: 559–77.
- Krishnan, P., Black, T. A., Grant, N. J., Barr, A. G., Hogg, E. H. (Ted), Jassal, R. S., and Morgenstern, K. (2006). Impact of changing soil moisture distribution on net ecosystem productivity of a boreal aspen forest during and following drought. *Agricultural and Forest Meteorology*, 139: 208–223.
- Labrecque, M., and Teodorescu, T. I. (2003). High biomass yield achieved by *Salix* clones in SRIC following two 3-year coppice rotations on abandoned farmland in southern Quebec, Canada. *Biomass and Bioenergy*, 25: 135–146.
- Larocque, G. R., DesRochers, A., Larchevêque, M., Tremblay, F., Beaulieu, J., Mosseler, A., Major, J. E., Gaussiran, S., Thomas, B.R., Sidders, D., Périnet, P., Kort, J., Labrecque, M., Savoie, P., Masse, S., Bouman, O. T., Kamelchuck, D., Benomar, L., Mamashita, T., and Gagné, P. (2013). Research on hybrid poplars and willow species for fast-growing tree plantations: Its importance for growth and yield, silviculture, policy-making and commercial applications. *The Forestry Chronicle*, 89: 32–41.
- Lemus, R., and Lal, R. (2005). Bioenergy crops and carbon sequestration. *Critical Reviews in Plant Sciences*, 24: 1–21.
- Leuning, R. (1995). A critical appraisal of a combined stomatal-photosynthesis model for C3 plants. *Plant, Cell and Environment*, 18: 339–335.
- Leuning, R., Zhang, Y. Q., Rajaud, A., Cleugh, H., and Tu, K. (2008). A simple surface conductance model to estimate regional evaporation using MODIS leaf area index and the Penman-Monteith equation. *Water Resources Research*, 44: 1–17.
- MacDonald, R. J., Byrne, J. M., Boon, S., and Kienzle, S. W. (2012). Modelling the potential impacts of climate change on snowpack in the North Saskatchewan River Watershed, Alberta. *Water Resources Management*, 26: 3053–3076.
- McNaughton, K. G., Jarvis, P. G. (1984). Using the penman-monteith equation predictively. *Agricultural Water Management*, 8: 263-278.
- Meinzer, F. C., Hinckley, T. M., and Ceulemans, R. (1997). Apparent responses of stomata to transpiration and humidity in a hybrid poplar canopy. *Plant, Cell and Environment*, 20: 1301–1308.
- Meiresonne, L., Nadezhdin, N., Cermak, J. Van Slycken, J., Ceulemans, R. (1999). Measured sap flow and simulated transpiration from a poplar stand in Flanders (Belgium). *Agricultural and Forest Meteorology*, 96: 165-179.

- Michaelian, M., Hogg, E. H., Hall, R. J., and Arsenault, E. (2011). Massive mortality of aspen following severe drought along the southern edge of the Canadian boreal forest. *Global Change Biology*, 17: 2084–2094.
- Migliavacca, M., Meroni, M., Manca, G., Matteucci, G., Montagnani, L., Grassi, G., Zenone, T., Teobalbelli, M., Goded, I., Colombo, R., and Seufert, G. (2009). Seasonal and interannual patterns of carbon and water fluxes of a poplar plantation under peculiar eco-climatic conditions. *Agricultural and Forest Meteorology*, 149: 1460–1476.
- Monteith, J. L. (1965). Evaporation and Environment. *Symposia of the Society for Experimental Biology*, 19: 205-224.
- Monteith, J. L., Unsworth, M. H. (2008). *Principles of environmental physics*, 3<sup>rd</sup> edition. Elsevier, London.
- Nave, L. E., Swanston, C. W., Mishra, U., and Nadelhoffer, K. J. (2013). Afforestation effects on soil carbon storage in the United States: A synthesis. *Soil Science Society of America Journal*, 77: 1–15.
- Novick, K., Brantley, S., Miniati, C. F., Walker, J., and Vose, J. M. (2014). Inferring the contribution of advection to total ecosystem scalar fluxes over a tall forest in complex terrain. *Agricultural and Forest Meteorology*, 185: 1–13.
- Perry, C. H., Miller, R. C., and Brooks, K. N. (2001). Impacts of short-rotation hybrid poplar plantations on regional water yield. *Forest Ecology and Management*, 143: 143–151.
- Priestley, C. H. B., and Taylor, R. J. (1972). On the assessment of surface heat flux and evaporation using large-scale parameters. *Monthly Weather Review*, 100: 81–92.
- Rijtema, P.E., and De Vries, W. (1994). Differences in precipitation excess and nitrogen leaching from agricultural lands and forest plantations. *Biomass and Bioenergy*, 6: 103-113.
- Robinson, B. H., Green, S. R., Chancerel, B., Mills, T. M., and Clothier, B. E. (2007). Poplar for the phytomanagement of boron contaminated sites. *Environmental Pollution (Barking, Essex : 1987)*, 150: 225–233.
- Saugier, B., and Katerji, N. (1991). Some plant factors controlling evapotranspiration. *Agricultural and Forest Meteorology*, 54: 263–277.
- Schindler, D. W. (2001). The cumulative effects of climate warming and other human stresses on Canadian freshwaters in the new millennium. *Canadian Journal of Fisheries and Aquatic Sciences*, 58: 18–29.
- Schindler, D. W., and Donahue, W. F. (2006). An impending water crisis in Canada's western prairie provinces. *Proceedings of the National Academy of Sciences of the United States of America*, 103: 7210–7216.

- Schneider, R. (2006). Death by a thousand cuts: impacts of in situ oil sands development on Alberta's boreal forest. Edmonton (AB), Drayton Valley (AB): *Canadian Parks and Wilderness Society and the Pembina Institute*: p. 36.
- Sierra, M., Martínez, F. J., Verde, R., Martín, F. J., and Macías, F. (2013). Soil-carbon sequestration and soil-carbon fractions, comparison between poplar plantations and corn crops in south-eastern Spain. *Soil and Tillage Research*, 130: 1–6.
- Stewart, J. (1988). Modelling surface conductance of pine forest. *Agricultural and Forest Meteorology*, 43: 19–35.
- Stewart, J., and Gay, L. W. (1989). Preliminary modelling of transpiration from the fife site in Kansas. *Agricultural and Forest Meteorology*, 48: 305–315.
- Sun, G., Zhou, G., Zhang, Z., Wei, X., McNulty, S. G., and Vose, J. M. (2006). Potential water yield reduction due to forestation across China. *Journal of Hydrology*, 328: 548–558.
- Tanner, C. B., and Jury, W. A. (1976). Estimating Evaporation and Transpiration from a Row Crop during Incomplete Cover. *Agronomy Journal*, 68: 240–243.
- Traux, B., Gagnon, D., Fortier, J., and Lambert, F. (2012). Yield in 8 year-old hybrid poplar plantations on abandoned farmland along climatic and soil fertility gradients. *Forest Ecology and Management*, 267: 228–239.
- Verlinden, M. S., Broeckx, L. S., Zona, D., Berhongaray, G., De Groote, T., Camino Serrano, M., Janssens, I. A., Ceulemans, R. (2013). Net ecosystem production and carbon balance of an SRC poplar plantation during its first rotation. *Biomass and Bioenergy*, 56: 412–422.
- Vesterdal, L., Ritter, E., and Gundersen, P. (2002). Change in soil organic carbon following afforestation of former arable land. *Forest Ecology and Management*, 169: 137–147.
- Wang, Y-P., Leuning, R., Isaac, P., and Zhou, G. 2004. Scaling the estimate of maximum canopy conductance from patch to region and comparison of aircraft measurements. *In: Forests at the Land-Atmosphere Interface*. Eds. Mencuccini, M., Grace, J., Moncrieff, J. & McNaughton, K.G. CABI Publishing
- Webb, E. K., Pearman, G. L., Leuning, R. (1980). Correction of flux measurements for density effects due to heat and water vapour transfer. *Quarterly Journal of the Royal Meteorological Society*, 196: 85-100.
- Wilske, B., Lu, N., Wei, L., Chen, S., Zha, T., Liu, C., Xu, W., Noormets, A., Huang, J., Wei, Y., Chen, J., Zhang, Z., Ni, J., Sun, G., Guo, K., McNulty, S., John, R., Han, X., Lin, G., and Chen, J. (2009). Poplar plantation has the potential to alter the water balance in semiarid Inner Mongolia. *Journal of Environmental Management*, 90: 2762–2770.

- Wilson, K. B., and Baldocchi, D. D. (2000). Seasonal and interannual variability of energy fluxes over a broadleaved temperate deciduous forest in North America. *Agricultural and Forest Meteorology*, 100: 1–18.
- Wilson, K., Goldstein, A., Falge, E., Aubinet, M., Baldocchi, D., Berbigier, P., Bernhofer, C., Ceulemans, R., Dolman, H., Field, C., Grelle, A., Ibrom, A., Law, B. E., Kowalski, A., Meyers, T., Moncrieff, J., Monson, R., Oechel, W., Tenhunen, J., Valentini, R., and Verma, S. (2002). Energy balance closure at FLUXNET sites. *Agricultural and Forest Meteorology*, 113: 223–243.
- Wu, A., Black, T. A., Verseghy, D. L., Blanken, P. D., Novak, M. D., Chen, W., and Yang, P. C. (2000). A comparison of parametrizations of canopy conductance of aspen and Douglas-fir forests for class. *Atmosphere-Ocean*, 38: 81–112.
- Zhang, Y. Q., Chiew, F. H. S., Zhang, L., Leuning, R., and Cleugh, H. a. (2008). Estimating catchment evaporation and runoff using MODIS leaf area index and the Penman-Monteith equation. *Water Resources Research*, 44: 1–15.
- Zhou, J., Zhang, Z., Sun, G., Fang, X., Zha, T., McNulty, S., Chen, J., Jin, Y., Noormets, A. (2013). Forest ecology and management response of ecosystem carbon fluxes to drought events in a poplar plantation in Northern China. *Forest Ecology and Management*, 300: 33–42.
- Zona, D., Janssens, I. A., Aubinet, M., Gioli, B., Vicca, S., Fichot, R., and Ceulemans, R. (2013). Fluxes of the greenhouse gases (CO<sub>2</sub>, CH<sub>4</sub> and N<sub>2</sub>O) above a short-rotation poplar plantation after conversion from agricultural land. *Agricultural and Forest Meteorology*, 169: 100–110.

## Appendices

### Appendix A : Wind rose, flux footprint analysis and site stability parameters

#### A.1 Wind rose at HP09 and HP11 each year of measurement

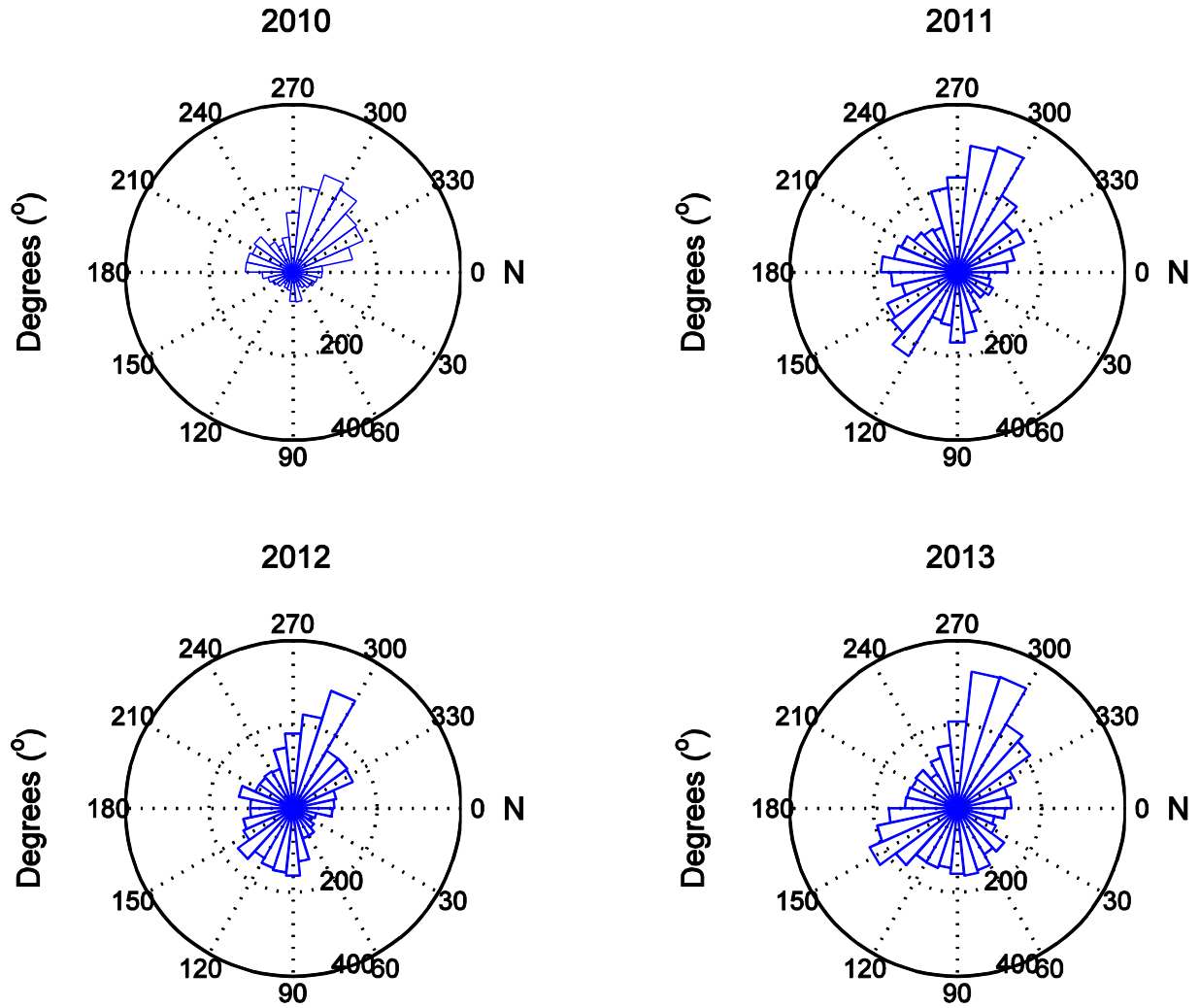


Figure 25: 11° bins of half hourly (May 1- September 30) wind direction for each year at HP09.

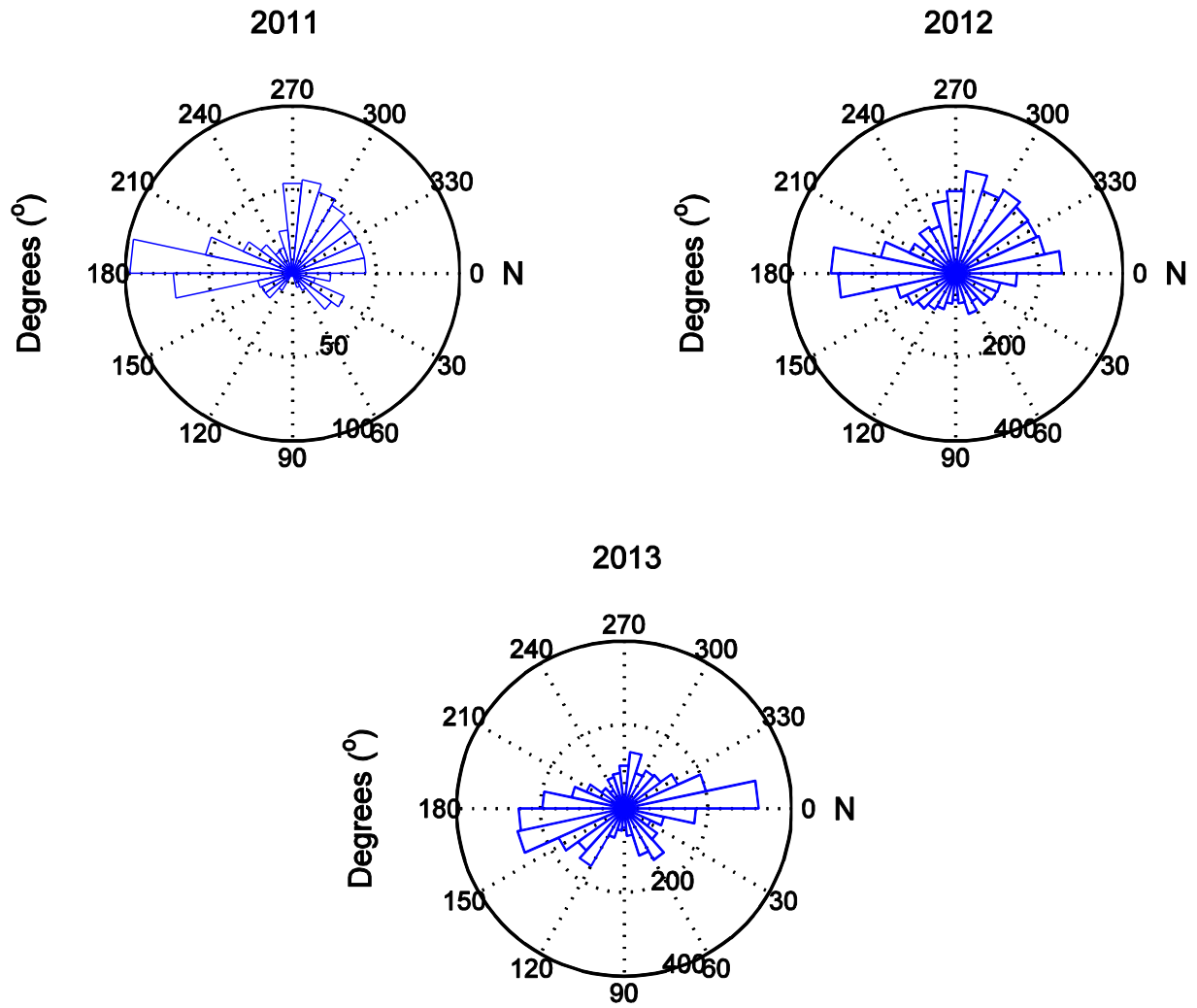


Figure 26: 11° bins of half hourly (May 1- September 30) wind direction for each year at HP11.

A.2 Flux footprint analysis at HP09 and HP11 each year of measurement

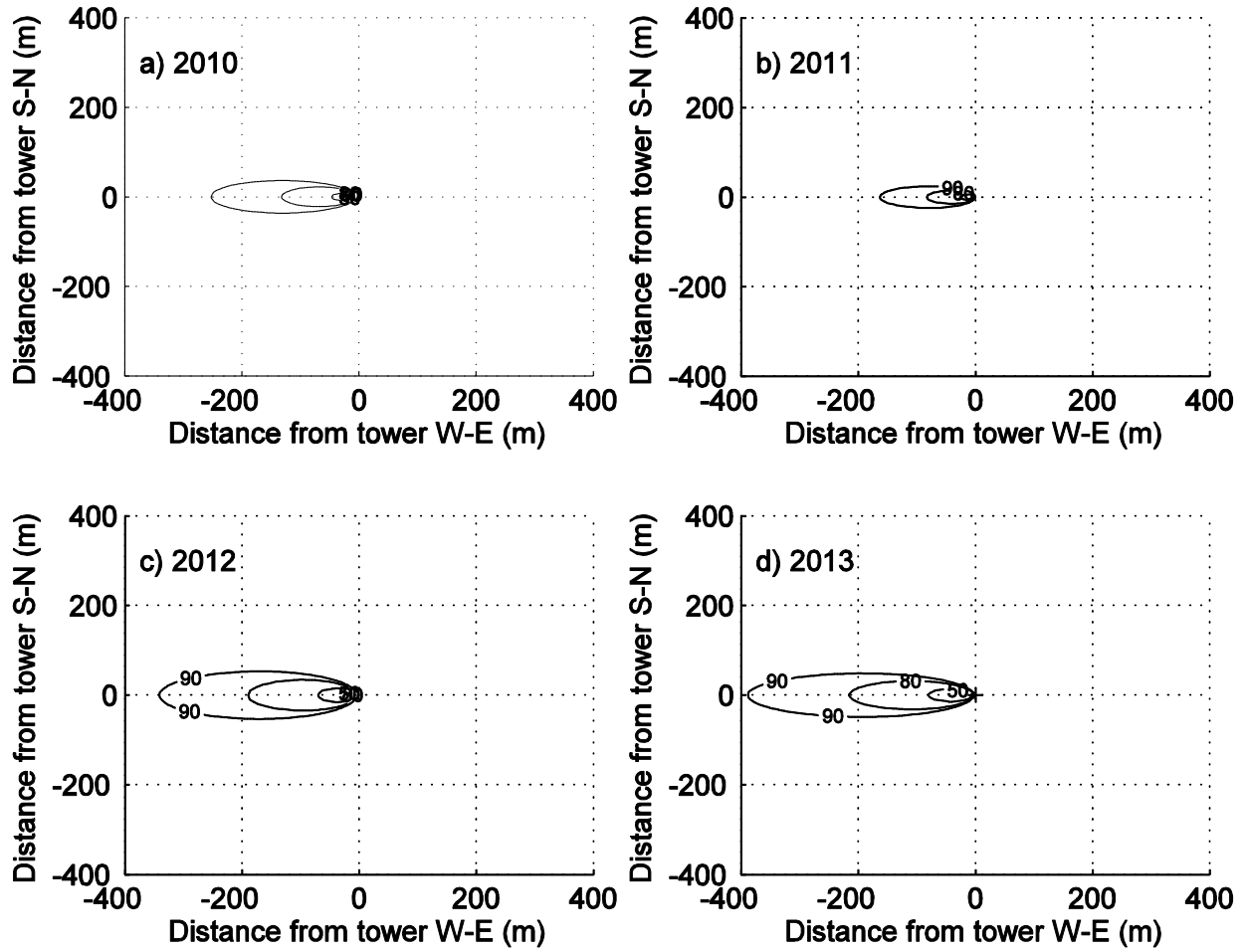


Figure 27: Daytime flux footprint analysis showing the 50, 80 and 90% cumulative turbulent source area for each year at HP09.

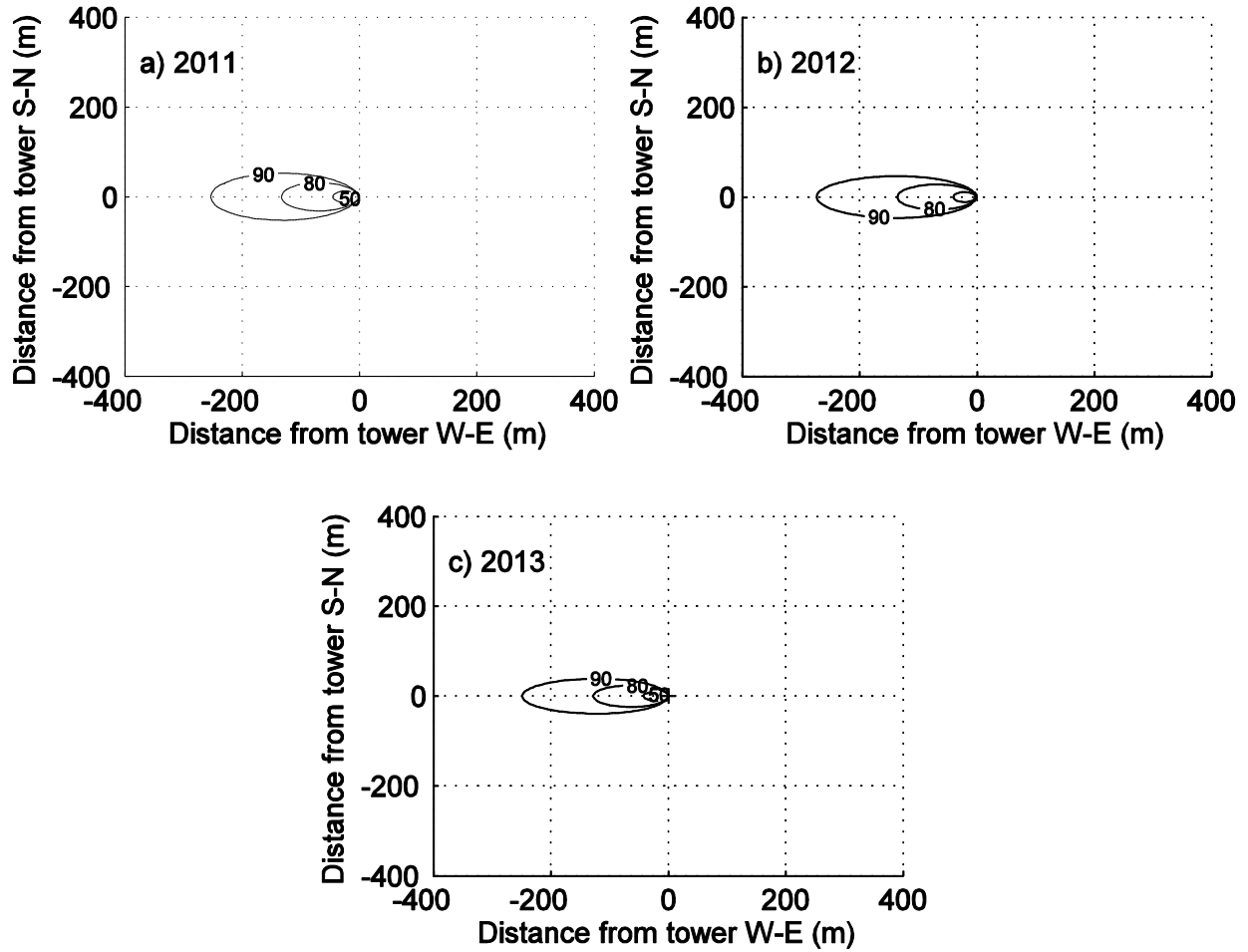


Figure 28: Daytime flux footprint analysis showing the 50, 80 and 90% cumulative turbulent source area for each year at HP11.

### A.3 Site instrumentation and canopy heights used to calculate stability parameters and flux footprint analysis

Table 3: EC instrumentation ( $z$ ), canopy ( $h$ ), zero plane displacement ( $d$ ), and  $z - d$  along with roughness length ( $z_m$ ) at HP09 and HP11, each year of the study.

Site	Year	$z$ (m)	$h$ (m)	$d$ (m)	$z - d$ (m)	$z_m$ (m)
HP09	2010	2	0.5	0.33	1.67	0.05
	2011	2	1.5	0.98	1.02	0.15
	2012	4.5	2.5	1.63	2.87	0.25
	2013	5.5	4	2.6	2.9	0.4
HP11	2011	2	0.5	0.33	1.67	0.05
	2012	2	1.5	0.98	1.02	0.15
	2013	3	2.5	1.63	1.37	0.25

## Appendix B : Site pictures

### B.1 Instrumentation at HP09 and HP11

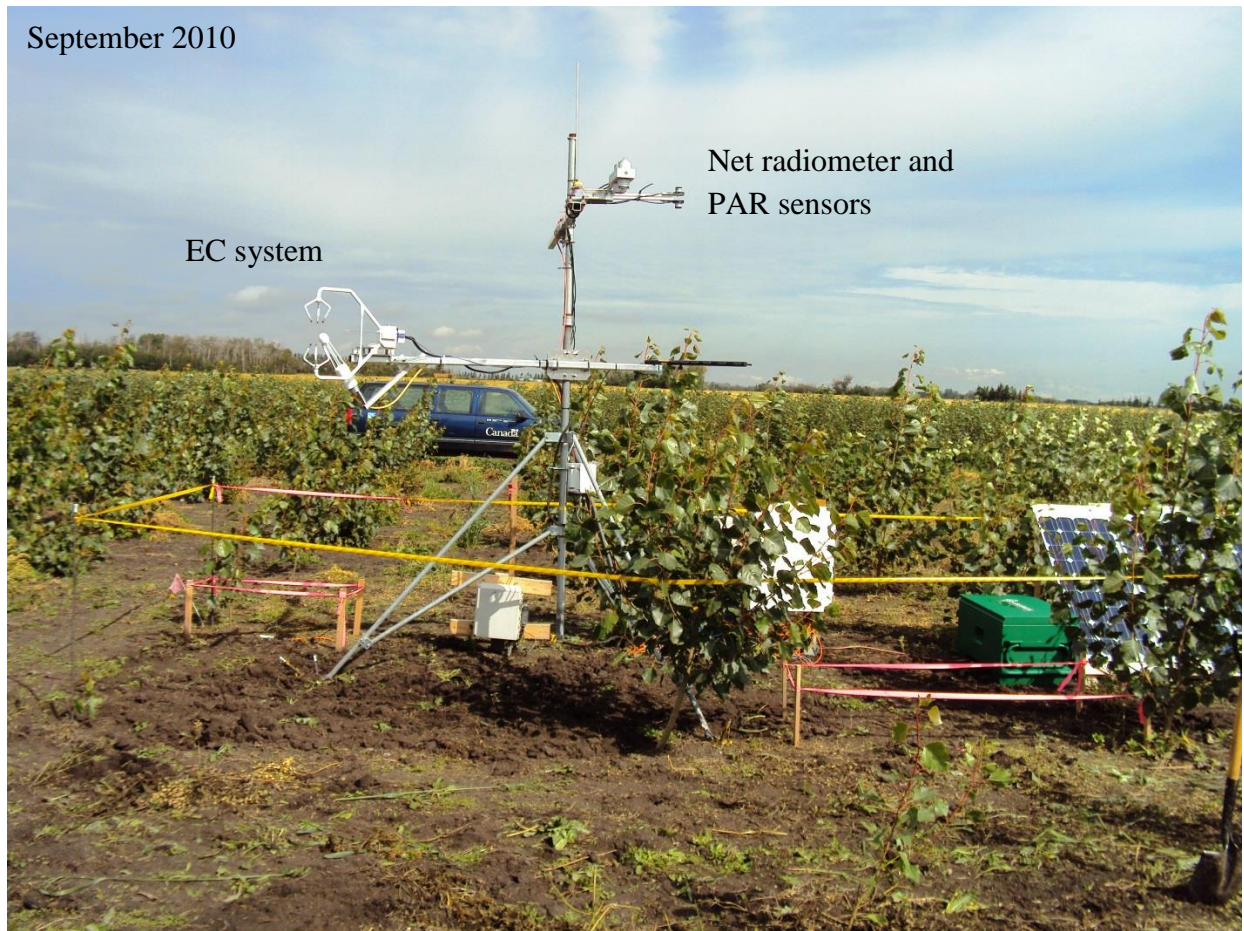


Figure 29: Tripod on which EC and radiation sensors were initially mount at HP09.

September 2011

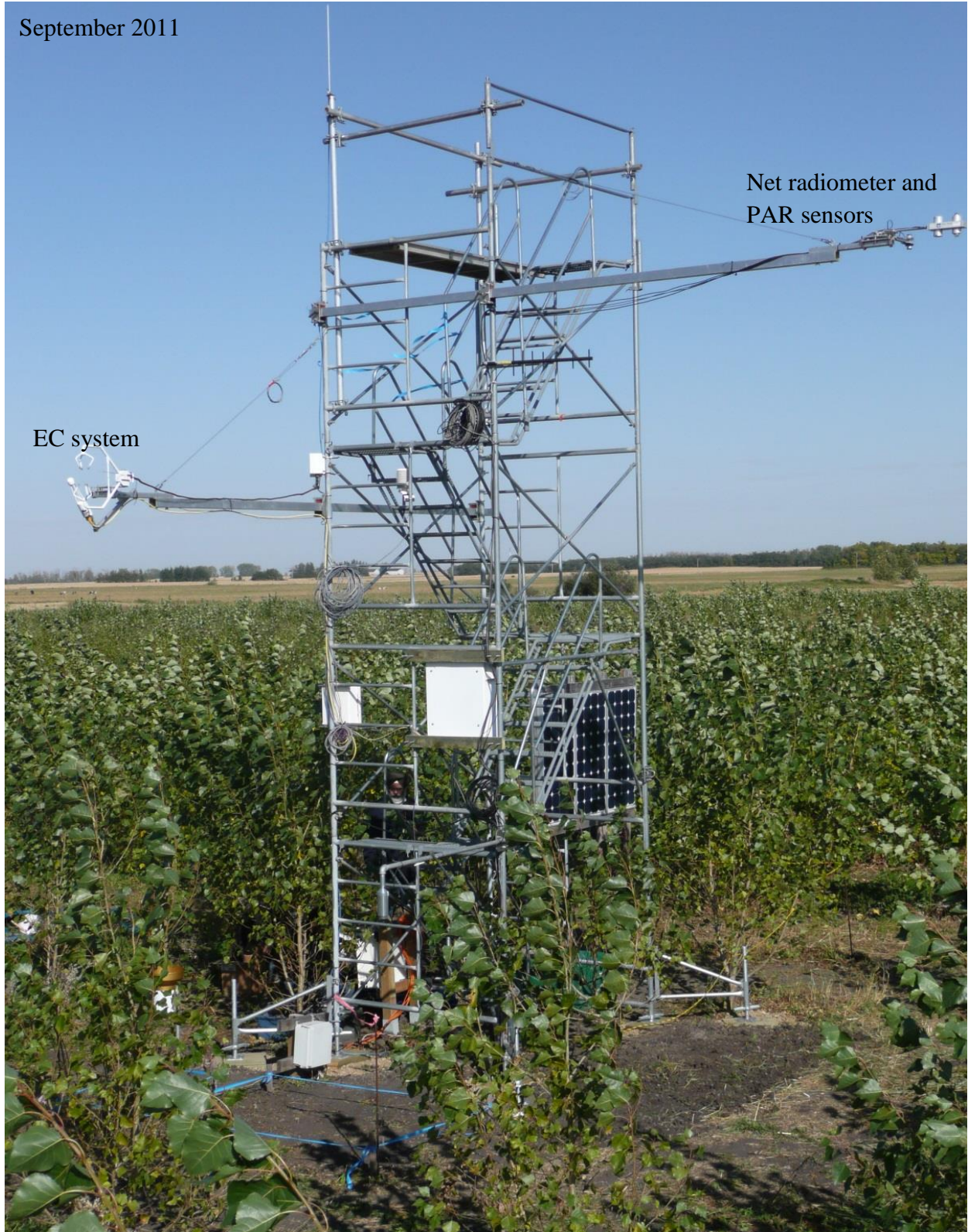


Figure 30: Scaffold tower used to increase EC and radiation sensor height in response to HP growth at HP09.

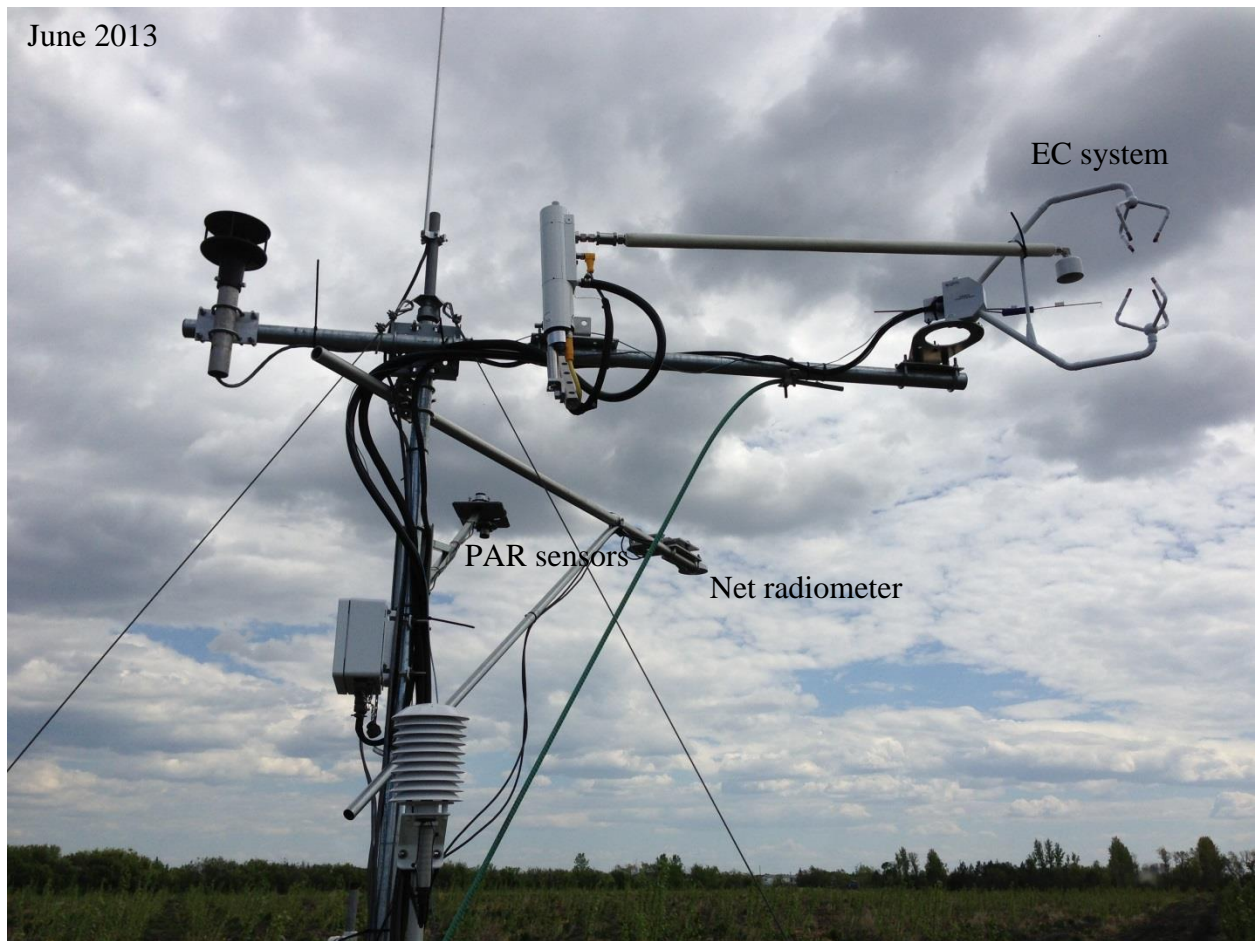


Figure 31: Tripod with guy-wires on which EC and radiation sensors initially mounted at HP11.

**B.2 Soil and vegetation during HP growth at HP09 and HP11**



Figure 32: Soil horizon profile (0 - 80 cm) at HP09.



Figure 33: Progression of HP growth throughout the measurement period. Panel a) and b) show HP09 early and late in the 2<sup>nd</sup> year of growth, respectively. Panels c) and d) show HP09 during the 4<sup>th</sup> and 5<sup>th</sup> year of growth.



Figure 34: Soil horizon profile (0 - 80 cm) at HP11.



Figure 35: Progression of HP growth throughout the measurement period at HP11. Panels a), b) and c) show HP11 during the 1<sup>st</sup>, 2<sup>nd</sup> and 3<sup>rd</sup> growing seasons.